MARIANA MIRACCA LAGE

The role played by density in meso and large scale ocean dynamics

São Paulo

2020

MARIANA MIRACCA LAGE

The role played by density in meso and large scale ocean dynamics

A thesis submitted to the Instituto Oceanográfico of the Universidade de São Paulo in partial fulfillment for the degree of Master of Science, Oceanography, with emphasis in Physical Oceanography

Advisor: Paulo Simionatto Polito

São Paulo

2020

LAGE, Mariana Miracca. **The role played by density in meso and large scale ocean dynamics**. Thesis (Master's) presented to the Instituto Oceanográfico of the Universidade de São Paulo to obtain the title of Master of Sciences, Oceanography Program, Physical Oceanography area.

Evaluated in 25/09/2020

Corrected version

Examination Committee

Prof. Dr. Paulo Simionatto Polito — Institution: Universidade de São Paulo (USP)

Grade: Approved — Signature_____

Profa. Dra. Cristina González Haro — Institution: Institut de Ciències del Mar (ICM)

Grade: Approved — Signature_____

Prof. Dr. César Barbedo Rocha — Institution: University of Connecticut (UConn)

Grade: Approved — Signature_____

São Paulo

2020

À minha família,
sem a qual eu nada seria.

Acknowledgements

I would like to dedicate this work to my parents, Adriana and Claudio, and my sister Marcela, who always supported me and encouraged me to follow my dreams. Thank you for being an inspiration, for all the values you taught me over these 28 years and for always believe I can accomplish everything, even though I doubt it sometimes. Thanks for pushing me (hard haha) towards growth. For all the unconditional love, support, friendship, hugs, I can't (and never will) thank you enough.

For my advisor, Paulo, I must say "OMG we did it!!". Thanks for the talks about science, about nothing, about life, about politics. Thank you for being part of the most amazing part of my life and for having me under your supervision in LOS for 5 years. I'm very proud of being part of this family. And most of all, thanks for believing in my ideas and for being an amazing advisor, raising me as a scientist. And the *dynamic duo* (jokes aside haha) wouldn't be complete without you, Olga. Thank you for being such an inspiration. When I think about women in science, the first person I think about is you. I told you once, and always will, maybe in 20 years I'll be as good as you are, and I'll certainly pursue that path. You both will always be in my heart (and I hope I get some visits wherever I will be in the future). I also promise to send my mom in the Halloween parties.

Thank you Cris and Jordi, for being so welcoming I felt at home in Barcelona. Thanks for receiving me at ICM, and for helping me develop this wonderful work. I definitely could not have done it without you. Hopefully we will collaborate a lot in a near future!

I would also like to acknowledge the Conselho Nacional de Desenvolvimento Científico e Tecnológico - Brasil (CNPq) and the Fundação de Amparo à Pesquisa do Estado de São Paulo – FAPESP (2019/02968-9 and 2019/13830-8) for the financial support to conduct this study.

To all my LOS friends, especially Piero that insists in having lunch alone. Thank you for the long lasting conversations and for being such a good partner in having coffee. And thanks for all the "good mornings" over the past 5 years. (You'll miss me, I can bet that). Marouan, thank you for the advices, conversations, and for an awesome Califa experience

during the Ocean Sciences! I really appreciate our conversations, you're like a big brother to me.

For the LaDinos, Dendê and Iguim, I must say I had the most amazing lunches in ages. Thank you for your friendship and I hope I can see you all, nailing life as you always encouraged me to do. Thanks Iury and Agatinha for the most amazing first Ocean Sciences Meeting, and for all the conversations and inspiring thoughts. Filipe, for being such a good friend during classes and outside the University, thanks for the laughs and the time we spent resolving assignments eating pizza. Thank you all so much (and I mean it!) for hearing me the every single time I said "baroclinic modes". Thanks for the happy hours as well, they were vital for my brain to cool down. And last but not least, Ilson. Thank you for the advices, the ideas, and to consider me $\frac{1}{4}$ LaDina. I won't forget that.

Dante, thank you for that one special hug and for all we are sharing since then.

Há um menino, há um moleque, morando sempre no meu coração.
Toda vez que o adulto fraqueja ele vem pra me dar a mão.
Milton Nascimento

Perhaps I occasionally sought to give, or inadvertently gave,
to the student a sense of battle on the intellectual battlefield.
If all you do is to give them a faultless and complete and
uninhabited architectural masterpiece, then you do not
help them to become builders of their own.
Carl Gustaf Rossby

Abstract

Sea surface height is key in ocean dynamics. Nowadays, level 4 satellite products based on multiple nadir looking altimeters can resolve horizontal scales of around 100 km, which is enough to study meso to large scale dynamics [$O(10^2 - 10^3)$ km] but miss smaller scale features [$O(10 - 10^2)$ km]. Using outputs from a general ocean circulation model, we reconstructed the streamfunction using sea surface buoyancy under the surface quasi-geostrophy (SQG) theory to determine which dynamical regime — classical quasi-geostrophy (QG) or SQG — dominates the sea surface height signal in the mesoscale range at 11°S, 24.5°S and 34.5°S on the South Atlantic. At these latitudes, analyses of sub-areas show that this dominance is related to the seasonal cycle of the mixed layer and the amount of eddy kinetic energy in the mesoscale. The sea surface height reconstruction under the SQG theory is better in winter, and SQG dominates in high eddy kinetic energy regions. Subsequently, we focused in Rossby wave dynamics. We identified long, first mode baroclinic Rossby waves in sea surface anomaly altimeter data using a 2D Finite Impulsive Response filter in the three ocean basins of the Southern Hemisphere. Then, we reconstructed the sea surface height anomaly applying a traditional QG vertical mode decomposition in the numerical model outputs and evaluated the contribution of stratification to the modulation of the Rossby waves' amplitudes: the more stratified the water column, the larger the amplitudes of the Rossby waves. The results shed a light on the interplay between surface and interior dynamics, connecting the ocean surface expression to the interior stratification. With the upcoming higher resolution altimeters, the analyzes can be extended towards finer scales, which will lead to a better characterization of processes that may influence the variation of potential vorticity, other than stratification, and thus modifying the sea surface height field and consequently Rossby waves' characteristics.

Keywords: Surface quasi-geostrophy, Quasi-geostrophy, buoyancy, vertical modes, first baroclinic mode, Rossby waves

Resumo

A altura da superfície do mar é uma variável-chave para entender a dinâmica do oceano. Atualmente, produtos de satélite de nível 4 baseados em vários altímetros podem resolver escalas horizontais em torno de 100 km, o que é suficiente para estudar a dinâmica de meso a grande escala [O (10^2 - 10^3) km] mas apresenta um problema para identificar feições de escalas menores [O (10 - 10^2) km]. Usando saídas de um modelo de circulação oceânica global, reconstruímos a função de corrente usando o empuxo da superfície do mar sob a teoria da quase-geostrofia de superfície (SQG) para determinar qual regime dinâmico — quase-geostrofia clássica (QG) ou SQG — domina o sinal de altura da superfície do mar na mesoescala em 11°S, 24.5°S e 34.5°S no Atlântico Sul. Nessas latitudes, análises de sub-áreas mostram que essa dominância está relacionada ao ciclo sazonal da camada de mistura e a quantidade de energia cinética das perturbações na mesoescala. A reconstrução da altura da superfície do mar sob a teoria SQG é melhor no inverno, e o regime SQG domina em regiões onde a energia cinética das perturbações é mais alta. Posteriormente, focamos na dinâmica de ondas de Rossby. Identificamos ondas de Rossby longas do primeiro modo baroclínico nos dados de anomalia da altura da superfície do mar do altímetro usando um filtro 2D de resposta impulsiva finita nas três bacias oceânicas do Hemisfério Sul. Em seguida, reconstruímos a anomalia da altura da superfície do mar aplicando a decomposição em modos verticais QG nas saídas do modelo numérico e avaliamos a contribuição da estratificação para a modulação das amplitudes das ondas de Rossby: quanto mais estratificada a coluna de água, maiores as amplitudes das ondas. Os resultados apontam para a interação entre a dinâmica da superfície e a dinâmica do interior do oceano, conectando a expressão da altura da superfície à estratificação da coluna d'água. Com o lançamento dos próximos altímetros de alta resolução, as análises podem ser estendidas para escalas menores, o que levará a uma melhor caracterização dos processos que influenciam a variação da vorticidade potencial, além da estratificação, modificando a altura da superfície do mar e, consequentemente, as características das ondas de Rossby.

Palavras-chave: Quase geostrofia de superfície, Quase-geostrofia, empuxo, modos verticais, primeiro modo baroclínico, ondas de Rossby

Contents

List of Figures

List of Tables

1 Introduction

1.1 The ocean viewed from space

Remote sensing can be defined as the acquisition of information about an element or phenomenon from a distance, meaning no physical contact between the source and the object to be measured. From 1978 on, several satellites designed to provide measurements from the ocean were launched (ROBINSON, 2004), and this had a huge impact in the scientific community in terms of understanding sea surface features. Thus, as long as it could be communicated through electromagnetic radiation, large scale phenomena that were poorly studied could from then on be properly brought into light.

To be meaningful, the data acquired from space must be calibrated and validated. Calibration is a process wherein the electromagnetic energy captured by the sensor is transformed into the variable that it was supposed to measure, based on empirical and theoretical methods (ROBINSON, 2010). In order to do so, when it is possible, algorithms are developed by adjusting the sensor readings to *in situ* data (ROBINSON, 2010), both collected at approximately the same time and location. It is also done in different areas and time periods, to avoid biases. In addition, product validation is made by comparing the calibrated satellite data with the same data measured directly, at the same location and time, provided the *in situ* dataset is not the same of the calibration. This process is made for several times and different environmental conditions. In that way, *in situ* data (e.g. buoys, ships) are not only complementary, but essential to ensure the reliability of satellite data.

Satellite data is restricted to the ocean surface. Although it has the great advantage of global coverage, the radiation cannot penetrate in the water column. The information retrieved by the sensor is representative of the surface and a priori nothing can be said regarding interior dynamics. Therefore, connecting the information at and below the surface remains a challenge. Altimeters are nadir-viewing radar sensors that emit pulses

and records the travel time, the magnitude and the shape of each returned signal after they are reflected from the surface (ROBINSON, 2010). Its measurements had a great impact in the acquisition of sea surface height values, and many features and physical processes that have a signature at the surface could be better understood. This is because the sea surface height changes either by a net flux of mass or variations in the density field in the water column, caused by, for example, baroclinic waves (POLITO; CORNILLON, 1997).

Unlike other satellites, altimeters can actually obtain information up to the thermocline depth by making simple assumptions. This happens because what causes the sea surface to slope is intrinsically related to ocean dynamics, both at the surface and at different depths. On one hand, assuming an homogeneous two-layered ocean in a steady state and flat bottom, there is no horizontal density gradient because densities do not vary. If the pycnocline slopes, the resulting balance is purely geostrophic. Selecting two different pycnocline locations, one deeper than the other, hydrostatic balance ensures that their mean density values differ. Therefore, surface height will differ by a factor that it is proportional to the density relative difference. Then, velocity profiles can be written as a Heaviside function and shear reduces to a pycnocline singularity. On the other hand, in a continuously stratified framework, the ocean is layered and horizontal density gradients arise. From the hydrostatic balance, the geostrophic vertical velocity shears, and this shear is given by horizontal variations in density. This represents the thermal wind balance (PEDLOSKY, 1987; ROBINSON, 2004; CUSHMAN-ROISIN; BECKERS, 2012).

Since altimeters do not provide geostrophic velocity measurements at depth, describing flows based only on surface variations becomes problematic. However, if the density 3D field is known, the thermal wind equations can be integrated and vertical velocity profiles can be estimated. In addition, ocean circulation is mostly driven by the wind, so we can presuppose that there is no significant movement in greater depths. This implies that the ocean can be divided in two layers, separated by the thermocline characterized by the presence of strong density gradients, and the movement is concentrated in the surface layer. Therefore, there is no horizontal pressure gradient at the deeper layer. Considering again an hydrostatic ocean, if the surface slopes towards one direction, the deep layer must slope in the opposite direction, which means that if the signal at the surface is a crest, the signal at the interface is a trough. To maintain the balance, since density variations between layers are around 10^3 smaller than the density of the surface layer itself, the slope of the interface must be much greater than the slope at the surface (ROBINSON, 2004).

Furthermore, if one knows the density profile, more specifically the difference be-

tween layers, the interface slope can be estimated from altimetry, since the sensor measures the surface slope. Having this simplified structure of densities, say, in an ocean basin, the horizontal interface field would resemble the surface height field, although with larger amplitudes. All these simplifications demonstrate the potential of satellite altimetry when extending surface information to a certain depth, even though the ocean is not as simple as considered here. But what if we put aside the simplifications and try to handle a more realistic ocean? How to relate density, or any other *in situ* variable, with the variables measured by the satellite? And beyond that, what are exactly the features that the altimeter is seeing? Even after several years from the launch of Seasat, the first synthetic aperture radar projected to measure the ocean, these questions are still in debate.

One of the several features that can be detected in altimeter datasets is Rossby waves. They are the main oceanic response to large scale (10^2 – 10^3 km) long period (10^2 – 10^3 days) atmosphere forcing, being crucial to both atmospheric and ocean dynamics. They can also transfer information and energy across basins (GILL, 1982) and enhance western boundary currents (PEDLOSKY, 1965). Using GEOSAT data, barotropic Rossby waves were first identified by Gaspar and Wunsch (1989) at the northwest Atlantic. The authors combined the data from the altimeter with a linear barotropic Rossby wave model to assess if there was any fraction of ocean variability consistent with barotropic planetary waves. Their results suggested that a fraction ranging from 6–15% can be attributed to this wave. Three years later, Jacobs *et al.* (1992) found a large scale contamination of GEOSAT data due to aliased energy that can easily be mistaken by a baroclinic Rossby wave because the tidal error has both wavelength and direction corresponding to a first mode wave. Nevertheless, knowing the phenomenon that caused the aliased energy made it possible to refine GEOSAT data, and thus large scale baroclinic features could be identified. Indeed, Jacobs *et al.* (1993) detected baroclinic Rossby waves in the Pacific ocean after several data corrections, the tidal aliasing included, and found that the energy contained in GEOSAT data is coherent to propagating quasi-geostrophic Rossby waves, agreeing with its theoretical framework.

Unlike its barotropic counterpart, baroclinic planetary waves have a more direct impact in ocean circulation, since they affect the thermocline. In general, these waves owe their existence to the meridional gradient of potential vorticity. Thus, its generation is closely related to perturbations in the potential vorticity field, such as seasonal and stochastic variability of the wind stress curl, coupling between barotropic and baroclinic modes, baroclinic instability, potential vorticity advection (POLITO; CORNIL-

LON, 1997), reversals in ocean currents and buoyancy forcing (CIPOLLINI *et al.*, 2000), and variations in the latter allows several vertical modes of horizontal ocean currents (ROBINSON, 2004). To the present day, several studies on Rossby waves and ocean circulation were conducted with the accurate contribution of satellite datasets, specially altimeters, providing a global picture of these features (CHELTON; SCHLAX, 1996; STAMMER, 1997; CIPOLLINI *et al.*, 1998; POLITO; LIU, 2003) and a better understanding on how the ocean responds to atmospheric forcing (POLITO; CORNILLON, 1997; VIVIER *et al.*, 1999) and changes in climate (LI *et al.*, 2016). Besides that, these waves are also identifiable in chlorophyll signals (CIPOLLINI *et al.*, 2001; AMOL, 2018) and sea surface temperature (HILL *et al.*, 2000) from satellites.

However, many challenges still remain, especially when it comes to the ocean circulation below the surface. In this sense, numerical models are important tools to simulate and predict the oceanic response under a global changing scenario. At present, there is a range of general ocean circulation models, with different degrees of complexity; one example is a primitive equation model forced by realistic winds, which include a significant part of the large-scale, low frequency atmospheric variability at sea level. To accurately represent ocean circulation, this model need, for example, to correctly reproduce Rossby waves, since they carry information, i.e. energy, across basins (CIPOLLINI *et al.*, 2000); the better these waves are represented, the better the model in the representation of the physics of large-scale ocean circulation. If the model fails to resolve Rossby waves, one possible reason is that the density structure of the water column (stratification) may not be well represented and therefore the vertical structure of baroclinic modes is compromised. To assess that, we can compare the modeled waves with the ones derived from altimeter data (POLITO *et al.*, 2008; WATANABE *et al.*, 2016).

In this context, we propose to study the relationship between the density and the sea surface height fields regarding meso and large scale variability, to understand how the latter responds to the dynamics and reflect the motions at depth. This thesis has three main Chapters with results from quasi-geostrophic (QG) and surface quasi-geostrophic (SQG) theory in the study of the sea surface height field. Chapter 1 provides the motivation and the theoretical framework in which this thesis builds upon. In Chapter 2, we discuss mainly what theory — QG or SQG — best characterizes sea surface height variations relating model outputs and altimeter data. In other words, which theory has a more relevant dynamical framework to interpret the surface signal at the mesoscale, and in which extent we can apply these results to observations. In Chapter 3 we apply the QG theory in the

study of planetary waves at mid-latitudes and discuss how the amplitude of these waves are related to changes in stratification.

1.2 Large scale ocean dynamics and planetary waves

Earth's rotation and sphericity become extremely important in large-scale ocean movements, and the variation of the Coriolis parameter (f) with latitude results in the β effect. Moreover, these movements are mainly horizontal, so the only Coriolis acceleration component that matters is the one involving horizontal velocities, and consequently only the local vertical component of f is dynamically significant. Rossby waves, also called planetary waves, are an important adjustment mechanism for forcing in the ocean circulation (OLBERS *et al.*, 2012) and its restoring force is due to the so-called planetary vorticity gradient.

In a flat-bottom, Boussinesq, hydrostatic, linear barotropic ocean with no mean flow, the quasi-geostrophic (QG) approximation yields the QG potential vorticity (hereafter PV) conservation:

$$\begin{aligned} &\tfrac{Dq}{Dt} = 0\,, \\ &\tfrac{\partial}{\partial t}(\nabla^2 - R_{de}^{-2})\psi + \beta\tfrac{\partial \psi}{\partial x} = 0\,, \end{aligned} \tag{1.1}$$

where $q = \nabla^2\psi - R_{de}^{-2}\psi + \beta y$, $R_{de} = \frac{\sqrt{gH}}{f_0}$ is the external deformation Rossby radius and $\psi = \frac{g}{f_0}\eta$ is the streamfunction.

Assuming a wave solution for ψ, the dispersion relation for a barotropic Rossby wave is obtained:

$$\omega = \frac{-\beta k_x}{k_x^2 + k_y^2 + R_{de}^{-2}}\,, \tag{1.2}$$

where k_x and k_y are respectively the zonal and meridional wavenumbers.

According to observations made by Polito and Cornillon (1997), the zonal propagation of Rossby waves is far more persistent than the meridional one. That said, the equation (1.2) is reduced to:

$$\omega = \frac{-\beta k_x}{k_x^2 + R_{de}^{-2}}\,. \tag{1.3}$$

Since R_{de} depends on the Coriolis parameter, which in turn is dependent on latitude (Figure 1.1), when ω is maximum, the group speed ($c_g = \frac{d\omega}{dk}$) is zero. It means this is a maximum frequency for the ocean to respond to a disturbance with a Rossby wave. Since c_g carries the energy of these waves, it is implied that it does not propagate. Consequently,

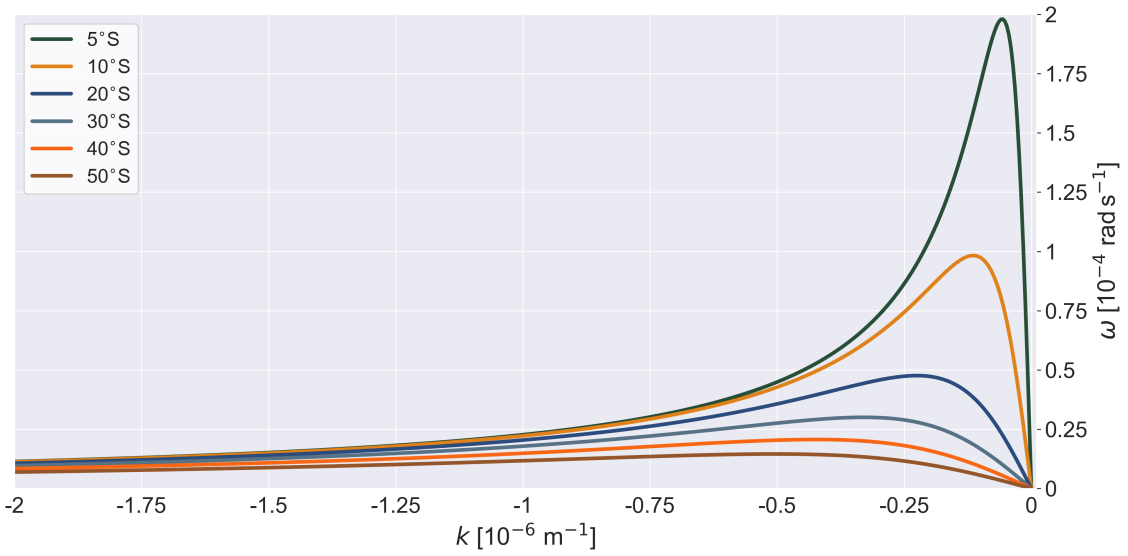

Figure 1.1: Dispersion relation diagram of barotropic Rossby waves at different latitudes.

there is a maximum latitude for the occurrence of the wave, called *critical latitude*.

In long waves, the stretching vorticity term is much larger than the relative vorticity term. In other words, R_{de} is much larger than the horizontal scale of the movement. Therefore, the QGPV equation (1.1) becomes:

$$-\frac{\partial}{\partial t}R_{de}^{-2}\psi+\beta\frac{\partial\psi}{\partial x}=0\,. \tag{1.4}$$

Assuming the same wave solution, we obtain the dispersion relation under long wave approximation (ω_l):

$$\omega_l=-\beta k_x R_{de}^2\,, \tag{1.5}$$

and, therefore, phase ($c_p=\frac{\omega}{k_x}$) and group ($c_g=\frac{\partial\omega}{\partial k}$) velocities:

$$c_{pl}=c_{gl}=-\beta R_{de}^2\,. \tag{1.6}$$

One can notice that long Rossby waves are non-dispersive, since $c_p = c_g$ and both velocities do not depend on the wavenumber k. Its phase speed is always negative, implying westward propagation.

Similarly, for short waves the relative vorticity term is much larger than that of the stretching vorticity, and thus $\omega_s=\frac{-\beta}{k_x}$, and phase and group velocities are $c_{ps}=\frac{-\beta}{k_x^2}$ and $c_{gs}=\frac{\beta}{k_x^2}$ respectively. Unlike long waves, c_p is dependent on k, which makes short waves dispersive. It is also easy to note that phase and group propagate in opposite directions.

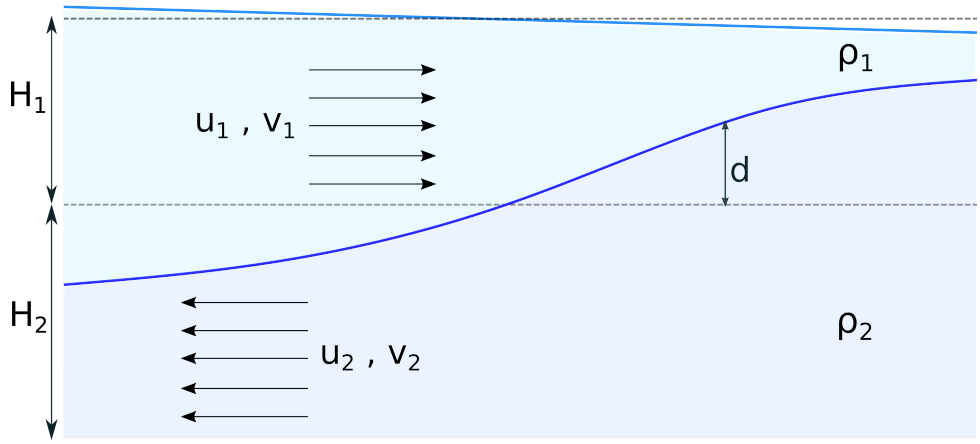

Figure 1.2: First baroclinic mode schematics for a two-layer ocean, adapted from Cushman-Roisin and Beckers (2011). The interface (d) and sea surface elevation are in opposite phase. Velocities (u_1,v_1 and u_2,v_2)create no net transport, having opposite directions in each layer ($\rho_1 \neq \rho_2$).

In a two-layer model, we introduce a stratified system by including the reduced gravity defined as $g' = \frac{\Delta\rho}{\rho} g$ but maintain equations and variables to a minimum. For a barotropic flow, the surface is nearly rigid and the flow is vertically uniform, behaving as if the aforementioned density difference is absent. Different from the barotropic counterpart, the baroclinic flow is vertically variant due to horizontal density gradients, also known as the thermal wind relations. Moreover, for a baroclinic ocean the external deformation Rossby radius is replaced by the internal radius, that is $R_{di} = \frac{1}{f_0}\sqrt{\frac{g'(H_1 H_2)}{H_1+H_2}}$ (CUSHMAN-ROISIN; BECKERS, 2011), being H_1 and H_2 the thickness of each layer (Figure 1.2), and $H = H_1 + H_2$. In this case, η is given by

$$\eta = -\frac{dH_2}{H}\frac{g'}{g} = -\frac{dH_2}{H}\frac{\Delta\rho}{\rho}. \tag{1.7}$$

In other words, η variations are directly related to the interface displacements (d) multiplied by a factor given by $-\frac{\Delta\rho}{\rho}$.

When the number of layers increase, the number of modes increase accordingly, and for an infinite number of layers we shall have infinite vertical modes, constituting a continuous stratified ocean. Density varies over time and in horizontal and vertical coordinates. From density conservation:

$$w\frac{\partial\overline{\rho}}{\partial z} + \frac{D\rho'}{Dt} = 0\,, \tag{1.8}$$

and introducing the squared Brunt-Väisälä frequency,

$$N^2 = -\frac{g}{\rho_0}\frac{\partial\overline{\rho}}{\partial z}\,, \tag{1.9}$$

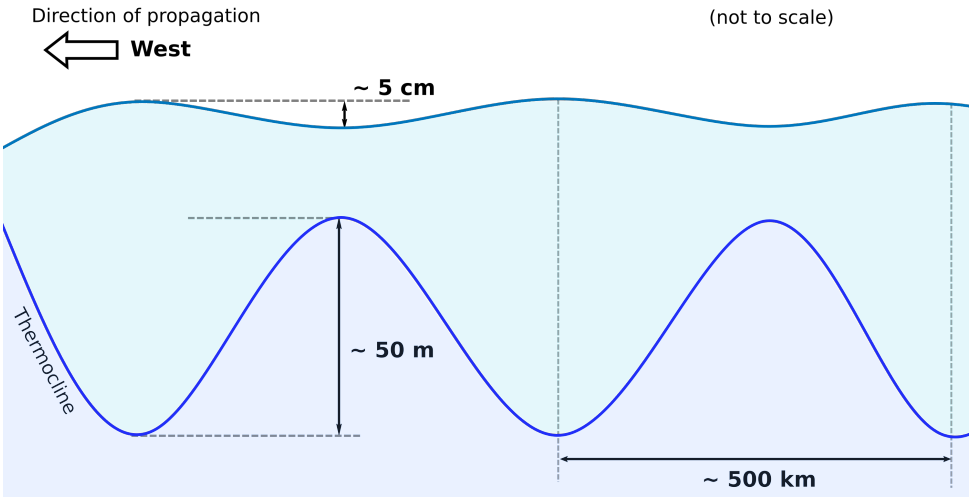

Figure 1.3: Schematic of a first baroclinic Rossby wave, not to scale, adapted from Cipollini *et al.* (2000).

the QG potential vorticity equation for a baroclinic ocean is:

$$\frac{D}{Dt}(\nabla^2\psi+\beta y)-\frac{\partial}{\partial z}\left(\frac{f_0}{N^2}\frac{D}{Dt}\frac{\rho'}{\rho_0}g\right). \tag{1.10}$$

Rearranging the terms of equation (1.10):

$$\begin{aligned}&\tfrac{Dq}{Dt}=0,\\&q=\nabla^2\psi+\beta y+\tfrac{\partial}{\partial z}\left(\tfrac{f_0^2}{N^2}\tfrac{\partial\psi}{\partial z}\right).\end{aligned} \tag{1.11}$$

The internal Rossby deformation radius for a continuously stratified ocean is inherently related to stratification, due to is dependence on the Brunt-Väisälä frequency. As in the previous case, equation (1.11) admits wave solutions and the dispersion relation, analogous to the barotropic case (Equation 1.3), becomes

$$\omega=-\frac{\beta k_x}{k_x^2+R_{di}^{-2}}. \tag{1.12}$$

First mode baroclinic Rossby waves can be generated locally, forced by wind stress curl, or remotely due to disturbances in thermocline/pycnocline height (Figure 1.3) at the eastern border of ocean basins (WATANABE *et al.*, 2016). These disturbances are three orders of magnitude higher and in opposition of phase of surface disturbances (OLIVEIRA; POLITO, 2013).

The relationship between the wave amplitude at the surface and at the pycnocline is controlled by stratification (e.g. Equation 1.7). Thus, if one knows the stratification, the internal expression of the wave as a function of depth can be unraveled from the

satellite derived sea surface height anomaly. For example, supposing that the interface displacements d in equation (1.7) in two different basins, e.g.: Pacific and Atlantic, are equal but their stratification profiles are different, the factor $\frac{\Delta\rho}{\rho}$ would control the surface signature. In other words, different stratification profiles would give different sea surface height signatures. Therefore, η would differ in the two basins considered.

Using a time series of 9 years, Polito and Liu (2003) studied propagating features by analyzing global sea surface height anomaly from the TOPEX/Poseidon altimeter. The authors filtered the surface field for each latitude and characterized Rossby waves globally. One of their findings is related to the discrepancies of waves' amplitudes in the three ocean basins, specially in mid-latitudes, being the Atlantic the basin with the weakest Rossby wave signal. Overall, their waves are in agreement to the linear theory showing that the average Rossby wave signal is in the form of free waves. The generation of these waves is strongly related to variations in the PV field, which in turn can be influenced by wind movements. However, the mean wind regime is similar for the three ocean basins (GILL, 1982; LEE *et al.*, 2013), so the question that remains is why this difference in waves' amplitudes occur, given that the forcing is similar.

1.3 Hypotheses and objectives

As previously discussed, the biggest motivation to conduct this study is the relationship between the sea surface height anomalies we can see from space and the isopycnal displacement, obtained from satellites and predicted from ocean modeling. In Chapter 2, we attempt to reconstruct the surface streamfunction using a realistic Brunt-Väisälä frequency to compute a numerical solution to identify which solution – traditional QG or SQG – is dominant at 11°S, 24.5°S e 34.5°S and if this dominance persists in a time series of 14 years. In other words, the main objective was to evaluate what the altimeter is actually observing: the barotropic and first baroclinic modes, claimed by several authors (WUNSCH, 1997; STAMMER, 1997) or a surface solution, discussed by LeTraon *et al.* (2008), Lapeyre (2009) and LaCasce (2017). Thus, the first hypothesis is:

$\mathbf{H}_1$: The dominance of the QG modes or SQG solutions at 11°S, 24.5°S and 34.5°S to the reconstruction Atlantic's sea surface height is directly related to the amplitude of mesoscale motions in each area;

In Chapter 3, two hypotheses were brought into light. The first one concerned the discussion in the study of Meinen *et al.* (2017), whether the signals detected at 34.5°S were

related to mesoscale eddies or Rossby waves. Therefore, the second hypothesis is as follows:

$\mathbf{H}_2$: Most of the variability of the sea surface height associated to propagating signals at 11°S, 24.5°S e 34.5°S is explained by Rossby waves;

The third one is related to the fact that disparities in Rossby waves' amplitudes were seen in different studies, e.g.: Polito and Liu (2003), although atmospheric forcing is similar between ocean basins. That is:

$\mathbf{H}_3$: Rossby waves' amplitudes measured by altimetric radars on the South Atlantic ocean at mid-latitudes are smaller than the ones in other ocean basins on the Southern Hemisphere due to differences in stratification among the three basins, although the atmospheric forcing present similar amplitudes;

In this context, the main objective is to identify Rossby waves in the latitude ranges of interest, assess their amplitude in the three ocean basins on the Southern Hemisphere to see if they have a smaller surface signature in the Atlantic, although wind forcing is similar. We propose to investigate the differences in stratification and its relation to planetary waves.

Given these hypothesis, the following specific objectives are proposed:

1. Numerically reconstruct the streamfunction (sea surface height) using SQG theory and a realistic stratification profile (squared Brunt-Väisälä frequency) at 11°S, 24.5°S e 34.5°S and assess which theory is the best to characterize sea surface height variability over a 14-year time series;

2. Identify Rossby waves at the latitudes of interest; Separate waves and eddies from the non-propagating signals using bi-dimensional digital filters;

    - Compare the mean wind stress (τ) and its curl in the three ocean basins of the Southern Hemisphere;

3. Assess the waves' amplitudes (A) at several spectral bands, as well as the explained variance associated to each one of them (σ_p^2) in the three ocean basins of the Southern Hemisphere;

4. Apply the QG modal decomposition using salinity and temperature profiles from the In Situ Analysis System (ISAS) dataset and Hybrid Coordinate Ocean Model

(HYCOM) outputs to reconstruct the sea surface height anomaly field η and assess differences in Rossby waves' amplitudes.

Data and methods that are used to fulfill these objectives are described in the corresponding Chapters.

2 What does the altimeter see?

According to Richman *et al.* (1977), mesoscale motions are distributed over the entire ocean on spatial scales between 50 and 500 km and timescales between 20 and 150 days. They are responsible for most of ocean variability, and transport of heat and momentum, being vital to understand ocean circulation and its relation to climate. It is suggested that these features are generated mainly by baroclinic instabilities of boundary currents (MCWILLIAMS *et al.*, 1983) and are radiated by oceanic Rossby waves (PEDLOSKY, 1977). In 1992, Topex/Poseidon was launched to measure sea surface height for studying ocean dynamics and its circulation. Unlike the precedent radars (e.g.: Seasat, GEOSAT, ERS-1), whose data were not sufficiently accurate because they were not projected to study large scale circulation, it presents high accuracy and precision of 2 cm and this was vital to the understanding of surface dynamics (FU *et al.*, 1994). Stammer (1997) provided a regional study on the global wavenumber-frequency spectrum of sea surface height (SSH) variability obtained by three years of altimetric data. To summarize, his results suggested that all spectra showed a plateau at long wavelengths, a power spectral density break around 400 km and a drop in energy close to a k^{-5} relation, following the predictions of horizontally isotropic QG turbulence.

In the same year, Wunsch (1997) first proposed that most regions on the global ocean are dominated by the barotropic and the first baroclinic modes, by studying the vertical wavenumber-frequency spectra of kinetic energy derived from three years of data obtained from the aforementioned satellite. His main idea was to understand the altimetric measurements in terms of elevation and slope, extending the results of Wunsch and Stammer (1995) and Stammer (1997) to the vertical direction. Assuming a linear, resting ocean and a flat bottom — which fails mostly everywhere on the real ocean — he used the annual mean climatology to calculate the dynamical modes. Despite some problematic results, the author concluded that, except the Tropics, the first baroclinic mode dominates the surface kinetic energy in most of the global ocean, meaning that altimeter is reflecting the movement of the main thermocline.

However, what was claimed by Stammer (1997) and Wunsch (1997) have been discussed for several years and 11 years later LeTraon *et al.* (2008) showed that SSH wavenumber spectral slopes in high eddy-energy regions are significantly different from the results of Stammer (1997), as they better follow a $k^{-\frac{11}{3}}$ relation, posing a different scenario when interpreting altimeter data. This smaller spectral slope is in accordance to the so-called Surface Quasi-Geostrophy (SQG) theory, first developed by Held *et al.* (1995). In general, the SQG theory is a model that describes surface intensified flows due to buoyancy. It assumes that there are no PV anomalies in the interior, and the flow is driven by a quantity distribution, in this case, density anomalies. The solutions are exponential-decaying profiles, intensified near the surface. If one assumes a flat surface, no upper boundary (rigid lid condition) and constant stratification, the equations would be exactly as predicted by QG theory. A detailed explanation on assumptions and equations will be addressed later on this Chapter and on Appendix A.

Since horizontal and vertical structures are related in SQG theory, it can be invoked in studies relating satellite data to numerical model outputs, e.g.: Isern-Fontanet *et al.* (2006), LaCasce and Mahadevan (2006), LeTraon *et al.* (2008), Lapeyre (2009), Wang *et al.* (2013). It has been shown (ISERN-FONTANET *et al.*, 2006, 2008; LAPEYRE, 2009; ISERN-FONTANET *et al.*, 2014) that a variety of fields can be reconstructed in a 3D framework from surface information, such as SSH and geostrophic velocities. In the study of Isern-Fontanet *et al.* (2006), the authors reconstructed surface ocean currents using microwave radiometer sea surface temperature (SST) data to complement the altimeter. They showed a very robust relationship when applying SQG to relate SST and SSH fields, being the highest correlations at wavelengths between 100 and 300 km.

A different approach was taken by Lapeyre and Klein (2006), who have posed the relation between the surface and interior dynamics in a nonlinear, baroclinic and unstable flow. They found out that there is a dominance of the SQG solution over the interior, classical QG in the upper oceanic layers of a simulation of the Antarctic Circumpolar Current. As stated by the authors, the dynamics of interior and surface layers are in a different dynamical balance, meaning that the surface is governed by the progression of density anomalies in a time basis, and there are no interior PV anomalies. Since traditional baroclinic modes do not represent the free surface motion, one can argue that they do not represent well the surface dynamics. Thus, normal QG modes may lack relevant information from the ocean surface.

LeTraon *et al.* (2008) assessed whether the altimeter wavenumber spectra in the Gulf

Stream, Kuroshio, and Agulhas regions agreed with the interior, traditional QG or SQG theory and concluded SQG is a much better scenario to interpret surface dynamics. Their results show that altimeter spectral slopes are better represented by SQG theory, in agreement with both theoretical results and numerical simulations for high eddy energy areas. They also showed SQG dynamics extend from $O(10 - 10^2)$ km, consistent to the mesoscale and corroborating Isern-Fontanet *et al.* (2006).

One year later, Lapeyre (2009) argued that QG modes alone are incomplete, and added an explicit term to characterize the surface mode. This surface-trapped solution depended on a transfer function and on the wavenumber and it is not orthogonal to the QG modes. The author used the output of a numerical simulation of the Atlantic and found that the surface mode contribution was as large as the first baroclinic mode at the surface layers, especially in areas where eddy kinetic energy is high. According to the author, the altimetric signal may be related to both traditional first baroclinic and surface-trapped modes. Beside large-scale density forcing, it seems that this relationship depends on how energetic the study area is, since the surface flow in the most energetic part of North Atlantic reflected the surface mode. Generally speaking, the barotropic and first baroclinic modes dominate in most of their study area because of the first baroclinic near-surface intensification, being captured by the altimeter and thus representing the motion of the main thermocline.

Different from Lapeyre (2009) – who solved the problem numerically – LaCasce (2012) considered the QG solution set as complete and orthogonal. Using an exponential stratification, the author found how the SQG solutions projects onto the traditional QG modes. There are some discrepancies between these authors regarding the interpretation of SQG solutions, however both argue that this approach may be better than the traditional QG modes in determined regions. In this context, rose the idea of assessing whether the altimeter is featuring traditional QG or the surface solution in the South Atlantic. Is this result related to the energy contained in the area? Or large-scale forcing, i.e. Rossby waves? Is this dominance persistent along the years?

Hence, how the surface fields (e.g.: sea surface height) respond to the dynamics and reflect the motion at depth remains to be understood. The main idea in this Chapter is to apply the SQG theory and reconstruct SSH fields to the mesoscale band (30 – 400 km) and assess whether the dominance is given by the surface or the interior solution. Using a non-constant $N^2(\mathrm{z})$ profile in the South Atlantic ocean, we extend the results obtained with HYCOM-NCODA outputs to the signal captured by the altimeter, relating them to

traditional QG or SQG solutions to test hypothesis H_1.

2.1 The relationship between altimetry and model outputs

The sea surface height anomaly data (AVISO/CMEMS, *Archiving, Validation and Interpretation of Satellite Oceanographic data*) comes from two series of altimetric satellites, NASA (National Aeronautics and Space Administration) and ESA (European Space Agency). These data were corrected, interpolated and distributed by the group AVISO / CMEMS, with spatial resolution of 0.25° and temporal resolution of 1 day. To obtain height estimates, these altimeters operate in the Ku (13.6 Hz) and C (5.3 Hz) bands respectively, being the first group slightly more accurate. The across-track resolution in the Equator is 315 km and in the Poles is 90 km, with an exact repeating cycle of approximately 10 and 35 days, respectively. In both cases the along-track resolution is 7 km.

In general, the sensor emits a radar pulse of known speed and measures the time it takes to be reflected from the ocean surface and to be picked up again by the sensor. Thus, the velocity and time values allow to calculate the distance between the ocean surface and the sensor in relation to the sea surface. To achieve the desired distance resolution, a signal processing technique called pulse compression is used (ROBINSON, 1995). In more detail, altimetric measurements are also based on distortion of the electromagnetic pulse to increase the accuracy of the distance measurement; they also require vertical geoid referencing (JGM-3/OSU91A) so that the sea surface height anomaly is associated with the mean geostrophic currents. In addition, the available dataset already features geophysical corrections (wet and dry troposphere, free electrons in the ionosphere, geoid), wave influence corrections (tides, sea state, electromagnetic bias), inverted barometer effect and corrections for compatibility between various instruments (AVISO/ALTIMETRY, 1996).

However, these nadir looking altimeters can resolve roughly horizontal scales down to 100 km, which poses a problem when dealing to finer scales. Since the SQG theory extends from the $O(10 - 10^2)$ km (mesoscale), a full reconstruction would need a much better resolution. Therefore, to maintain the consistency on scales when applying the SQG theory, we used the SSH fields derived from HYbrid Coordinate Ocean Model (HYCOM) outputs. Besides SSH, we used temperature (T) and salinity (S) profiles, that provide a density field consistent with the modeled SSH.

HYCOM is sponsored by the National Ocean Partnership Program (NOPP), as part of the U. S. Global Ocean Data Assimilation Experiment (GODAE) to develop and evaluate a data-assimilative hybrid isopycnal-sigma-pressure (generalized) coordinate ocean model. The chosen dataset is the reanalysis 53.X and uses the Navy Coupled Ocean Data Assimilation (NCODA) system for data assimilation, which includes the assimilation of available satellite altimeter observations, satellite, and *in-situ* sea surface temperature as well as *in-situ* vertical temperature and salinity profiles from XBTs, Argo floats and moored buoys. It is also worth mentioning that this experiment does not include tidal forcing. The advantage in choosing reanalysis outputs reside precisely in the assimilation of real observations, complementary to the numerical model, so that profiles would be physically consistent to variations in the sea surface height field.

HYCOM-NCODA outputs (hereafter HYCOM) have temporal resolution of 3 hours and spatial resolution of around 30 km. Its grid is better than that of the altimeter dataset, 0.08°, which is approximately 10 km and it is capable of producing physically consistent fields with variability in spatial and temporal scales smaller than that observed by satellite altimeters. Even if we cannot discuss these scales in terms of altimetry, HYCOM can provide an idea of what the altimeter is missing, and what could be done and identified in terms of mesoscale if the altimeter's resolution is improved. The SSH fields derived from HYCOM are similar to those of the altimeter, but have less noise and it is richer in terms of the spectral point of view. Therefore, HYCOM can be used as a proxy of altimetric data.

To assess whether the sea surface height from HYCOM is a good representation of the altimetric measurements, a cross-correlation was performed in a time series common to both at 15°N on the Pacific ocean, from 1994 to 2015. HYCOM SSH was converted in SSH anomaly and was bicubically re-gridded to match the AVISO data (see Appendix B for further details). Since HYCOM outputs incorporate data from AVISO/CMEMS, we expected a high correlation between the two sea level anomaly fields. Results suggest a good correspondence between them (Figure 2.1) as the correlation was, on average, 0.8 over the Hovmöller diagram, statistically significant (p-value = 0). Therefore, we have confidence to draw conclusions about the sea surface fields seen by the altimeter using HYCOM outputs in the mesoscale range, at least from around 100 km and larger wavelengths.

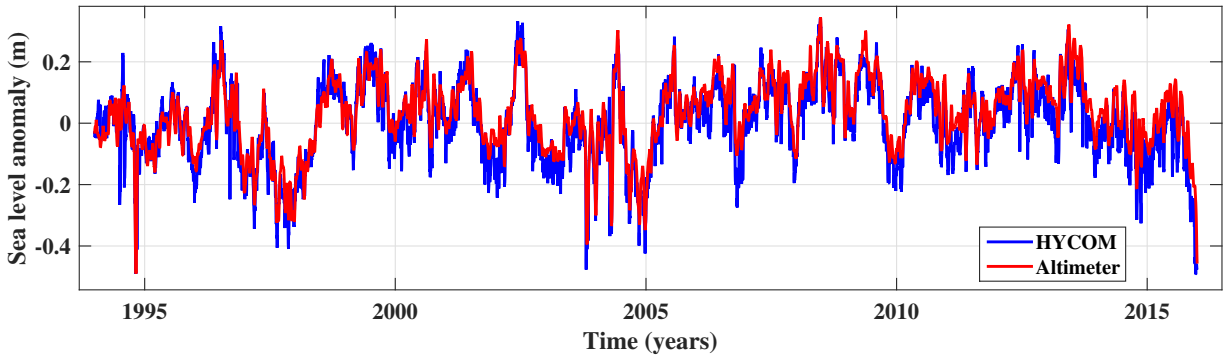

Figure 2.1: Time-series of HYCOM (blue) and altimeter (red) SSH anomaly, fixed at 15°N and 130°E from 1993 to 2015 on the Pacific ocean; correlation is 0.9 (p-value = 0).

2.2 On the decomposition of vertical modes

In QG theory, knowing the surface buoyancy and interior PV, one can reconstruct 3D dynamics by inverting the equation:

$$q = \nabla^2 \psi + \frac{\partial}{\partial z}\left(\frac{f_0^2}{N^2}\frac{\partial \psi}{\partial z}\right) \tag{2.1}$$

where q is the PV anomaly, ψ the flow streamfunction, f_0 the Coriolis parameter and N^2 the squared Brunt-Väisälä frequency as defined in Section 1.2, equation (1.9). The appropriate boundary condition at the surface comes from the hydrostatic equation, that is:

$$f_0 \frac{\partial \psi}{\partial z} = b_s, \; at \; z = \; 0, \tag{2.2}$$

where b_s is the surface buoyancy given by $\frac{-g}{\rho_0}\rho$. ρ_0 is a reference density and ρ the density 2D field at the surface. At the bottom ($z = -H$), we have:

$$\frac{\partial \psi}{\partial z} = 0. \tag{2.3}$$

The system of equations (2.1), (2.2) and (2.3) can be split in two solutions. The first one is governed by surface quasi-geostrophy (HELD *et al.*, 1995) and assumes no interior PV and allows horizontal density variations. In other words, $q = 0$ and $b_s \neq 0$ and one can obtain the surface streamfunction (ψ_{sqg}). This solution is associated to frontogenesis without ageostrophic movements, in this case the buoyancy anomalies are advected leading to the stirring of its contours and the development of horizontal fronts (LAPEYRE; KLEIN, 2006). The second solution is related to the interior (ψ_{int}), obtained by allowing PV anomalies in the interior and assuming no surface buoyancy, that is $q \neq 0$

and $b_s = 0$.

The modal decomposition rises from the separation of variables of the linearized conservation of PV equation (Equation 1.1). For the QG modes, i.e. the interior solution, the vertical equation is:

$$\frac{\partial}{\partial z}\left(\frac{f_0^2}{N^2}\frac{\partial F_i}{\partial z}\right) = -\lambda_i^2 F_i, \tag{2.4}$$

where $F_i(z)$ is the vertical structure for each mode, also called transfer function, and $-\lambda_i^2$ are the separation constants, also the eigenvalues, defined as the inverse of Rossby deformation radii squared. The appropriate boundary conditions at the surface ($z = 0$) and at the bottom ($z = -H$) are:

$$\frac{\partial F_i}{\partial z} = 0, \tag{2.5}$$

Equations (2.4) and (2.5) constitute a Sturm-Liouville problem, F_i being the eigenvectors and λ_i the eigenvalues. To assess this problem, we assume rigid lid condition (Equation 2.5), no mean flow, flat bottom and a linear ocean. These simplifying assumptions break down over most of the world's ocean. However, a bit of solace comes from the results of Watanabe *et al.* (2016), in that the linear Rossby wave mode explains most variance at mid-latitudes. With that in mind, we proceed treating this as a linear problem.

As for the SQG, the vertical structure of the surface solution is given by (LACASCE, 2012):

$$\frac{\partial}{\partial z}\left(\frac{f_0^2}{N^2}\frac{\partial \chi}{\partial z}\right) = k^2\chi \tag{2.6}$$

where $k = \sqrt{k_x^2 + k_y^2}$ is the wavenumber magnitude and χ is a transfer function analogous to F_i. The boundary conditions are slightly different:

$$\frac{\partial \chi}{\partial z} = 1, \; at \; z \; = \; 0\,, \tag{2.7}$$

and

$$\frac{\partial \chi}{\partial z} = 0, \; at \; z \; = \; -H\,. \tag{2.8}$$

Since these solutions are dependent on the wavenumber magnitude k, the equation system (2.6), (2.8) and (2.7) does not form an eigenvalue problem.

Many authors (PEDLOSKY, 1987; GILL, 1982; MCWILLIAMS, 2006) have addressed modal decomposition using a constant N^2. Others (PEDLOSKY, 2003; LACASCE, 2012; LACASCE; WANG, 2015) have opted to use an exponential approxi-

mation. Although depth-variant, this exponential approximation – as well as N^2 constant – are not very realistic when representing the stratification of the water column. Hence, we have decided to use realistic N^2 profiles to numerically calculate the vertical modes, assuming a continuously stratified ocean.

Because of the ongoing debate on which vertical structure solution (SQG or QG) is better related to the information provided by the altimetric satellites, we decided to address this question by reconstructing numerically the streamfunction ψ related to the SQG using a depth-variant N^2 and compare the result with the interior streamfunction, to see which solution is dominant and captured by HYCOM at the surface. Then, given the correlation between the altimeter and the data-assimilating model, we can relate the result to the satellite observations. According to Wang *et al.* (2013), the sea surface height (η) has contributions from both the interior (ψ_{int}) and the surface (ψ_{sqg}) solutions. At the surface:

$$\psi = \psi_{sqg} + \psi_{int} = \frac{g}{f_0}\eta\,. \tag{2.9}$$

Provided we have η, from HYCOM, and ψ_{sqg}, from our numerical solution, we obtain ψ_{int} as the residual of equation (2.9).

To quantify the dominance of a solution, we define:

$$\gamma = \sqrt{\frac{\sum \psi_{sqg}^2}{\sum(\psi - \psi_{sqg})^2}}\,, \tag{2.10}$$

where ψ is given by $\frac{g\eta}{f_0}$ since we are in a QG framework. If $\gamma > 1$, the dominance of the surface dynamics is given by the surface solution. On the other hand, if $\gamma < 1$, this means that the interior solution dominates. Values equal to 1 means the same importance on both solutions. Our main idea is to test whether the simplified QG – SQG solutions fit our model results.

2.3 Fourteen years of sea surface height reconstruction

2.3.1 SQG solutions in the South Atlantic Ocean

To reconstruct the sea surface height fields, we invoked the SQG theory. This is a particular situation where the flow is completely determined by density variations at the surface, assuming that the interior PV is constant. This implies that the smaller horizontal scales vertically decay faster than the larger ones (ISERN-FONTANET *et al.*, 2008).

In this case, we assume that PV anomalies in the lower layers have little influence in the upper dynamics (LAPEYRE; KLEIN, 2006). The method employed is inserted in a quasi-geostrophic framework and inverts the PV equation (2.1) (HOSKINS *et al.*, 1985) associated with density anomalies, assuming a regional average of realistic N^2 profiles and f_0 (WANG *et al.*, 2013).

According to Lapeyre and Klein (2006), both buoyancy anomalies and mesoscale PV can be forced by baroclinic instabilities at large scales. The authors put forward that the interior PV in the upper ocean is correlated to b_s, so that for the first 500 m a "surface-trapped" solution would be a good representation of the total streamfunction. Thus, velocities can be diagnosed from a single snapshot of sea surface temperature, which was explored by Isern-Fontanet *et al.* (2008). These authors defined an "effective" SQG — a modified version of the SQG equations with constant N^2 — to reconstruct the 3D dynamics of the upper ocean, and showed that the reconstruction of the velocities and vorticity fields is good up to 500 m. The correlation between PV and b_s also means that ψ_{sqg} and ψ_{int} will present correlated spatial features, differing only at the vertical (ISERN-FONTANET *et al.*, 2008).

The SQG is a reduction of the Eady's baroclinic instability model to one boundary, i.e. the surface (LAPEYRE, 2009). As previously mentioned, this model is associated to frontogenesis, since density anomalies are stirred by mesoscale eddies, leading to strong gradients at submesoscale. Thus, in SQG, the time evolution surface buoyancy drives surface dynamics and a solution to ψ_{sqg} would be given by:

$$\hat{\psi}_{sqg}(\mathbf{k}, z, t) = \chi(k, z)\, \hat{b}_s(\mathbf{k}, t)\,, \tag{2.11}$$

where $\mathbf{k} = (k_x, k_y)$ is the wavenumber vector and the hat stands for the Fourier transform. Thus, the next step is to obtain b_s and χ from T and S profiles.

We selected three areas in the Atlantic ocean so that the latitudes of interest, namely 11°S, 24.5°S and 34.5°S, would be in the center of a 6° meridional length box, zonally extended to comprise the whole basin. Then, these areas are split in another four (Figure 2.2, Table 2.1), that is: western boundary (WB), western and eastern interior oceans (WOF and EOF) and eastern boundary (EB). Using the Thermodynamic Equation of Seawater (TEOS-10), T and S from HYCOM are converted to conservative temperature and absolute salinity and potential density and N^2 profiles are calculated. Then, for each box, these profiles are vertically cubic interpolated to have equal spacing (10 m) and averaged to have a 7-day resolution. The result is one smooth $N^2(z)$ profile every week for each

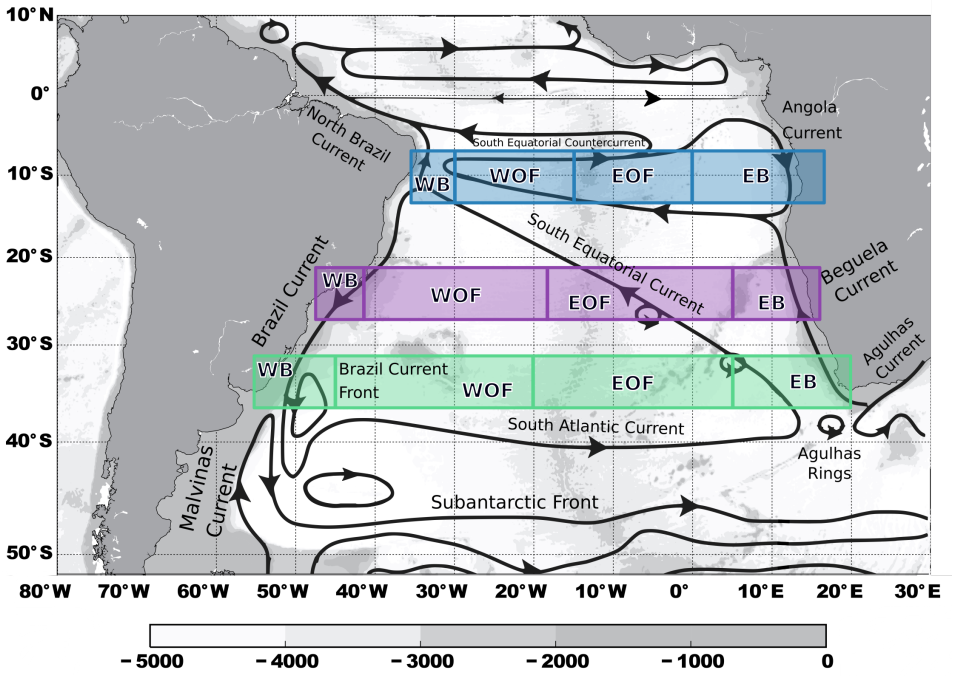

Figure 2.2: South Atlantic large-scale upper-level geostrophic circulation, adapted from Talley *et al.* (2011). Sections at 11°S (blue), 24.5°S (purple) and 34.5°S (green) used for SSH reconstruction. **WB** stands for western boundary, **WOF** and **EOF** represents western and eastern ocean interior and **EB**, eastern boundary.

area. The reconstruction of ψ_{sqg} is made for each area for a time series of 14 years, from 2002 to 2015.

Following LaCasce (2012) and Wang *et al.* (2013), the numerical transfer function χ is calculated according to the theoretical framework provided in Section 2.2 for each N^2 profile. A detailed description of the numerical resolution of the transfer function χ is given in Appendix A.2. Once the values of χ are obtained, we can reconstruct ψ_{sqg} for each weekly snapshot of surface buoyancy in the Fourier domain, provided the field is doubly periodic. Each box was extended in (x,y) direction with mirror symmetry to avoid discontinuities and minimize errors in the Fourier analysis, as in Isern-Fontanet *et al.* (2006). Besides that, a bandpass Lanczos filter was applied to retain wavelengths in accordance to the SQG theory, that is $O(10 - 10^2)$ km.

The same method was applied to a constant N^2 profile to test the accuracy of the numerical solution. Since both the stream and transfer functions (ψ_{sqg} and χ, equation 2.11) are known, we compared the numerical solution with the analytical one. For a constant N^2 profile (see Appendix A.2), the numerical solution gives a correct result, therefore it can be applied to the areas of interest using depth-variant N^2 profiles.

Table 2.1: Study areas' latitudinal and longitudinal limits.

Areas	Latitude	Longitude
WB	8°S – 14°S	34.5°W – 30°W
	21.5°S – 27.5°S	47°W – 42°W
	31.5°S – 37.5°S	55°W – 45°W
WOF	8°S – 14°S	30°W – 15°W
	21.5°S – 27.5°S	42°W – 18°W
	31.5°S – 37.5°S	45°W – 20°W
EOF	8°S – 14°S	15°W – 0°
	21.5°S – 27.5°S	18°W – 5°E
	31.5°S – 37.5°	20°W – 5°E
EB	8°S – 14°S	0° – 15°E
	21.5°S – 27.5°S	5°E – 15°E
	31.5°S – 37.5°	5°E – 20°E

2.3.2 Eddy kinectic energy and wavenumber spectra: a review

According to Ponte and Klein (2013), this reconstruction may not be representative everywhere. If the surface density anomalies are weak, their signature on upper-ocean dynamics would be small, or even non-existent. Thus, both interior and surface solutions may be applied simultaneously and partition the variance of the upper layers. The validity of SQG in reconstructing SSH fields implies a SSH spectrum with slopes of $k^{\frac{-11}{3}}$ (ISERN-FONTANET *et al.*, 2014), and according to LeTraon *et al.* (2008) one should invoke SQG theory in high eddy energy areas. Therefore, we expect a good reconstruction in the mesoscale range where eddy-energy is high in mid-latitudes.

Upper-ocean dynamics can be retrieved from SSH and N^2 if assuming that SSH is reflecting the first baroclinic mode (SMITH; VALLIS, 2001). However, there are some limitations on this reconstruction. The first one is related to depth: Isern-Fontanet *et al.* (2008) showed that the correlations between fields of the POP model and the SQG reconstruction using surface fields decreases with depth. For a correlation of 0.7, the reconstruction method is good up to 500 m, on average. The second is related to the type of forcing that is generating the flow: Lapeyre and Klein (2006) argue that SQG should dominate when baroclinic instability is driven by large-scale meridional gradients. Thus, QG theory should prevail near strong baroclinic currents, although there are many other processes that play an important role at mesoscales (ROCHA *et al.*, 2016).

One of the approaches to see whether SQG or QG theories are better to describe upper dynamics is to evaluate SSH wavenumber spectra. Xu and Fu (2012) have identified that for the 70 – 250 km range, the altimeter SSH wavenumber spectra decays different from

the predicted by QG theory, which is k^{-5}. LeTraon *et al.* (2008) analyzed the slopes at high eddy energy areas (Gulf Stream, Kuroshio and Agulhas regions) and concluded that the altimeter SSH wavenumber spectra follow a $k^{\frac{-11}{3}}$ relation, close to SQG predictions. This was also confirmed by Dufau *et al.* (2016) and Hosoda *et al.* (2015). However, these results seem to be inconsistent to in situ observations, which may be due to, among other features, altimeter noise (WANG *et al.*, 2010). Between 20°N – 20°S and at low energy eastern regions, the wavenumber spectral slopes falls between k^{-1} and k^{-2} (DUFAU *et al.*, 2016), which departs from both theories. These values were attributed to internal gravity waves, tides and atmospheric forcing (RICHMAN *et al.*, 2012; DUFAU *et al.*, 2016; ROCHA *et al.*, 2016). In these regions, the kinetic energy related to eddies would be masked by the kinetic energy attributed to non-balanced motions, e.g.: internal waves (TCHILIBOU *et al.*, 2018), and some of this energy could be attributed to tides (DUFAU *et al.*, 2016). Using a varying mesoscale wavelength range, Vergara *et al.* (2019) revisited the global SSH wavenumber spectra. After removing the internal tide signal in a region covering most of the South Atlantic, the authors found an increase in the spectral slope of about 38%. Then, accounting for these motions could signify changes in spectral slopes, and therefore in QG or SQG dominance over the South Atlantic.

In general, the slopes are flatter than both theories predict over the entire ocean. Using HYCOM outputs, Richman *et al.* (2012) presented three main reasons for that fact: (i) the presence of internal tides, (ii) altimeter noise and (iii) shift of the inertial sub-range to smaller scales. The authors compared the HYCOM SSH spectral slopes with the ones derived from the study of Xu and Fu (2012) and with both QG and SQG predictions. For high-eddy energy regions, their results corroborate LeTraon *et al.* (2008). However, when eddy activity is weak and internal tides are strong (e.g.: southeast Pacific, away from western boundary currents), the spectral slope fall between SQG and QG predictions. Also, they have found regions with much flatter slopes, departing significantly from what was expected for both QG and SQG.

Still according to Richman *et al.* (2012), although assimilating satellite data, the spectral slopes from HYCOM differed significantly from those from the altimeter. This is probably due to the misinterpretation between long internal tides and mesoscale eddies made by the altimeter. This happens because they have similar length scales, which makes their separation in a single snapshot in the altimeter signal a challenge. Besides, altimeter data contain noise. The authors observed that if the altimeter noise is corrected, the SSH slopes are in agreement to HYCOM'(RICHMAN *et al.*, 2012, see Figure 10). Thus, ac-

cording to the authors, the spectral slopes alone are not sufficient to confirm SQG or QG dominance, one should take into account energy and dissipation cascades as well.

Vergara *et al.* (2019) and Richman *et al.* (2012) pointed out that many studies (LE-TRAON *et al.*, 2008; DUFAU *et al.*, 2016) have fixed the mesoscale range to compute the wavenumber spectra. However, the length scale of eddies varies according to the Rossby radius of deformation. When computing our numerical reconstruction of the SSH, there was no difference in setting the filter lower limit according to the R_{di} at each latitude; results differed only at the third decimal place. This is an indication that HYCOM is not resolving the smaller scales. Therefore, we chose to maintain the lower limit in 12 km at all latitudes, which is also in accordance to Lapeyre and Klein (2006).

At the western boundary region of 11°S (blue WB, Figure 2.2), the South Equatorial Current (SEC) bifurcates to give rise to the North Brazil Current, that flows to the north, and the Brazil Current (BC), to the south (purple and green WB, Figure 2.2), being the former stronger. Stratification in this region strongly responds to atmospheric forcing and the variability of surface fields is influenced by a variety of processes involving a large range of scales. Most of the water carried by SEC feeds the North Brazil Current, and only 4 Sv goes to the BC. Besides, much of the transport in the northern part of the South Atlantic Subtropical gyre is lost to the northern Hemisphere and to equatorial currents, which explains why BC is the weakest of the global western boundary currents (PETERSON; STRAMMA, 1991).

Moreover, its transport remains small when moving south (PETERSON; STRAMMA, 1991). South of 24°S, BC is intensified at a rate of 5% every 100 km (GORDON; GREENGROVE, 1986) and south of 30°S this intensification may be associated to a re-circulation cell, which carries around 12 Sv above 1400 m. Thus, at 33°S, transports are around 18 Sv (GORDON; GREENGROVE, 1986). Near the Brazil-Malvinas Confluence, one interesting feature is the so called Brazil Current Front (BCF) (purple and green WOF, Figure 2.2), confined to the western Atlantic, first seen by Roden (1986). This front is characterized by sharp thermohaline gradients in the upper layers and large vertical shears of horizontal velocities, leading to a strong baroclinic flow.

At the eastern boundary of 11°S (blue EB, Figure 2.2), there is a cyclonic geostrophic gyre, extending from 10 – 20 m up to 300 m and with subsurface velocities of about 50 cms^{-1} (PETERSON; STRAMMA, 1991). It has a weak baroclinic expression, and the surface speed is of about 3 cms^{-1} (GORDON; BOSLEY, 1990). In the eastern boundary at 24.5°S and 34.5°S (purple and green EB, 2.2), the Benguela Current flows north-

ward, and as the region suggests is the eastern boundary current of the South Atlantic subtropical gyre. According to Peterson and Stramma (1991), this current is fed by the South Atlantic Current but can also receive waters from the Agulhas Current as well. Besides, eddies generated by the Agulhas Retroflection propagate west-northwest between 25.5°S and 35.5°S, and this region is known as the Agulhas eddies propagation corridor (GARZOLI; GORDON, 1996; GUERRA *et al.*, 2018). Pegliasco C. and Morrow (2015) showed that there are several eddies generated at the South Atlantic eastern boundary due to coastal dynamics and probably due to the aforementioned eddy corridor, especially between 15°S and 40°S and east of 10°W. Some of these eddies are found to be strongly subsurface intensified, especially between 20°S and 30°S. If the mesoscale eddies are subsurface intensified (or have no density anomalies) the SQG reconstruction will fail (ISERN-FONTANET *et al.*, 2008). Therefore, we expect a larger contribution of ψ_{int} and QG dominance at 24.5°S in this region.

The Brazil Current present high eddy energy, while lower values are found near the boundary of the subtropical gyre (WYRTKI K.; HAGER, 1976). High eddy energy is associated to strong, western boundary currents. Aguedjou *et al.* (2019) have detected mesoscale eddies in the tropical Atlantic using altimeter sea level anomalies and calculated the mean eddy kinetic energy (hereafter EKE) attributed to mesoscale eddies. The authors found the majority of eddies in latitudes between the Equator and 10°S. However, in terms of EKE, the most energetic ones were found in the Equatorial region and in the North Brazil Current (NBC) retroflection. It was also possible to notice in their study low values of EKE ($\sim$ 50 cm^2s^{-2}) over most of the South Atlantic, being the western part below 24°S the most energetic ($\sim$ 200–250 cm^2s^{-2}), which is 4 times higher than 10°S and also corroborates Wyrtki K. and Hager (1976). Moreover, the lifetime of eddies far from the boundaries are high, meaning that EKE would be low due to weak velocities. Close to the western boundary, lifetime drops and EKE increase, especially near 25°S (AGUEDJOU *et al.*, 2019).

Using the geostrophic velocities provided by AVISO, we calculated the South Atlantic EKE (Figure 2.3). Low values (0 – 0.01 J) are found mostly at the center of the subtropical gyre and north of 25°S. From around 20°S, the western boundary increases its EKE due to the meandering and consequently the mesoscale activity associated to the Brazil Current, baroclinic at this latitude. Further south, the Brazil-Malvinas Confluence ($\sim$ 35°S, 55°W – 45°W) and the Agulhas retroflection and leakage regions ($\sim$ 35°S, 5°E – 25°E) are the most energetic regions in terms of EKE (Figure 2.3), reaching more than 0.04 J.

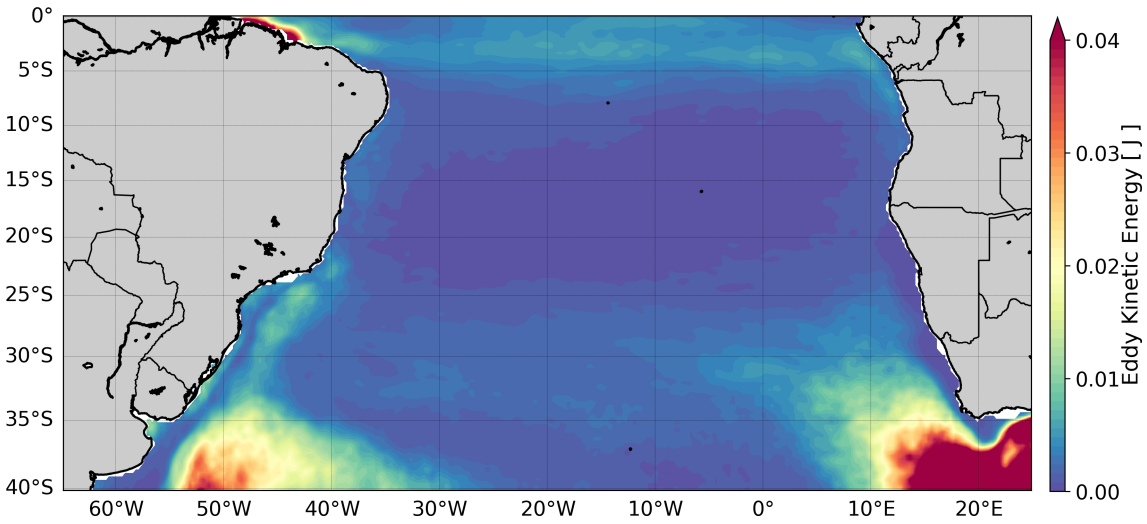

Figure 2.3: Spatial variance of the geostrophic velocity anomalies from AVISO's altimetric record in the South Atlantic as a proxy of the eddy kinetic energy.

2.3.3 The distinct dynamics in QG and SQG solutions

Figure 2.4 presents the Probability Density Functions (PDF) of the γ ratio (Equation 2.10) for each area, quantifying the representativity of ψ_{sqg}. The integral over the density function curve between the lowest and the greatest values of range represents the probability of the γ falling within a particular scenario, QG or SQG. This integral is always equal to 1, and can easily be transformed into percentages. In our case, the sum of the percentages is less than 100% because we are excluding $\gamma = 1$, meaning 50% contribution of each solution. The PDFs were normalized and limited on the x-axis ($\gamma = [0,2]$) after calculations to improve visualization.

At 11°S the western boundary region (WB blue patch, Figure 2.4) SSH variability is dominated by the interior solution. Being a western boundary current region, according to LeTraon *et al.* (2008) and Lapeyre (2009), one should expect SQG dominance over the upper dynamics. However, there are several factors that may have influenced this result. First, the WB region extends from 34.5°W to 30°W. It is known that the North Brazil Current (NBC) has a width of approximately 100 km and its flow is confined near the coast, which means that it was probably underestimated in our region. Moreover, the NBC at this latitude is a strong subsurface current, with its core around 150 m (SILVEIRA *et al.*, 1994), and we are specifically analyzing the surface signal (z = 0). Second, there is low kinetic energy attributed to the mesoscale, hardly reaching 0.01 J and this low energy pattern extends over the entire basin at this latitude. The remaining areas at this latitude are dominated by QG, exceeding 61% in all areas (blue patches, Figure 2.4). Given this

result, we also suggest that interior PV, related to ψ_{int} and the classical QG theory, has much more influence in the upper layer dynamics than horizontal density anomalies that drive the surface solution ψ_{sqg}. Therefore, we can conclude that at this latitude, SSH reconstruction using the SQG framework fails. According to Vergara *et al.* (2019), SSH spectral slopes in this latitude are, on average, close to k^{-2}, which is flatter than the predicted by SQG and QG theories. Although we cannot directly corroborate this result because we lack the information of our SSH spectral slopes, we found general agreement regarding low-energy areas and especially at the eastern boundary current systems, that receive more influence of unbalanced motions (RICHMAN *et al.*, 2012).

At 24.5°S it is noticeable an increase towards SQG dominance in all areas except the EB (purple patches, Figure 2.4) in comparison to 11°S. SQG gains importance at the western Atlantic (WB and WOF), but is still very weak close to the eastern boundaries. As shown by Aguedjou *et al.* (2019) and our Figure 2.3, eddy energy in this area is approximately twice as much as the same area at 11°S, which may have contributed to the rise in the percentage of SQG. However, EKE in this region in still considered small. In WB, both contributions are equally important (48%) and in WOF SQG dominates over QG (74%). The reason for this dominance, however, is not quite clear. It may be associated to the northern branch of the South Atlantic Current (SAC) that re-circulates to meet the BC again, or the inclusion of a small part of the BC inside the area. To better assess this result, further investigation regarding the conditions of baroclinic instabilities are needed, which is outside the scope of this study. We corroborate results from Rocha *et al.* (2013), since the MARLIM mooring (22.7°S; 40.2°W) analyzed in their study is contained in our WOF area: SQG can describe surface movements at this location. However, the authors also show that the SQG solution may be indistinguishable from a 3 mode interior QG reconstruction. As for the eastern boundary (EB purple patch, Figure 2.4), results are similar to those of the previous latitude.

Regarding altimeter spectral slopes, Richman *et al.* (2012) (Pacific ocean) and Vergara *et al.* (2019) (globally) noticed a decrease in k values towards SQG predictions with increasing latitude, especially between 20°S and 60°S, which may also suggest that at some point (i.e. latitude), there is a regime shift and SQG becomes dominant.

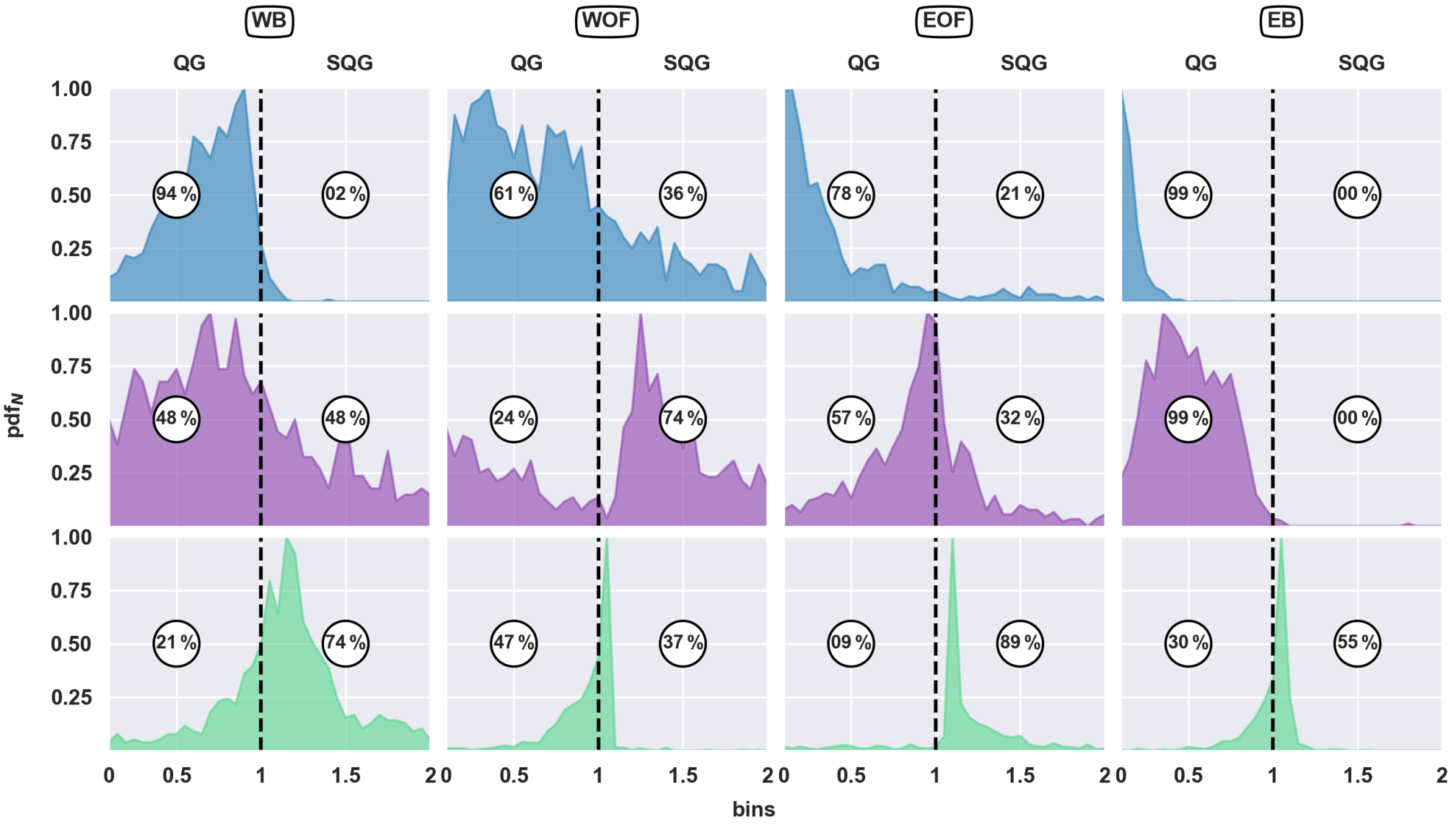

Figure 2.4: Normalized Probability Density Function (PDF_N) of γ at 11°S (blue), 24.5°S (purple) and 34.5°S (green). Percentages indicate how much of γ falls between QG ($\gamma < 1$) and SQG ($\gamma > 1$).

A completely different scenario arises at 34.5°S. SQG dominates in all areas, except for area WOF, which may be associated to the increase in EKE (Figure 2.3). This result also suggests that SQG importance grows polewards. A significantly increase in SQG dominance is noticeable when comparing regions at the former latitudes. As mentioned, our area at 34.5°S (green patches, Figure 2.2) is close to the Brazil-Malvinas Confluence to the west and the Agulhas Current and the Agulhas eddy corridor to the east, the most energetic regions of the South Atlantic (Figure 2.3), and these results corroborates previous studies (e.g.: LeTraon *et al.* (2008)) in terms of SQG dominance in high latitudes and high eddy kinetic energy areas. As for the WOF region, we suggest that the QG dominance may be associated to the Brazil Current Front and its baroclinic flow and a drop in EKE due to the eastward position of this area in relation to WB, which may explain why at this region QG dominated over SQG. It was pointed out by Rocha *et al.* (2016) that QG should be relevant near strong baroclinic currents, given the dominance of the stretching term in the quasi-geostrophic potential vorticity gradient, the non-uniform PV field and the propensity of baroclinic instability.

According to Rocha *et al.* (2016), during summer and for wavelengths smaller than 100 km, a shallow mixed layer (ML) associated with a strong pycnocline can trap and enhance the kinetic energy of surface unbalanced motions. When approaching winter, the deepening of the ML facilitates instabilities. The latter may favor small-scale $O(1–10)$ km frontal instabilities. Even though we do not resolve these scales, they may be important for the variability of SSH and EKE. Sasaki *et al.* (2014) showed for a high eddy energy region on the North Atlantic that there is an important seasonal cycle driven by the atmosphere and interactions between scales that affect the SSH variability. During summer, a shallower MLD imply in weak lateral buoyancy gradients, meaning weak available potential energy (CALLIES *et al.*, 2015). Moreover, the ML is not horizontally homogeneous, thus horizontal density gradients can modify its thickness and horizontal structures (TANDON; GARRETT, 1995). Therefore, we expect that our SQG reconstructions to be better during winter, when the MLD is deeper.

Indeed, results presented in Table 2.2 suggest that SSH reconstruction under SQG theory is better during winter, when the mixed layer depth (MLD) is deeper, corroborating Gonzalez-Haro and Isern-Fontanet (2014). Vergara *et al.* (2019) reported a regime change from summer to winter, the former being dominated by QG and the latter by SQG. This regime change is evident in WOF and EB at 34.5°S and in EOF 24.5°S (red values, Table 2.2). Although only evident in a few regions, all areas except from WB at 24.5°S had an

Table 2.2: Percentagens of the QG and SQG dominance in winter and summer for all regions at 11°S, 24.5°S and 34.5°S. Red colors represent regime shift from QG (summer) to SQG (winter).

	WB		**WOF**		**EOF**		**EB**		
	QG	SQG	QG	SQG	QG	SQG	QG	SQG	**Latitude**
Total	**94%**	**4%**	**61%**	**36%**	**78%**	**21%**	**99%**	**0%**	
Summer	91%	2%	72%	27%	100%	0%	100%	0%	**11°S**
Winter	92%	4%	49%	46%	69%	29%	100%	0%	
Total	**48%**	**48%**	**24%**	**74%**	**57%**	**32%**	**99%**	**0%**	
Summer	51%	47%	45%	54%	82%	12%	100%	0%	**24.5°S**
Winter	59%	37%	8%	91%	33%	51%	99%	1%	
Total	**21%**	**74%**	**47%**	**37%**	**9%**	**89%**	**30%**	**55%**	
Summer	14%	84%	91%	2%	19%	80%	60%	23%	**34.5°S**
Winter	7%	90%	4%	85%	0.4%	99%	27%	92%	

increase in SQG percentages during winter, even in areas where QG is dominant. These results strongly corroborate Gonzalez-Haro and Isern-Fontanet (2014), Liu *et al.* (2014) and Isern-Fontanet *et al.* (2014) on the dependence of field reconstruction and the MLD. This means that during winter there are more SSH reconstructions that fall within SQG dominance ($\gamma > 1$).

Generally, SSH variability is composed of a variety of processes on a wide range of scales. Thus, the dominance lies between SQG and QG theories (TCHILIBOU *et al.*, 2018), as they are constantly competing over SSH (PONTE; KLEIN, 2013). Our results are consistent with previous studies (LETRAON *et al.*, 2008; RICHMAN *et al.*, 2012; ROCHA *et al.*, 2013; ISERN-FONTANET *et al.*, 2014; GONZALEZ-HARO; ISERN-FONTANET, 2014) in terms of SQG dominance over high latitudes and higher EKE areas.

2.4 Summary and Conclusions

Our motivation resides in the ongoing discussion on whether the surface fields and its dynamics are better described by the QG or the SQG framework. Altimetric satellites can identify features down to approximately 60 km due to its spatial resolution. Since correlations with HYCOM were higher than 0.8, we decided to analyze the latter SSH fields to draw conclusions about whether SQG or QG theory dominates the surface dynamics at 11°S, 24.5°S and 34.5°S on the Atlantic Ocean. Provided HYCOM has a better spatial resolution (0.08°), we were able to reconstruct the SSH field using a bandpass Lanczos

filter to retain wavelengths between 12 and 400 km, and even if we cannot resolve neither relate the smaller wavelengths to what the altimeter is seeing, the results presented here may shed a light when assessing QG or SQG dominance from approximately 60 to 400 km in different regions of the South Atlantic other then analyzing the wavenumber spectrum alone.

Following LaCasce (2012) and Wang *et al.* (2010), we reconstructed ψ and SSH fields using SQG theory and the relation $\psi = \psi_{sqg} + \psi_{int}$, the latter being the interior streamfunction associated with the QG theory. We used the method described in Section 2.2, assuming that surface density and interior PV are correlated. We obtained the transfer function χ as in LaCasce (2012) and Isern-Fontanet *et al.* (2014), but for non-constant Brunt-Väisälä profiles for each area in Figure 2.2. Once we had all the vertical solutions for a finite set of k, the SSH fields were bandpass filtered and we assessed the dominance of QG or SQG through the analysis of γ (Equation 2.10) as SQG and interior solutions contributes to SSH variability (WANG *et al.*, 2013).

According to Liu *et al.* (2014), the performance of the reconstruction is affected by data resolution. Regarding altimeters and apart from temporal sampling, data at high frequency is difficult to measure due to noise contamination, which leads to the impossibility of detecting smaller scales. Significant power in small scale signals is observed in the 7 km along-track data; however, these signals do come mostly from noise. Our choice of using HYCOM reanalysis resides precisely on the fact that it assimilates satellite and *in situ* data, providing physically consistent dynamical fields (T, S, SSH). Being more realistic, our SQG reconstruction method and results would be more reliable to compare the SSH from HYCOM and the SSH reconstructed under the SQG theory.

Although QG theory dominated over most of our study area, we point out that different dynamical regions (e.g.: western boundary currents, subtropical gyres) presented contrasting results (Figure 2.4). Indeed, Vergara *et al.* (2019) found that mid-latitudes zonally averaged SSH spectral slopes would follow the SQG theory, which was merely a computational result when averaging the slope range between QG and SQG. Besides, they have also considered together dynamically contrasting regions in these calculations. In previous studies, SQG dominance was found in small regions at mid-latitudes, mostly near highly energetic western boundary current systems (XU; FU, 2012; VERGARA *et al.*, 2019). Despite using a different method and SSH from a numerical model, we corroborate their results, since SQG dominated at WOF at 24.5°S — partially corroborating Rocha *et al.* (2013) — and at all areas except WOF at 34.5°S, in general agreement to Xu

and Fu (2012) and Vergara *et al.* (2019).

In terms of seasonal variation, our results strongly corroborate Gonzalez-Haro and Isern-Fontanet (2014). Our SSH reconstruction using the SQG framework was improved during winter, when the ML is deeper. Therefore, the dependence on the seasonal variation of the MLD is evident, which is also in agreement to Isern-Fontanet *et al.* (2014) and Sasaki *et al.* (2014), although there are a variety of processes that influence not only the ML but also SSH fields. Moreover, we were able to identify the regime shift mentioned by Vergara *et al.* (2019) in three areas (EOF at 24.5°S and WOF and EB at 34.5°S), and all regions where there was some SQG contribution except from WB at 24.5°S showed an increase in SQG dominance from summer to winter. In areas where SQG strongly dominates (e.g. WB at 34.5°S, WOF at 24.5°S), this increase is even higher.

The results showed by Richman *et al.* (2012) and Vergara *et al.* (2019) suggest that at the intertropical band, neither QG nor SQG dominates upper dynamics since the SSH spectral slope is approximately k^{-2}. From our results (Figure 2.4), QG dominated over the entire latitude of 11°S, suggesting that most of the contribution of SSH variability is associated to the interior PV. We therefore suggest treating 11°S with the QG theory. However, further investigation is needed to assess this result, especially towards the analysis of SSH wavenumber and EKE spectra. These spectra should provide more information regarding the spectral slopes and if they are indeed close to either what the QG theory predicts (k^{-5}) or to flatter values (k^{-2}). Still according to the aforementioned studies, up to 40°S there is an increase in SQG dominance with increasing latitude, also noticed in our results.

From Figure 2.4 and Table 2.2, QG – SQG dominance changes when approaching higher energy areas and higher latitudes. At 11°S, SSH reconstruction is in disagreement to the SQG theory. At 24.5°S, a higher contribution of SQG appears where there is more EKE, and at 34.5°S SQG strongly dominates. In this sense, our results are in general agreement with previous studies (LETRAON *et al.*, 2008; LAPEYRE, 2009; ISERN-FONTANET *et al.*, 2014; RICHMAN *et al.*, 2012; VERGARA *et al.*, 2019). Thus, SQG theory should be invoked in specific regions on the South Atlantic, at least when assessing SSH variability in the mesoscale range in the upper layer.

To provide a more comprehensive comparison, SSH wavenumber and energy spectra should provide additional information on QG – SQG dominance. We are aware that changes in SSH are influenced by ocean-scale interactions, and since our main limitation in SSH reconstruction resides on spatial resolution, we are missing smaller wavelengths (< 30 km) and the processes associated with them. According to Ferrari and

Wunsch (2010), the ocean kinetic energy is dominated by geostrophic motions and its spatial structure is controlled over a large range of scales. Thus, a variety of processes are constantly competing over energy distribution. Therefore, isolating one or even some of these processes is a challenge. We also propose a deep investigation on the environmental conditions to decide whether SSH reconstruction using the SQG framework is good enough to be applied to satellite data; in other words, if the reconstructed SSH correlates well with altimeter's SSH, and in which conditions the reconstruction is better. We began working on that, showing the relationship between the SSH reconstruction and the MLD seasonal variation, as in Gonzalez-Haro and Isern-Fontanet (2014).

The surface streamfunction can be reconstructed using the surface buoyancy field provided we (i) assume that PV is constant (zero, for convenience) and (ii) allow buoyancy at the surface. Since the total streamfunction includes both the surface and interior solutions, this reconstruction can provide an insight of the different dynamical regimes that are present in the South Atlantic, and when to invoke one or another theory in the study of upper dynamics and SSH variability. In conclusion, we accept hypothesis H_1, since SSH reconstruction under the SQG framework varied within latitudes and its subsequent regions. The lowest latitude and areas with low EKE (Figures 2.3 and 2.4) are dominated by QG solutions, while higher EKE areas (e.g.: the meanders of the Brazil current at 24.5°S, Brazil-Malvinas Confluence and Agulhas leakage) are associated to SQG. The change in regime QG – SQG described by Vergara *et al.* (2019) was observed at 24.5°S (EOF) and 34.5°S (WOF and EB), and in all areas except for WB at 24.5°S SQG strongly dominated during winter.

The present results have implications that will be useful for the analysis of data collected by the upcoming Surface Water and Ocean Topography (SWOT) satellite mission, planning for launch in 2021. SWOT will resolve ocean scales from 30 km, depending on sea state, providing a more accurate and complete wavenumber spectra. With that, it would be possible to evaluate energy cascades and dissipation rates at smaller scales between the ocean surface and interior, accounting for balanced and unbalanced motions, high frequency internal tides and internal gravity waves (MORROW *et al.*, 2019). We point out that this information added to the field reconstruction under SQG theory will refine the knowledge of interior and surface dynamics at mid-latitudes. With the new SWOT mission, it will be possible to better understand the regional and seasonal variations of this dominance, especially regarding low energy areas, the relative contribution of PV stretching, the horizontal velocity gradients in the upper layer and vorticity balance,

in terms of quantifying unbalanced motions and their influence in the upper layers. Thus, this will reaffirm the role of altimetric satellites as the only ones that allow us to make inferences about the internal dynamics of the oceans. Our results using HYCOM corroborates previous studies and the possibility to extend our findings to a high-resolution altimeter is encouraging.

3 *Quasi-geostrophic interior modes and Rossby waves*

For quasi-geostrophic motions, the velocity field is geostrophic to the lowest order and the time evolution of the flow is determined by ageostrophic movements (KUNDU; COHEN, 2002). Assuming the β-plane approximation, in this Chapter we introduce Rossby waves, that owe their existence to the latitudinal variation of the Coriolis parameter f (the β effect), that provides a basic state PV gradient. First-mode baroclinic Rossby waves can be defined as large scale propagating features on the interface between two layers of different densities within a thin layer of fluid over a sphere. For the shallow-water regime, the baroclinic motion is a balance between the stretching vorticity caused by interface displacements and the planetary vorticity. The so-called β effect refers to the influence of Earth's rotation on the movement of a fluid considering Earth's curvature. Thus, it acts on the vorticity of a fluid that meridionally moves on the planetary vorticity field. This happens because the perpendicular planes to the Earth's rotation axis (i.e. latitudes) present maximum (minimum) tangential velocity in the Equator (Poles), due to the variation of the radius of the rotation plane.

Figure 3.1 shows a schematic of a long internal Rossby wave. Considering an upward displacement of the interface and an associated baroclinic flow, east of the hump the northward flow in the top layer demand H_1 to increase to conserve potential vorticity. In the same way, west of the hump, the southward flow requires a decrease in H_2, for the same reason. Thus, the interface must rise on the east and sink on the west, resulting in a westward movement. The conservation of PV acts as its restoring mechanism and their generation is strongly associated to variations in the PV field, which may be caused by a variety of physical processes such as variability of the wind stress curl (HERRMANN; KRAUSS, 1989; FU; QIU, 2002; WATANABE *et al.*, 2016), advection by zonal currents and baroclinic instabilities (COX, 1980; KILLWORTH; BLUNDELL, 2007). As previously mentioned, Rossby waves play an important role in ocean large scale circulation

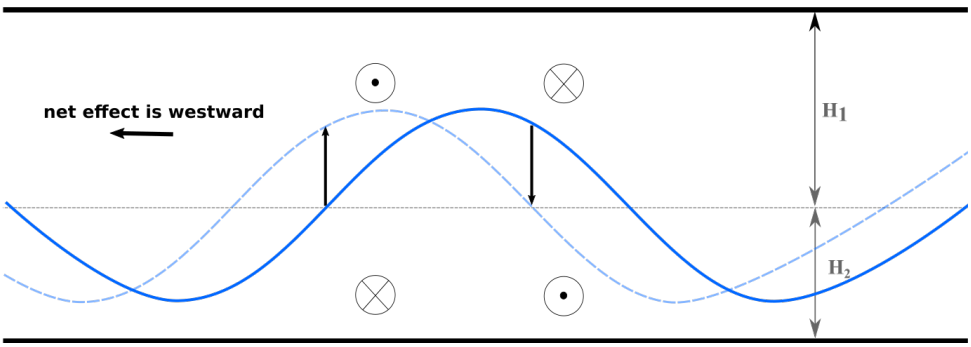

Figure 3.1: Schematics of a long internal Rossby wave. Adapted from Salmon (1998).

because they have a direct impact in intensifying western boundary currents. The phase speed range from 1 – 10 km day^{-1} and wavelengths from $O(10^2 \text{ - } 10^3)$ km (POLITO; CORNILLON, 1997), depending on the latitude.

These waves were extensively described in the literature and although found in the three ocean basins (CHELTON; SCHLAX, 1996; POLITO; LIU, 2003), most studies are focused on the Pacific ocean (KANG; MAGAARD, 1980; KESSLER, 1990; FU; QIU, 2002; MAHARAJ *et al.*, 2007; BELONENKO *et al.*, 2017). They are known to be faster in low latitudes (GILL, 1982, Figure 12.3), since its phase speed depends on the Coriolis parameter. Additionally, these waves have a very clear signal in sea surface height fields when displacing the main thermocline (POLITO; CORNILLON, 1997), making them identifiable in altimeter data, especially in Hovmöller (also known as zonal-temporal) diagrams.

Using a method based in several filters and contrasting the idea of Chelton and Schlax (1996) who claimed that the phase speed of Rossby waves in mid to high latitudes are faster than the linear theory predicts, Polito and Liu (2003) have decomposed the sea surface height data obtained by the Topex/Poseidon over 8 years into westward propagating features and characterized its parameters (e.g.: λ, T, c_p and A) globally. Details on the method, which was very similar to the one applied in this study, will be discussed later. Their results corroborated previous studies (BOULANGER; MENKES, 1995; ZANG; WUNSCH, 1999) and provided a global coverage on the characteristics of Rossby waves. As noted by Polito and Liu (2003), the phase speed of the Rossby waves detected using the altimeter data suggested that these waves are of the first baroclinic mode, meaning that the surface is reflecting movements at the thermocline. Interestingly, there are remarkable differences within waves' amplitudes at the surface among the three major ocean basins (POLITO; LIU, 2003, Figures 3, 4 and 5, upper right panel), being significantly lower in the Atlantic ocean when compared to Pacific and Indian basins, especially in the 10°S –

30°S latitude range.

The reason for this difference in amplitudes is not obvious, and is the main motivation for this Chapter. Some possible explanations are directly related to waves' forcing mechanisms. Apart from the Equator, ocean circulation is driven by Ekman transport due to the spatial variability of the wind stress curl. A series of zonal bands, alternating convergences and divergences arise and drive the interior circulation (TALLEY *et al.*, 2011) by the emergence of vertical movement (w). As noted in a variety of studies (HAN; LEE, 1985; MILLIFF; MORZEL, 2001; RISIEN; CHELTON, 2008; LEE *et al.*, 2013; SUDRE *et al.*, 2013) the large-scale variability on a scale of months to years of the wind stress and wind stress curl in mid-latitudes at the three ocean basins is similar. Another possible explanation is due to changes in stratification. Recalling Section 1.2, the linearized form of the potential vorticity conservation equation, for a baroclinic ocean, is

$$\frac{\partial}{\partial t}\left[\nabla^2\psi - \frac{\partial}{\partial z}\left(\frac{f_0^2}{N^2}\frac{\partial \psi}{\partial z}\right)\right] + \beta\frac{\partial \psi}{\partial x} = 0\,, \tag{3.1}$$

where N is the Brunt-Väisälä frequency (Equation 1.9). Thus, vertical variations of N^2 profiles imply in changes in the stretching vorticity term of equation (3.1). Therefore, stratification plays an important role in interior dynamics. Providing the similarity in wind forcing, in this Chapter we propose that the discrepancies in waves' amplitudes may be associated to the density stratification.

According to McWilliams (2006), it is a common practice to decompose fields of a baroclinic fluid in vertical modes in a way that each variable is written as a sum over the vertical modal contributions. This method is useful when most of the energy is attributed to few vertical modes, which happens in large-scale ocean dynamics. Kundu *et al.* (1975) conducted one of the pioneer studies regarding this modal decomposition, investigating fluctuations in ocean currents near the Oregon cost. The authors separated the velocity field into a depth-invariant – i.e. barotropic – and several baroclinic components. The barotropic mode had a positive and high correlation (0.8) with sea surface height, meaning that southward currents were associated to lowering the sea level, consistent with a geostrophic alongshore current. Also, the barotropic mode had the highest explained variance, followed by the first baroclinic mode. In the same study of Kundu *et al.* (1975), one remarkable result was that the first baroclinic mode was negatively correlated to the wind stress curl, meaning that the surface variability is mostly northward when the wind is southward, but positively correlated to sea surface height. The authors suggested that the results are mainly tentative, since they are based in measurements from a single section,

and the behavior of the baroclinic component was not readily explained. Although dealing with coastal currents, these results show a significant progress to assess the contribution of the decomposition in normal modes.

Several years later, Silveira and Brown (2000) studied the dynamics of the North Brazil Current retroflection between 1990 and 1991 to investigate the dynamics of its meanders. The authors have decomposed the velocity observations into dynamical modes in the same way as Kundu *et al.* (1975) and LeBlond and Mysak (1978). In the study of Silveira and Brown (2000), centered at 5°N, the sum of the first three vertical modes accounted for 75% of the vertical structure of the flow, and a six-mode approximation represented well the velocity profiles. Moreover, the barotropic plus the first two baroclinic modes are sufficient to characterize and represent wave dynamics (DEWAR; MORRIS, 2000), which was also corroborated by Maharaj *et al.* (2007). According to Maharaj *et al.* (2007), the variance attributed to Rossby waves in sea surface height data is associated to the first three modes. Motivated by the aforementioned studies, we tested to see how many modes were representative of the surface field seen by the altimeter (See Appendix B), and reconstructed the sea level anomaly accounting for the barotropic plus the first and second baroclinic modes.

The solution of the vertical modes depends only on the local stratification, i.e. the $N^2(z)$ profile (See Section 2.2 equations (2.4) and (2.5) and Appendix A.1). The barotropic mode ($i = 0$) is constant over depth, taken as a unity for convenience, so that its vertical gradient ($\partial F_0/\partial z$) is zero. Unlike the barotropic, the baroclinic modes ($i > 0$) have i zero crossings in depth, meaning that larger modes correspond to smaller R_{di}. Moreover, their vertical structure varies with depth ($\partial F_i/\partial z \neq 0$), so that disturbances caused by a baroclinic Rossby wave are expected to be associated to density variations. Therefore, one can establish a direct relation between the first baroclinic Rossby wave signals captured by the altimeter and the first baroclinic mode.

In this Chapter we characterize Rossby waves at 11°S, 24.5°S and 34.5°S at the Southern Hemisphere and attempt to address the differences on the waves' amplitudes through the analysis of the stratification. The first discussion concerns the identification of long, first mode baroclinic Rossby waves in sea level anomaly and the similarity on atmospheric forcing along the latitudes of interest. If the forcing is almost the same, why can we see discrepancies in waves amplitudes? Then, we look at this question thinking about stratification and the first baroclinic structure. We address this issue by considering depth-variant N^2 profiles and the aforementioned modal decomposition.

3.1 Data and methods

In Section 2.1, we showed the correlation (0.8, p-value = 0) between sea surface height fields derived from altimetry and from HYCOM outputs at 15°N on the Pacific ocean (Figure 2.1). Because of the satellite data assimilation and the use of satellite products to validate the model (CUMMINGS, 2007; BACKEBERG *et al.*, 2009; SUDHEER; RAVICHANDRAN, 2012; CASTELLANOS *et al.*, 2016), we expect HYCOM to correctly identify Rossby waves signals for the same time interval since it provides physically consistent fields. We chose to conduct a test case at 15°N on the Pacific because of the following reasons:

1. The Pacific has the largest basin of all oceans, so that boundary effects should be relatively less relevant;
2. The Coriolis effect is significant, since we are away from the Equator, and the R_{di} estimation for the first baroclinic mode is compatible with altimeter's resolution;
3. Polito and Liu (2003) showed that annual and semi-annual baroclinic Rossby waves present amplitudes similar to those of the seasonal cycle;
4. This tropical region is influenced by El Niño/La Niña, so that this signal is included in SSH observations.

From Figure 2.1 it is readily noticed that HYCOM includes all the altimetric signals, despite the different dynamics associated to them. Thus, for the meso to large scale, the signals are maintained and the sea level anomaly is well represented by HYCOM. In this Chapter, we also compared T and S from HYCOM with a reanalysis based exclusively on *in situ* measurements data. The idea was to examine variability between the outputs and consequently the results when calculating the vertical modes, and assess if the Rossby waves detected in HYCOM outputs are consistent to the ones detected on the altimeter sea level anomaly data. The test case and the method employed can be seen in Appendix B.

3.1.1 Data

Apart from the HYCOM outputs and sea surface height from the altimeter already mentioned in the previous Chapter, in this Section we introduce the *In Situ Analysis System* (ISAS) dataset, which are entirely based on *in situ* measurements. T and S profiles

from ISAS are distributed by the *Coriolis Data Center* and are obtained from Argo floats, moorings and scientific cruises, having a spatial resolution of 0.5°. The data are "based on the optimal interpolation and the estimated quantity is the anomaly on depth levels relative to a reference climatology and is uni-variant, which means that temperature and salinity are estimated independently" (GAILLARD, 2012). Both variables have 150 vertical levels, ranging from 0 to 2000 m. The ISAS data is developed and maintained in the *Laboratoire de Physique des Océans*, within Argo Observing Service (SO-ARGO) where they are used for research on meso to large scale processes that demand relatively high vertical resolution.

The autonomous profilers which the data from ISAS is mainly based spend most of their time drifting in depth, where they stay neutrally buoyant. At typical 10-day intervals, the floats pump fluids into a bladder and the profiler rise to the surface for about 6 hours while measuring temperature and salinity. While at the surface, floats transmit the collected data to satellites and the latter measure their geographical position. In sequence, the bladder is emptied and the profiler returns to its original density, sinks and drifts until the next cycle. Argo profilers are designed to produce about 150 of these cycles, and usually collect variables above 2000 m. Temperature accuracy is ± 0.002°C and pressure is ± 2.4 dbar. Salinity, on the other hand, can have two accuracy values: the first one, ± 0.01 psu when data is uncorrected and the sensor drift is small; and the second, after the drift corrections and thermal lag error, found in the dataset itself. Deposition of Argo profilers began around the 2000s and continues at a rate of 800 each year. They are distributed around the globe approximately every 3 degrees ($\sim$300 km) and are the primary source of global subsurface datasets used in most oceanographic data assimilation and reanalysis models. In this context, ISAS is an analysis tool for the T and S fields, originally designed for Argo data synthesis. From the 2000s, with a higher rate of profilers in the ocean, it extended to the global ocean.

A comparison between the climatology from ISAS and HYCOM outputs was made in terms of $N^2(z)$ and vertical modes. Because ISAS fields are based on statistics, i.e. local scale of autocorrelation, we intended to assess if ISAS can preserve the information in the scales of interest and be used to calculate the vertical modes. Both HYCOM and ISAS assimilate Argo data, so the data are far from being statistically independent; therefore, a high correlation was already expected. The data treatment was the same for the two outputs: T and S were converted in conservative temperature and absolute salinity to retrieve density and potential density profiles. We calculated $N^2(z)$ and the vertical struc-

ture of the baroclinic modes (F_i) and correlations were higher than 0.98 (p-value = 0). Thus, there were no significant differences between T and S from both reanalysis outputs.

3.1.2 Finite Impulsive Response filters

As in the studies of Polito and Cornillon (1997), Polito *et al.* (2000) and Polito and Liu (2003), the Finite Impulse Response filter (FIR2D) is applied to the altimeter sea level anomaly (hereafter η) data to decompose the signal in propagating and non-propagating features. This method consists of a chain of convolution filters, such that the data to be filtered $\eta_u(x,t)$ is convolved with a filter kernel $f_i(x',t')$, resulting in η_f. Both are 2D, with longitude and time (x,t) and their respective lags (x',t') as independent variables; this guarantees that the filter can select eastward or westward directions. The repeated (chained) operation is $\eta_f(x,t) = \eta_u(x,t) \otimes f_i(x',t')$, such that in the next iteration the data to be filtered does not have the signal already filtered, i.e. $\eta_u(x,t) \longleftarrow (\eta_u(x,t) - \eta_f(x,t))$.

A key concept is that we already have some information about the signals we want to filter. For example, in most latitudes there is an obvious annual signal due mostly to the short wave contribution to the heat budget, and its periodicity is determined from the seasonal cycle: one solar year. The duration of the day and solar declination are independent of longitude, thus a natural length scale is the basin width along a given parallel. With this information we can build a filter kernel with one central bump, half year between zero-crossings, and half of the basin width. To avoid spectral leakage, tapering at the borders is necessary. One can achieve this using a wide Gaussian bump. In the case of long Rossby waves, linear theory provides a reference westward phase speed if we assume (i) no forcing, (ii) no mean flow and (iii) flat bottom. The idea of filtering is similar: for each period, derived from harmonics and sub-harmonics of a solar year, we build the filter kernel with one central bump and taper the borders with a Gaussian function. This Gaussian is multiplied by a cosine surface dependent on (x,t), allowing positive (crests) and negative (troughs) values. Moreover, the size of the kernel filter is empirically chosen, half wavelength and half period for the non-propagating signal, and one wavelength and one period for waves. This scales result in a minimum overlap between spectral bands, ensuring a more continuous spectrum (for details see Polito *et al.* (2000) and Polito and Liu (2003)).

The kernel filters are applied in a decreasing order. The larger the component, the larger the number of points of $f_i(x',t')$ (LIM, 1990). First, we remove low-frequency

signals, beginning with the seasonal cycle. In this case, the normalized Gaussian-function have its maximum (minimum) at the center (corners), so that the sum of all points equals one. Subsequently, we filter Rossby waves with fixed periods (T) of 731 (η_{24}), 365 (η_{12}), 183 (η_6), 91 (η_3) and 46 (η_1) days. From an initial guess of c_p, in agreement to the linear theory, λ is estimated from $c_p = \frac{\lambda}{T}$. In this case, the Gaussian-function (G) is multiplied by the tapered cosine function, that is,

$$f_i(x',t') = G \cdot \cos\left(\frac{2\pi}{L}h - \frac{2\pi}{V}v\right), \tag{3.2}$$

where L and V are the horizontal (related to x) and vertical (related to t) wavelength and (h,v) the 2D field to set the size of the filter. After all the waves are removed, we separate the large-scale non-wavelike signal and the "mesoscale eddy field" (η_E) (POLITO; LIU, 2003), using a similar approach to that of the seasonal cycle component. Thus, the η_0 is decomposed into the following:

$$\eta_0 = \eta_t + \eta_{24} + \eta_{12} + \eta_6 + \eta_3 + \eta_1 + \eta_E + \eta_r\,, \tag{3.3}$$

where η_r represents the residuals, i.e. what is left from η_0 after the filtering process, which also includes the barotropic and low-frequency signals and η_t includes both the seasonal and the large-scale (tendency included), non-wavelike signal. In all components, we ensure that the filtered matrix explains the most variance of the original by least-squares fitting it to the unfiltered field.

The Hovmöller diagram of the component to be filtered is subdivided in tiles of size $\lambda \times T$. For each tile, we calculate the autocorrelation matrix and subsequently the Radon transform (LIM, 1990). The estimate of c_p is given by the tangent of the angle corresponding to the highest variability (POLITO; CORNILLON, 1997; CIPOLLINI *et al.*, 1998). As c_p is the most accurate, λ is corrected. The parameters are averaged in space and time so that there is only one value of c_p, T and λ for the entire area. Then, the process is repeated using this new c_p until the average difference between the last calculated c_p and the present value has converged within 10% of the latter or more than 20 iterations have been done (POLITO *et al.*, 2000). These parameters, as well as the wave amplitudes (A), are estimated based on a least-square fit of a sinusoidal function of the filtered matrix relative to η_u before filtering.

The main advantage of using 2D filters instead of 1D resides in the sensitiveness to propagation. Having a 2D and 1D filter of the same length, each output data point in the first case will be calculated based in a larger number of input data points, resulting in

a better performance. Moreover, 1D filters give independent phase estimates at times t and $t+1$, which means they could introduce phase breaks due to mesoscale instabilities (POLITO; CORNILLON, 1997). Since 2D filters operate simultaneously in space and time, the resulting phase is relatively more continuous.

3.1.3 QG modal decomposition

The modal decomposition applied in this Chapter was explained in Section 2.2 and detailed in Appendix A.1. In this Section, we are looking exclusively to the traditional QG vertical decomposition (Equations 2.4 – 2.5). In other words, $q \neq 0$ (Equation 2.1) and there are no lateral variations in surface buoyancy, i.e. $b_s = 0$. To calculate the vertical modes, we used T and S profiles from ISAS, vertically interpolated to have 10 m spacing.

Following LeBlond and Mysak (1978) and Silveira and Brown (2000), the meridional velocity can be separated into its vertical and horizontal structures:

$$v(x,y,z,t) = \mathbb{V}_i(x,y,t)\, F_i(z)\,, \tag{3.4}$$

where $\mathbb{V}_i$ is the meridional velocity modal amplitude for each mode and F_i is the vertical structure calculated as in Section 2.2 and equation (2.4), analogously for the zonal velocity u. To obtain the modal amplitudes,

$$\mathbb{V}_i(x,y,t) = \frac{1}{H}\int_{-H}^{0} v(x,y,z,t) F_i(z) dz\,, \tag{3.5}$$

and for the first three modes,

$$[u,v] = \sum_{i=0}^{2} [\mathbb{U}_i, \mathbb{V}_i]\, F_i\,. \tag{3.6}$$

According to Flierl (1978) and Silveira and Brown (2000), the relationship between the velocities' modal amplitudes $\mathbb{U}_i$ and $\mathbb{V}_i$ and the streamfunction modal amplitude Ψ_i assuming $\psi(x,y,z,t) = \Psi_i(x,y,t)\, F_i(z)$ is:

$$[\mathbb{U}_i, \mathbb{V}_i] = \left[-\frac{\partial}{\partial y}, \frac{\partial}{\partial x} \right] \Psi_i\,. \tag{3.7}$$

Thus, having the amplitudes Ψ_i, one can reconstruct the streamfunction ψ_i for each mode at several vertical levels. Following Thompson *et al.* (2002), η can be approximated by

truncating the first three modes:

$$\eta = \frac{f_0}{g}\psi(z=0) = \frac{f_0}{g}\sum_{i=0}^{2}\Psi_i F_i(z=0)\,, \tag{3.8}$$

and each mode gives different temporal and spatial patterns that, when added, yield the total η field.

Since the altimeter only provides a single, integrated value for the dynamic height, the modal amplitudes were estimated using HYCOM's u and v vertical profiles. According to Dewar and Morris (2000), a model based in the barotropic and first two baroclinic modes is sufficient to reproduce long baroclinic planetary waves. Their results suggest that at least three layers are necessary to capture the dynamics by ocean adjustment. In the South Pacific, Maharaj *et al.* (2007) showed that the fourth baroclinic mode is negligible in the sea level anomaly signal from altimetry, being the first two together with the barotropic mode responsible for almost all the variance. We corroborate their results, in our test case scenario (See Appendix B) in that the three first modes accounted for more than 76% of the vertical structure. Therefore, the modal amplitudes $\mathbb{U}_i$ and $\mathbb{V}_i$ were calculated using these modes only. Our assumption is that η captures the barotropic and the first and second baroclinic modes.

We calculated the modal amplitudes Ψ_i (Equations 3.5 and 3.7) using velocities from HYCOM and the vertical modes F_i (Equation 2.4) using N^2 from T and S profiles from ISAS. From equation (3.8), we reconstructed the η field and assessed the role played by stratification in waves' amplitudes under two different approaches. In the first one, we aimed to reconstruct the sea level anomaly from the Atlantic Ocean, using (i) Atlantic's stratification and (ii) different N^2 profiles, to obtain different vertical structures (i.e. F). For the latter, we used realistic and physically consistent N^2 profiles, from the Pacific and Indian basins. In the second approach, we reconstruct η for the three ocean basins in the Southern Hemisphere using each basin's N^2, F and Ψ, to identify differences among basins. Then, we compare the results in terms of Rossby waves' amplitudes applying the same filtering method.

3.2 Rossby waves in the Southern Hemisphere

The sea level anomaly η was decomposed in propagating and non-propagating features using the methodology described in Section 3.1.2 and results can be seen in Figures

3.2, 3.3 and 3.4 for the Atlantic, 3.5, 3.6 and 3.7 for the Pacific and 3.8, 3.9 and 3.10 for the Indian oceans. As previously mentioned, η_0 stands for the original sea level anomaly data, η_t the large-scale basin signal, η_j, j = 24, 12, 6, 3, 1, the propagating signals and η_r the residual. Our results derived from a time series of 26 years and a combination of a variety of altimetric satellites (e.g.: Topex/Poseidon, Jason-1, Jason-2, ESR-1, ESR-2), which leads to improved interpolation methods and smaller associated errors.

The η_t is presented in all latitudes as horizontal straight lines, meaning that the whole basin goes up or down at the same time once a year in a non-propagating seasonal cycle. It is possible to observe some interesting phenomena in these diagrams: a tendency in sea level rise that could be due to continental ice melting and thermal expansion (CHURCH *et al.*, 2004; CAZENAVE; LLOVEL, 2010) — a strong indication of global warming — and the seasonal cycle oscillating at the entire basin at all latitudes. At 11°S on the Pacific (Figure 3.5) it is also possible to notice the El Niño/La Niña east-west oscillation, also observed by Polito and Sato (2015) at 15°S. Nevertheless, this discussion is outside the scope of the present work and further investigation is needed to assess this result.

At all latitudes, the striking resemblance of η_0 and the sum of filtered data (η_s) means that the filter has a good performance. Indeed, the explained variance of η_s in relation to η_0, that is,

$$EV = 100 \times \left(1 - \frac{\sigma^2(\eta_0 - \eta_s)}{\sigma^2(\eta_0)} \right), \tag{3.9}$$

and σ^2 is the variance of the field, exceeds 86% in all cases, and the highest percentages were at 11°S for the Pacific and Indian oceans (99%). This also means that the filtering process does not modify in any significant amount the original data and are justified to proceed with the separation of the Rossby waves' signal. To determine how significant those percentages are, we performed a Monte Carlo statistical simulation. The η_0 was replaced by random noise, normally distributed, with the same mean and standard deviation as the original data and the FIR2D was applied in the same way. The explained variance results for all latitudes and components (not shown) fell between 0 and 1%, which suggest by contrast, that the filter is actually portraying a statistically significant signal from η_0.

Meinen *et al.* (2017) calculated the volume transport of the Deep Western Boundary Current (DWBC) at 34.5°S; their spectral analysis of the absolute transport time series peaked at 90 to 160 days, centered at 145 days. The authors suggested that this energy may be associated with mesoscale eddies (GARZOLI; SIMIONATO, 1990; MEINEN *et al.*, 2013, 2017), agreeing with what was claimed by Chelton *et al.* (2007), that these

westward propagating features are more likely nonlinear "coherent vortices" than Rossby waves. However, mesoscale eddies exhibit different dynamics and besides having a closed circulation, they are generally isolated and intermittent features. The translation speed of the eddies is of the same order of magnitude as c_p, which makes its signature in zonal-temporal diagrams similar to waves. At this latitude, however, the critical period of 3 – 6 months (POLITO; LIU, 2003) permits Rossby waves as solution to west-propagating features, e.g. Meinen *et al.* (2017).

The South Atlantic region between about 25.5°S and 35.5°S is known as the Agulhas eddies propagation corridor (GARZOLI; GORDON, 1996), and the generated eddies propagate to the west-northwest direction. During 1993 – 2016, Guerra *et al.* (2018) used a merged multi-mission altimeter data to detect and track the Agulhas eddies. The authors estimated a production of 6 ± 1.2 eddies per year and characteristics (amplitude, vorticity, volume, and energy), as well as the number of eddies, decay faster with longitude. In addition, they showed a significant overlap of the translation speed of the tracked eddies and the propagation speed of first mode baroclinic Rossby waves, which was shown previously by Oliveira and Polito (2013) between 10°S and 30°S. Using the same time series, Chen and Han (2019) identified short lived ($\sim$ 1 month) and long lived ($\geq$ 1 year) eddies using a combination of altimeter data. Their results for the South Atlantic show that the most frequent area of long lived eddy formation is along the east coast of Africa, probably due to the meandering of eastern boundary currents or to the influence of the waves generated by baroclinic instability. For the medium-lived, i.e. lifespans between 30 and 365 days, their origin and terminations are concentrated in the latitudinal range of 30°S and 60°S. Although some studies identify and treat phenomena found at latitudes south of 25.5°S as mesoscale eddies (CHELTON *et al.*, 2007; BAKER-YEBOAH *et al.*, 2010), there is evidence that these eddies are superimposed on Rossby waves in this region (OLIVEIRA; POLITO, 2013; POLITO; SATO, 2015).

Polito and Sato (2015) showed that there is a significant number of eddies that propagate along with Rossby waves, and this occurrence is neither random nor an artifact of the method employed. In their global analysis between 67.375°N and 67.375°S, the authors demonstrated that the method based on filters — similar to the one used in this study — correctly identified Rossby waves apart from eddies, and most of the eddies that are found over planetary wave extremum, stays there often (42% to 61%) for their entire lifetime. Moreover, 11% to 35% of the eddies detected were always superimposed in a wave maximum. The identified features in the filtering process are more elongated in the

Table 3.1: Explained variance (EV) of the sum of all filtered Rossby waves and the seasonal and large scale signal (η_t) for each latitude and basin of the Southern Hemisphere.

Basin	Latitude	Rossby waves	η_t
Atlantic	11°S	41%	56%
	24.5°S	57%	42%
	34.5°S	61%	32%
Pacific	11°S	63%	46%
	24.5°S	73%	22%
	34.5°S	51%	45%
Indian	11°S	69%	30%
	24.5°S	75%	19%
	34.5°S	67%	14%

meridional rather than the zonal direction, and since the height anomaly caused by an eddy has circular symmetry, it cannot be mistaken by a Rossby wave. This is particularly easy to see in their η_6 diagrams results, although many other components were analyzed. We also corroborate these structures in our diagrams (Figures 3.2 to 3.10). Thus, these eddies show a tendency to align their centroids to Rossby waves, but still can be separated by the filter.

From our results (Table 3.1), the sum of all filtered components identified as Rossby waves in the Atlantic explains the least amount of the original variance at both 11°S and 24.5°S, 41% and 57%. However, at the same latitudes, the contribution of the same waves to η_0 is at least 16% higher for the Pacific and 18% for the Indian oceans. At 34.5°S, the Rossby wave contribution increases for the Atlantic, reaching 61%, but decreases in the Pacific, 51%, and Indian, 67%, Oceans. Nevertheless, except for the Atlantic at 11°S, Rossby waves account for more than half of the surface signal. In the same way, the seasonal cycle and the large scale signal (η_t) contribution decreases with latitude on both the Atlantic and Indian oceans; as for the Pacific, it accounts for nearly half of the variability at 11°S and 34.5°S, being significantly smaller (22%) at 24.5°S. This means that the Rossby wave contribution to the sea surface height anomaly data is as high and as important as the seasonal cycle itself. It is interesting to notice that in most of the cases the explained variance of η_t to the sea surface height anomaly signal is smaller than the sum of the filtered Rossby waves, 11°S on the Atlantic being the only exception. Therefore, we accept hypothesis H_2, since most of the variability associated to propagating signals is explained by Rossby waves.

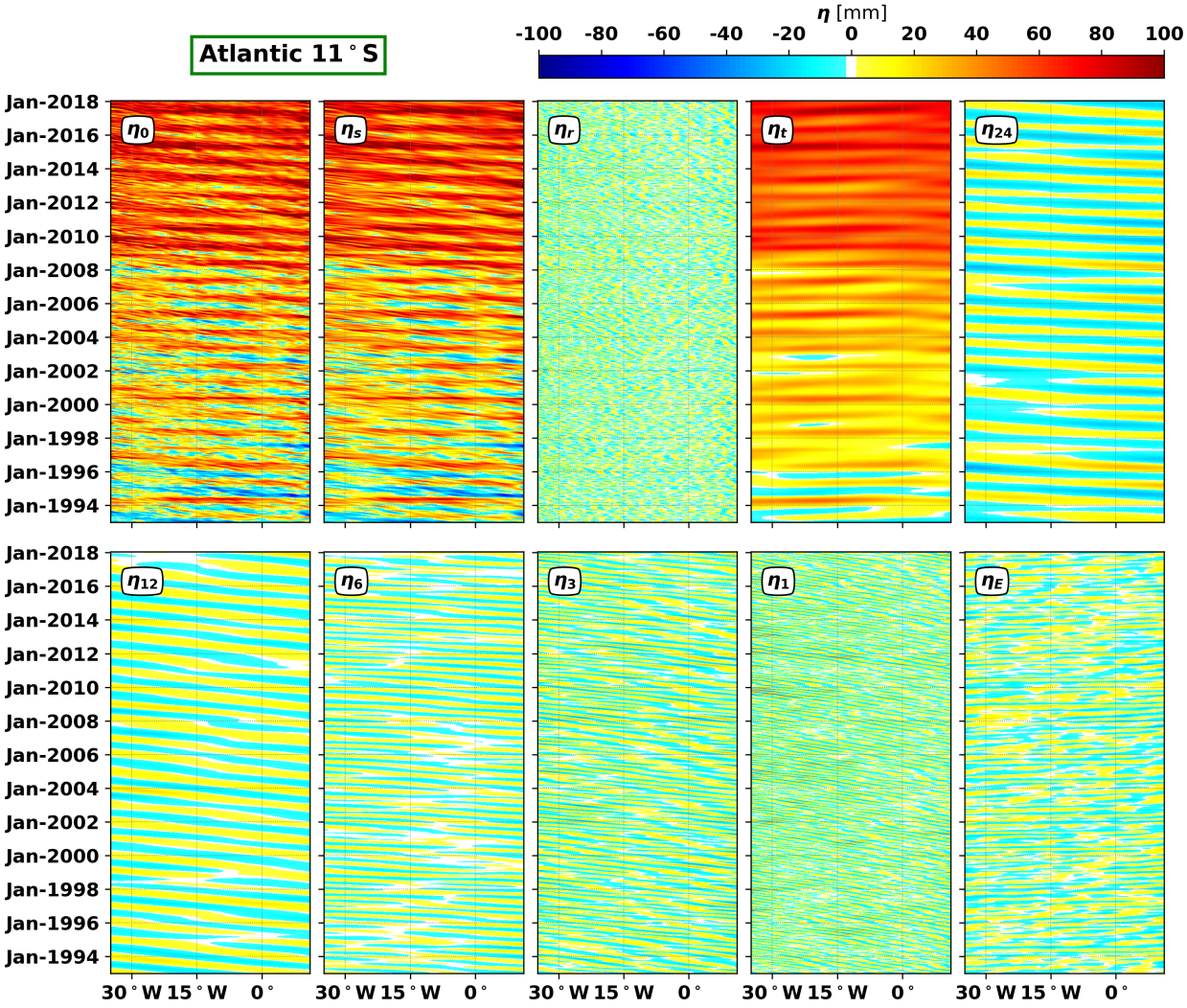

Figure 3.2: Propagating (η_j, $j = 24, 12, 6, 3, 1$) and non-propagating (η_t, η_E) components filtered from the altimeter's sea surface height anomaly from the Atlantic ocean at 11°S. η_0 stands for the original η, η_s for the sum of filtered components and η_r for the residual.

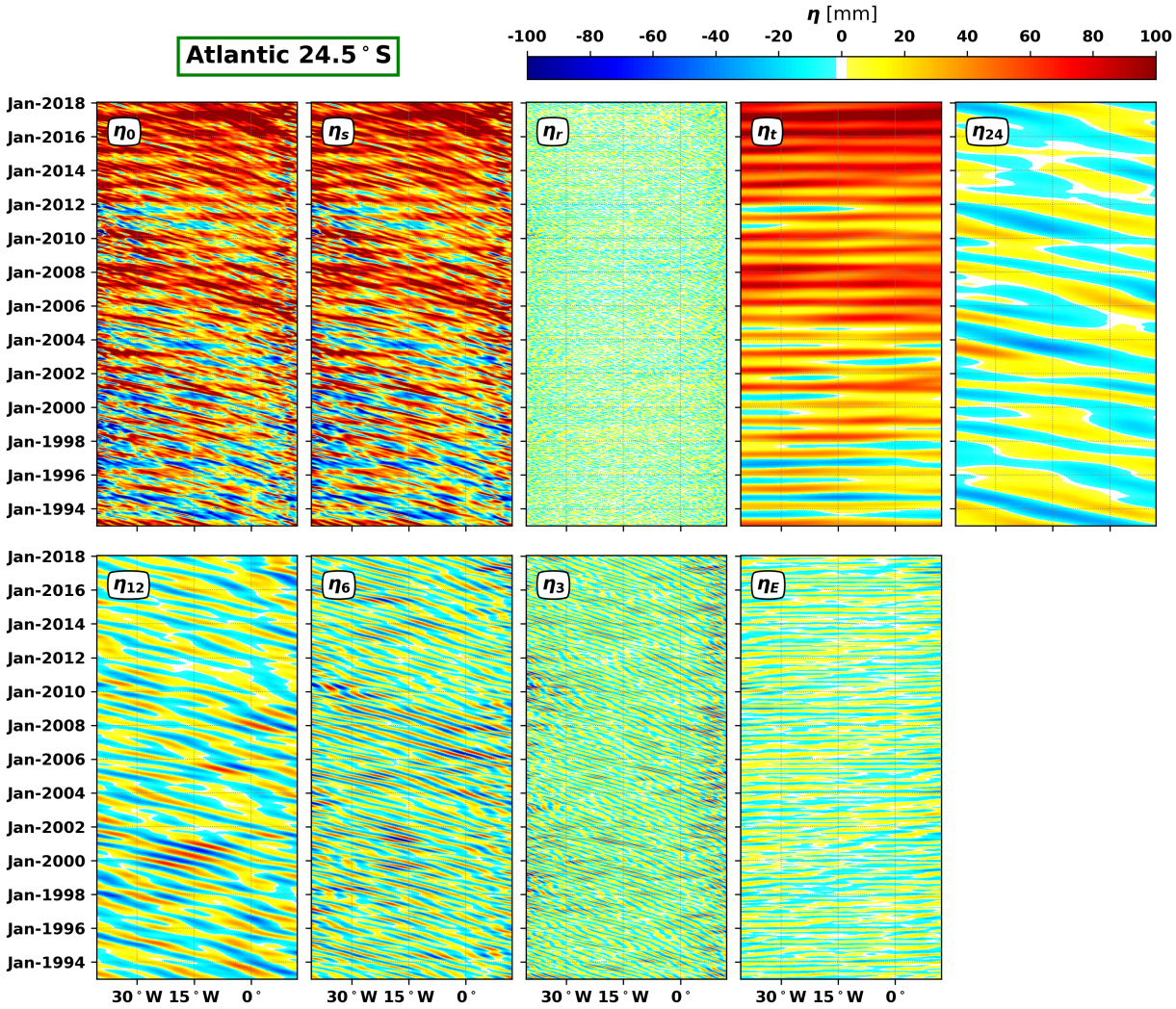

Figure 3.3: Similar to Figure 3.2 at 24.5°S.

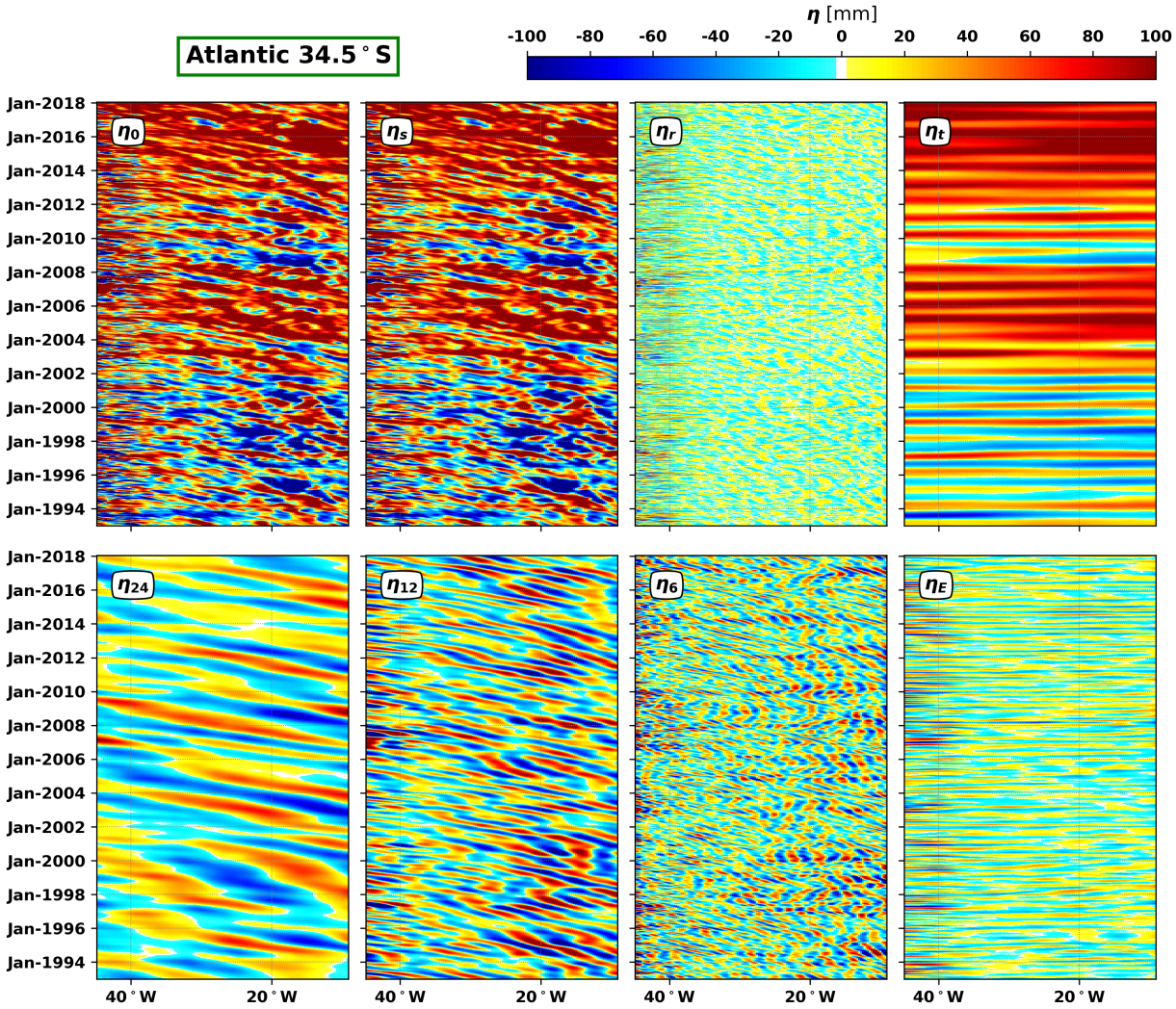

Figure 3.4: Similar to Figure 3.2 at 34.5°S.

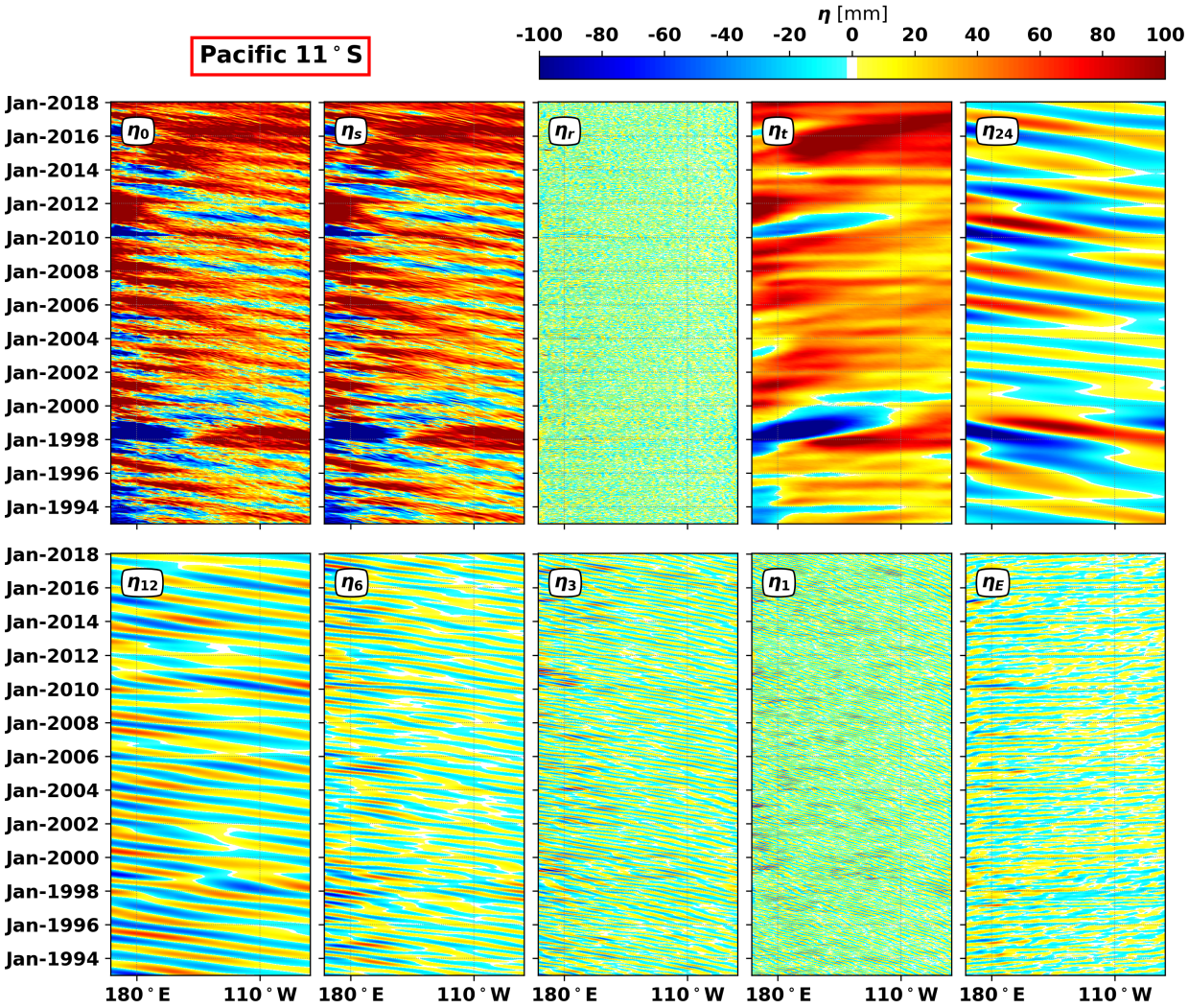

Figure 3.5: Similar to Figure 3.2 for the Pacific ocean at 11°S.

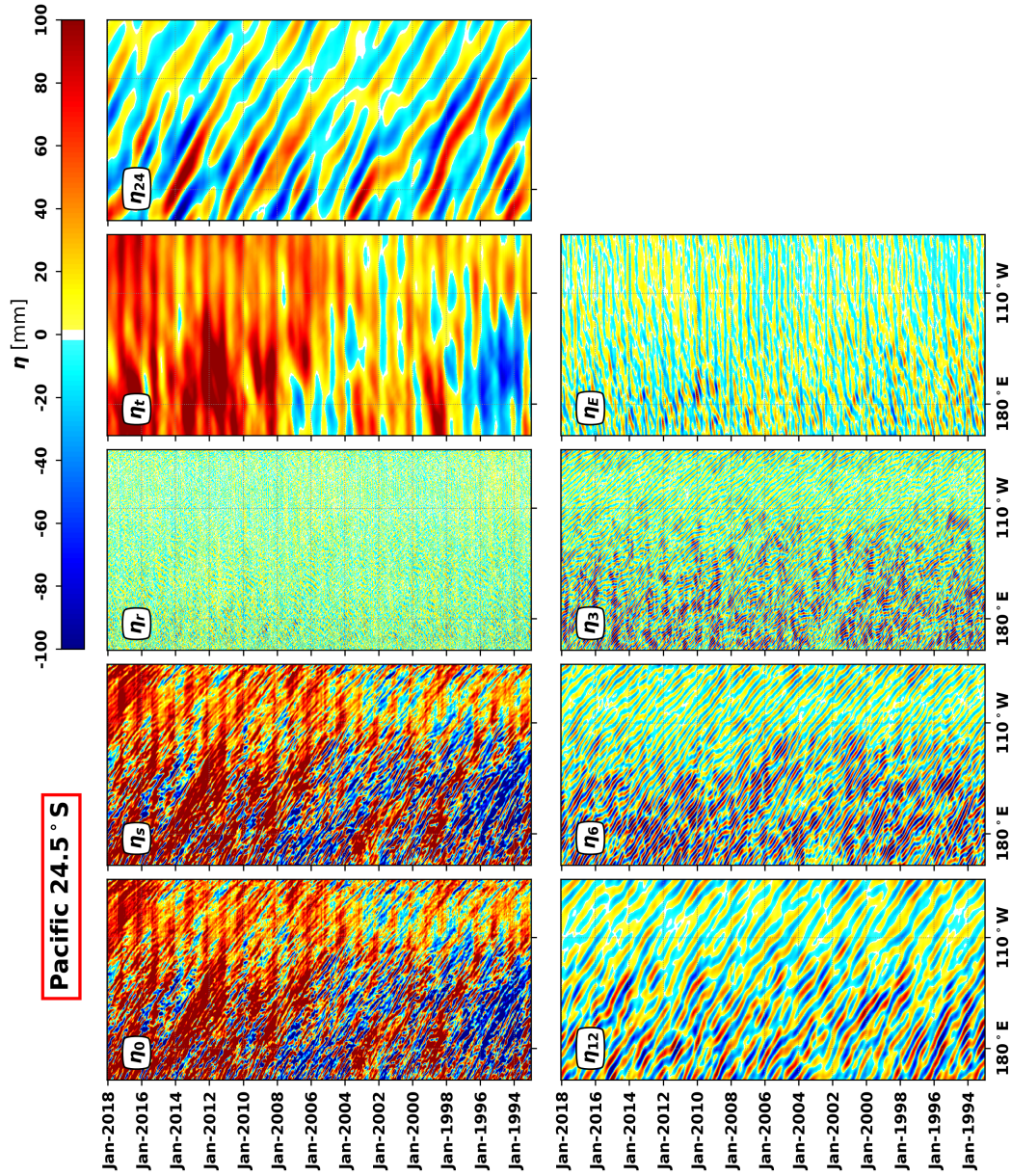

Figure 3.6: Similar to Figure 3.5 at 24.5°.

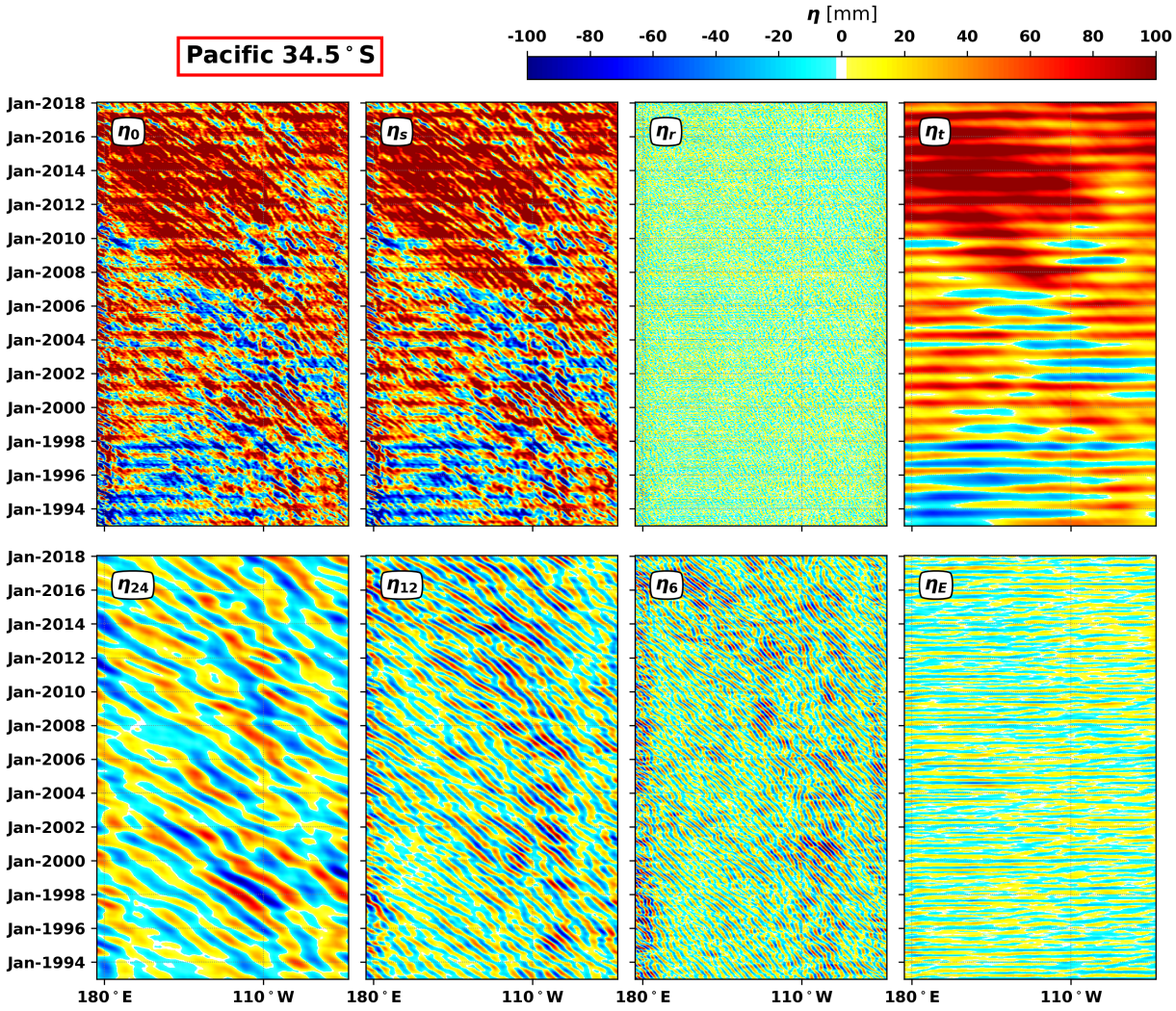

Figure 3.7: Similar to Figure 3.5 at 34.5°S.

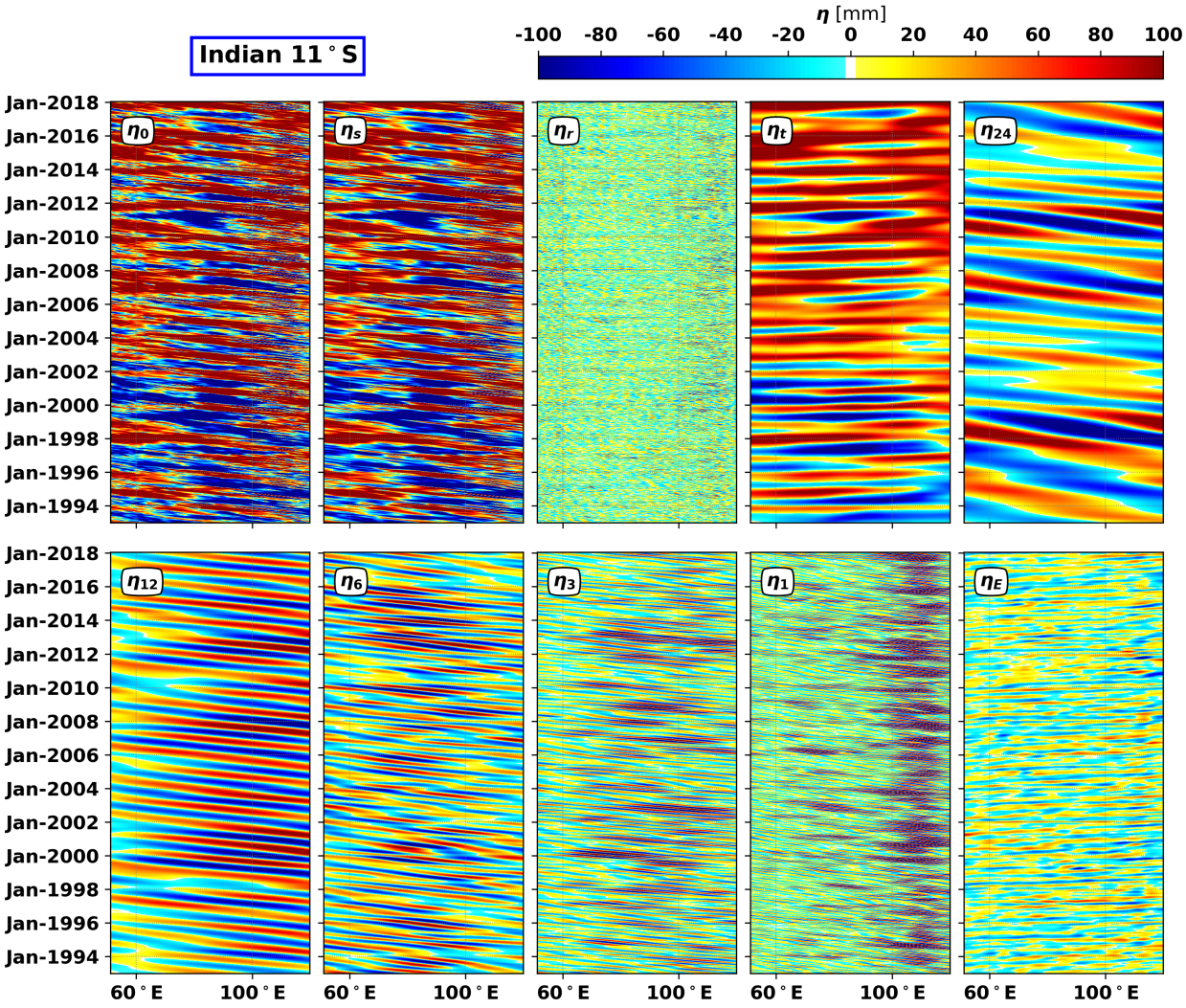

Figure 3.8: Similar to 3.2 for the Indian ocean at 11°S.

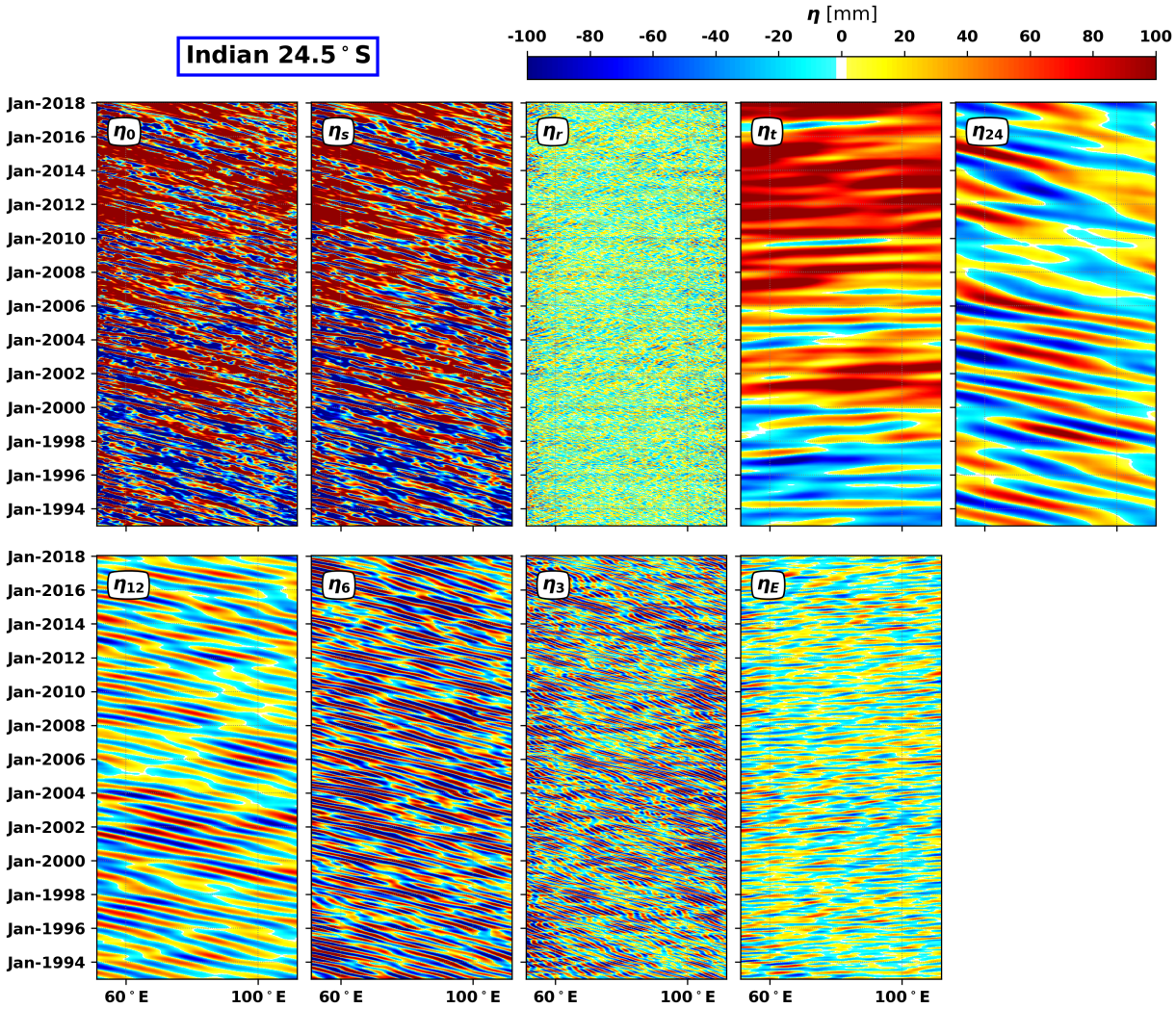

Figure 3.9: Similar to Figure 3.8 at 24.5°S.

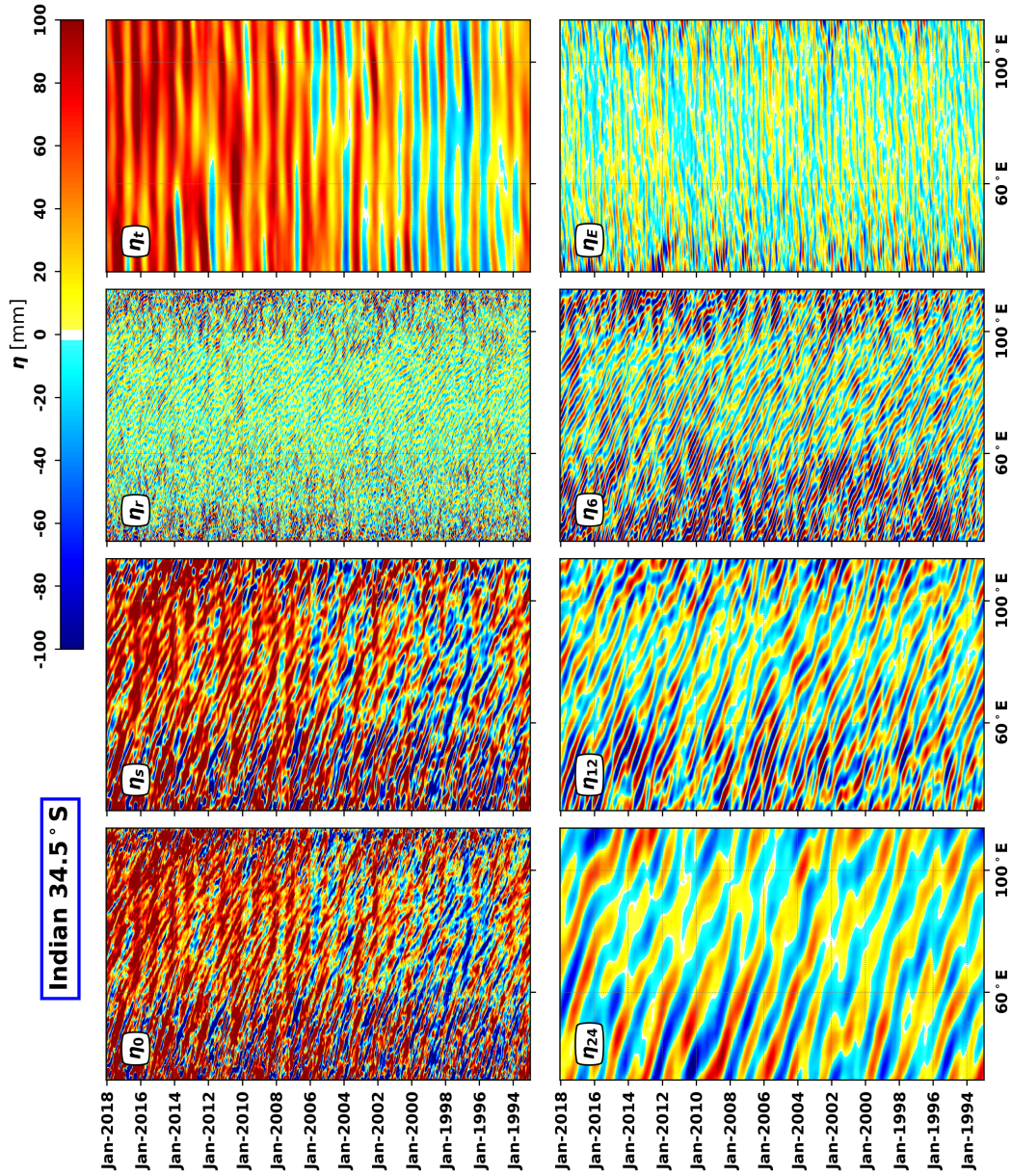

Figure 3.10: Similar to Figure 3.8 at 34.5°S.

3.2.1 Phase speed and amplitudes

As previously mentioned, long Rossby waves have most of their energy in the potential form (GILL, 1982). Therefore, an estimation of c_p would set the timescale for the energy to propagate from the east side of the basin to the west side. For the propagating signals, results can be seen in Tables 3.2, 3.3 and 3.4 for the Atlantic, Pacific and Indian oceans respectively. Waves are significantly faster when approaching the Equator, and the phase speed decreases with increasing latitude. This is due its dependence to the latitude, since

$$c_p = -\beta R_{di} = -\frac{NH\ \mathrm{cotan}(\phi)}{R}, \tag{3.10}$$

where ϕ is the latitude and R is the Earth's radius, 6371 km. Additionally, variations in c_p are also associated to changes in stratification (YANG, 2000), topography (TAILLEUX; MCWILLIAMS, 2001), wind forcing (LIU, 1999) and strong zonal currents through advection (KILLWORTH; BLUNDELL, 2003). These differences in phase speeds are easily identified in our results in all ocean basins.

Our results corroborate Polito and Cornillon (1997), Polito and Liu (2003), not a surprising fact since the methodologies are similar. Wang *et al.* (1998) have identified large-scale biannual and annual (9 to 10 months) Rossby waves on the Pacific at 25°S with phase speeds ranging from -5.5 to -6 km day^{-1}. We corroborate this result at some extent at 24.5°S, being the annual wave a bit slower (-4.75 km day^{-1}). This difference may be attributed the 0.5° offset and to different filtering techniques, since the authors used 1D filters.

Interestingly, although waves' c_p are similar within similar latitudes, amplitudes differ greatly among basins, especially at 11°S and 24.5°S. At 11°S, the η_{24} wave is the strongest signal (34%) on the Pacific, having c_p = -19.81 km day^{-1} and A = 55 mm. However, the same η_{24} component on the Indian ocean is slower (-17.04 km day^{-1}) but has the highest A (72 mm) and an explained variance of 17%. As for the Atlantic, η_{24} is the fastest (c_p = -31.12 km day^{-1}) but have a significant smaller amplitude, 16 mm only. In other words, the amplitude of η_{24} from the Indian (Pacific) Ocean is 350% (244%) larger than η_{24} from the Atlantic. These percentages are calculated in relation to the amplitudes in the Atlantic Ocean (Table 3.2), negative values meaning that amplitudes in the Atlantic are larger than the ones in the basin that is being compared.

As noted by Polito and Liu (2003), the Atlantic has the weakest Rossby wave signal in all basins. From our analysis, we corroborate that at 11°S and 24.5°S (Table 3.1).

Table 3.2: FIR2D results for the Atlantic basin: Amplitude (A) in mm, phase speed (c_p) in km day^{-1}, period (T) in days, wavelength (λ) in km and percentage explained variance (EV).

Latitude	Component	A	c_p	T	λ	EV
11°S	η_{24}	16	-31,12	370	-11488	20
	η_{12}	11	-12,13	347	-4214	3
	η_6	7	-22,91	14	-3341	3
	η_3	12	-11,61	113	-1278	8
	η_1	12	-8,35	68	-563	8
24.5°S	η_{24}	18	-5,94	764	-4419	9
	η_{12}	26	-4,38	337	-1445	16
	η_6	29	-4,35	159	-682	20
	η_3	20	-3,7	94	-340	13
34.5°S	η_{24}	36	-3,07	592	-1793	14
	η_{12}	55	-2,34	281	-633	30
	η_6	38	-1,28	143	-171	19

At 11°S , the Indian Ocean present the waves with the largest amplitudes (Table 3.4), followed by the Pacific (Table 3.3) and Atlantic (Table 3.2). Comparing the same wave components, waves in the Indian Ocean are 283% (η_3) to 742% (η_6) larger than the same ones in the Atlantic. At the same latitude, the amplitudes of Rossby waves in the Pacific are also larger than the same ones in the Atlantic, ranging from 34% (η_1) to 245% (η_{24}). At 24.5°S, c_p values become similar for waves with the same period. As the previous case, the Atlantic has the smallest amplitudes. For η_6, which has the same period of the seasonal cycle, the percentages of explained variance (EV) are different for the three basins, 3%, 8% and 14% respectively, but c_p values are similar: -4.35, -4,51 and -5.48 km day^{-1}. Given this result, some particularities can be inferred: this latitude is approximately the center of the subtropical gyres on the three basins, so that mean currents and shear are smaller compared to other locations; moreover, it is a region between the trade winds and the westerlies, therefore the wind contribution is relatively weak. With no external influences, i.e. advection and forcing, values of c_p converge to a value determined by R_{di}, which includes stratification. Despite this similarity, amplitudes are significantly different: 29, 49 and 94 mm respectively. In comparison to the Atlantic, waves amplitudes' are 42% (η_{12}) to 123% (η_{24}) larger in the Pacific and 96% (η_{12}) to 245% (η_3) larger in the Indian Oceans. The differences in amplitudes are smaller between components in relation to the previous latitude.

Intriguingly, at 34.5°S the Pacific Ocean present the weakest Rossby wave signal (Table 3.1) and the smallest amplitudes (Table 3.3) for all components. Thus, in comparison

Table 3.3: As in Table 3.2, for the Pacific basin.

Latitude	**Component**	**A**	c_p	**T**	λ	**EV**
11°S	η_{24}	55	-19,81	810	-15599	34
	η_{12}	37	-21,72	371	-8053	17
	η_6	19	-23,07	185	-4203	8
	η_3	18	-16,56	97	-1567	5
	η_1	16	-12,25	54	-645	3
24.5°S	η_{24}	40	-5,71	709	-4000	15
	η_{12}	37	-4,75	302	-1402	15
	η_6	49	-4,51	147	-650	27
	η_3	36	-3,37	103	-332	16
34.5°S	η_{24}	35	-2,71	613	-1604	17
	η_{12}	36	-2,25	282	-621	19
	η_6	32	-1,66	173	-272	16

Table 3.4: As in Tables 3.2 and 3.3, for the Indian basin.

Latitude	**Component**	**A**	c_p	**T**	λ	**EV**
11°S	η_{24}	72	-17,04	568	-9591	17
	η_{12}	72	-17,41	339	-5901	24
	η_6	59	-16,17	190	-3008	14
	η_3	46	-19,36	85	-1629	8
	η_1	47	-16,14	51	-825	10
24.5°S	η_{24}	59	-5,79	703	-3842	12
	η_{12}	51	-6,85	287	-1932	9
	η_6	94	-5,48	161	-877	33
	η_3	69	-4,33	97	-410	21
34.5°S	η_{24}	39	-3,96	647	-2513	12
	η_{12}	48	-3,54	301	-1039	23
	η_6	57	-3,3	147	-476	36

to the Atlantic, the amplitudes decrease (-3% – -35%), i.e., amplitudes are 3% to 35% smaller in the Pacific basin. The Indian Ocean is still the basin with the highest Rossby wave signal (67%) and the largest amplitudes (Table 3.4) for components η_{24} and η_6, 8% and 50% larger than the same components in the Atlantic. As for η_{12}, it is 12% smaller in the Indian Ocean. Besides that, differences in amplitudes at this latitude are not as high as in the previous ones (Tables 3.2, 3.3 and 3.3). The η_6 presents EV of 19%, 16% and 36% for the Atlantic, Pacific and Indian Oceans. For this component, amplitudes for the Atlantic and Pacific are very similar (38 and 32 mm), but larger in the Indian (52 mm). As for η_{24} and η_{12}, amplitudes are akin for the three basins and range from 35 to 55 mm. The c_p at this latitude are also similar, the Indian having the fastest waves. It remains to understand why these differences arise and how they are related to background stratification, i.e. variations in the PV field. We considered this topic in Chapter 1 and we address the results of this discussion in the following Sections of this Chapter.

According to Barnier (1988), wave amplitudes tend to be larger west of major topographic features, e.g. the Mid-Atlantic Ridge. The author simulated the North Atlantic and generated non-linear first-mode baroclinic Rossby waves forced by seasonal wind fluctuations using a two-layer model with uniform stratification. His main findings include the influence of the Mid-Atlantic Ridge on the waves' energy transfer from the baroclinic to the barotropic mode, as it acts as a barrier to block the westward traveling energy. Westward of the ridge, the opposite holds and the energy is transferred from the barotropic to the first baroclinic mode, generating a wave-train that continues to propagate westward. Thus, one can argue that topography may play an important role in amplifying these waves, which was further corroborated by Polito and Cornillon (1997) and Osychny and Cornillon (2004) for the North Atlantic. In comparison to the previous studies, our analysis include a larger time series, and we can see this amplification in some of our results, for example, in the Pacific at 24.5°S (Figure 3.6) and in the Indian at 34.5°S (Figure 3.10), when waves cross major topographic features. In these cases, amplitudes are enhanced and maintain its larger value until the end of the basin. However, Fu and Chelton (2000) showed that this is not always the case. In the Atlantic, waves are mainly uniform in terms of amplitudes (Figures 3.2, 3.3 and 3.4), and waves in the Indian Ocean behave in a similar manner. At 24.5°S (Figures 3.3 and 3.9), for example, the waves propagate across the entire basin despite the major topographic features and amplitudes at the eastern and western parts are maintained (FU; CHELTON, 2000, see also Figure 12).

3.2.2 Rossby radii of deformation (R_{di})

Consider a small perturbation in the pressure field. The fastest wave in an incompressible fluid is the shallow water wave (internal or external). The R_{di} is the length that this gravity wave travels in one inertial period. If a phenomenon has a characteristic length much larger than R_{di}, even at the fastest possible speed, the pressure perturbation that physically defines this phenomenon will experience the effects of planetary rotation. Besides that, as seen in the previous Sections, R_{di} plays an important role in phase and group speed of baroclinic Rossby waves. According to Chelton *et al.* (2008), the first baroclinic Rossby radius decreases from 240 km close to the Equator to less than 10 km at latitudes higher than 60°.

Houry *et al.* (1987) calculated R_{di} using T and S data provided by Levitus (1982) climatology between 30°N – 70°S, 70°W – 70°E. The N^2 profiles were calculated up to 2000 m and averaged on a 5°× 5° box. Several years later, Chelton *et al.* (1998) calculated R_{di} using a methodology similar to the one described in Section 2.2, however assuming a Wentzel-Kramers-Brillouin (WKB) approximation for the N^2 profile, which slightly modifies equation (2.4). The authors calculated 1°× 1° climatologies of the first baroclinic Rossby radius of deformation using climatological averaged T and S profiles, as well as the first baroclinic gravity-wave phase speed. They also investigated whether neglecting temporal variations in the stratification in the linear theory is justified when calculating R_{di}. If, at a given location, R_{di} significantly varied seasonally, one could argue that this assumption does not hold.

The variability of R_{di} depends on the latitude mostly because of its dependence on the Coriolis parameter. The higher (lower) the latitude, the lower (higher) R_{di} value. Moreover, stratification is weak in high latitudes and the dependence on N^2 also decrease R_{di}. Indeed, their results suggest that although seasonal variations of N^2 are large above the pycnocline, the net effect of density variations in the entire water column on R_{di} seasonal variation is little. Because of the dependence of c_p and R_{di}, Rossby waves' c_p in similar latitudes are alike.

Our R_{di} (Table 3.2.2) were calculated following the methodology described in Section 2.2 and Appendix A.1, as the eigenvalues of equation (2.4) for the three ocean basins of the Southern Hemisphere at 11°S, 24.5°S and 34.5°S. Each latitude has one associated N^2 profile, meridionally averaged. Therefore, the obtained R_{di} is an estimation of the whole longitudinal transect. Discrepancies arise when comparing the aforementioned studies

Table 3.5: Comparison between R_{di} (km) obtained based on the QG model. Our study used a longitudinal averaged N^2, Houry *et al.* (1987) used a $5^\circ \times 5^\circ$ averaged N^2 and Chelton *et al.* (1998) used a $1^\circ \times 1^\circ$ averaged N^2 and the WKB approximation.

Basin	**Latitude**	**Our study**	**Houry *et al.* 1987**	**Chelton *et al.* 1998**
Atlantic	11°S	70	73	87
	24.5°S	35	42	43
	34.5°S	23	28	32
Pacific	11°S	90	x	95
	24.5°S	39	x	46
	34.5°S	23	x	31
Indian	11°S	85	78	94
	24.5°S	38	48	48
	34.5°S	23	36	34

mainly because our study is based on T and S profiles from ISAS, which includes Argo buoys, with a spatial resolution of 0.5°. For each N^2 used in the calculation of R_{di} and the vertical modes, our T and S profiles were averaged over 14 years (2002 – 2015). Houry *et al.* (1987) and Chelton *et al.* (1998) used climatological annually averaged temperature and salinity profiles from the National Oceanographic Data Center (NODC), the latter based on Boyer and Levitus (1994). Besides, although methodologies are similar, Chelton *et al.* (1998) opted to approximate the N^2 profile to an exponential (WKB approximation), which was not done neither in our study nor in the study of Houry *et al.* (1987).

3.2.3 Are these waves first baroclinic?

The linear theory foresees first-mode baroclinic Rossby waves to have constant phase speed and a continuous phase throughout ocean basins, and mainly zonal propagation (GILL, 1982). The approximations of the linear theory reduce the problem to the zeroth-order dynamics, making it minimalist, but still provide reasonable results, e.g.: Watanabe *et al.* (2016). However, using constant c_p derived from a fixed β and a climatological R_{di} means to exclude other factors that may lead to variations in the background potential vorticity gradient. Several studies relate theoretical to observational c_p, reporting discrepancies between the linear theory and observations in terms of Rossby wave dynamics (HERRMANN; KRAUSS, 1989; DEWAR; MORRIS, 2000; KILLWORTH *et al.*, 1997; KILLWORTH; BLUNDELL, 2003). Herrmann and Krauss (1989) pointed out some reasons for these discrepancies: (i) the flow is forced (wind/buoyancy), meaning that it is not free; (ii) the ocean has a varying bottom; (iii) waves are nonlinear; and (iv) the ocean is not at rest. As the altimeters revised their accuracy and the time series grew, it became

possible to treat the waves by separating them from other non-propagating signals. For example, according to Chelton and Schlax (1996), Rossby waves identified by altimeters appear to propagate faster than the linear theory predicts. The authors claimed that outside the tropical band (10°N – 10°S), linear theory fails in predict first baroclinic Rossby wave phase speeds. One year later, Polito and Cornillon (1997) showed that despite Rossby wave propagation is mainly zonal, they do propagate in the meridional direction, generally to the northwest (southwest) above (below) 25°N in the North Atlantic Ocean. In this context, we expect our waves (Tables 3.2, 3.3 and 3.4) to be first-mode baroclinic.

According to Döös (1999), a perfect resonance between wind forcing and free waves would alter the amplitudes of the waves, but not the phase speed. For that to happen, the wind stress curl and waves should have not only the same frequency but also the same wavelength, repeating for a few wavelengths towards the ocean away from the coast. Considering the turbulent characteristics of both fluids, it is hard to believe that this would happen. If the phase is the same, the forced Rossby wave c_p would be different than that of a free wave. The precise form of the response under this resonance depends on eastern boundary conditions, but under some circumstances the forced response appears to have a c_p two times higher than the original wave. However, as pointed by Killworth *et al.* (1997), this resonance is hard to occur so precisely and everywhere in the ocean to uniformly increase the c_p, and it is also unlikely to occur at mid-latitudes.

Topography can also increase wave phase speeds (RHINES, 1970). However, as shown by Killworth and Blundell (1999), there is little evidence for overall increases in the c_p of Rossby waves by topography. The authors showed that although topography has influence locally, the net effect on the entire basin is negligible. In terms of nonlinearity, Anderson and Killworth (1979) found that it is related to changes in stratification if the waves are away from western boundary currents. However, seasonal variations in the stratification leads to small changes in R_{di} (CHELTON *et al.*, 1998). Thus, the vertical configuration necessary to change waves' phase speeds is unlikely to occur so easily.

Killworth and Blundell (2003) first proposed that a faster c_p may be explained by the presence of a background baroclinic mean flow, which changes the PV gradient, and changes in bottom topography. Discrepancies between phase speeds are small near the Equator, but increase poleward. Besides, the authors also found that, for long waves, the contribution of the mean flow is much more noticeable and representative than effects of varying bathymetry, also seen several years later by Maharaj *et al.* (2007). Except for the Antarctic Circumpolar Current and western boundary currents, the barotropic component

is not sufficiently large to affect this solution (KILLWORTH *et al.*, 1997). For a baroclinic flow, variations in the ray paths of Rossby waves are affected by variations in the thermocline. On one hand, linear theory is able to explain a significant part of the variability associated to Rossby waves when we include topography and mean flow interactions. On the other hand, this inclusion acts to mend the linear theory.

Motivated by the aforementioned studies, we compared the first mode dispersion curves for the classical linear Rossby wave theory and the same linear theory but adding a term ($\bar{u}_g\, k_x$) to account for the background mean flow. Both curves were computed for each basin at each latitude, and R_{di} was calculated using the ISAS reanalysis and the method described in Section 2.2 (See also Appendix A.1). Our main idea was to see whether the waves detected in the η fields from altimeter are of the first baroclinic mode, yet Doppler shifted.

Figure 3.11 shows the dispersion relation of first baroclinic Rossby waves. The dashed lines represent the classical linear theory, that is,

$$\omega = -\frac{\beta k_x}{k_x^2 + R_{di}^{-2}}\,, \tag{3.11}$$

and the solid lines the classical plus mean flow (hereafter *extended*). In that, ω is plotted as a function of period ($T = \frac{2\pi}{\omega}$) and wavelength ($\lambda = \frac{2\pi}{k_x}$), to facilitate the interpretation. The extended theory curve was computed by adding the background mean flow, which was defined, for consistency, as the average zonal geostrophic velocity ($\bar{u}_g$) from the altimeter over the entire domain for each basin at each latitude (Table 3.6), that is:

$$\omega = -\frac{\beta k_x}{k_x^2 + R_{di}^{-2}} + \bar{u}_g k_x\,. \tag{3.12}$$

We obtained $\bar{u}_g$ by averaging the zonal geostrophic velocity u_g temporally (1993 – 2018) and spatially (longitude). As the altimeter provides u_g at the surface, the averaged $\bar{u}_g$ represent only the barotropic component of the velocity.

Although our $\bar{u}_g$ values are relatively small (Table 3.6), differences between the linear and extended curves in Figure 3.11 are readily depicted. In general, waves tend to follow the extended theoretical curve. At 11°S, the linear and extended curves draw close in the long-wave limit for both the Pacific and Atlantic (Figure 3.11-a, b), but differ for the Indian ocean (Figure 3.11-c). This is due to a $\bar{u}_g$ 10 times higher in the Indian (compare $\bar{u}_g$ values in Table 3.6), leading to faster waves predicted by the extended curve. For the remaining latitudes, differences between the two curves are more striking, but less

Table 3.6: Averaged zonal geostrophic velocity $\bar{u}_g$ in $\mathrm{m\,s^{-1}}$ derived from the altimeter data for each basin at each latitude.

Basin	**Latitude**	$\bar{u}_g$
Atlantic	11°S	0.01
	24.5°S	0.02
	34.5°S	0.02
Pacific	11°S	0.01
	24.5°S	0.01
	34.5°S	0.02
Indian	11°S	0.16
	24.5°S	0.04
	34.5°S	0.04

pronounced between basins (see Figure 3.11-d to i).

Maharaj *et al.* (2007) pointed out that, in the tropics, linear theory performed better than the extended to account for Rossby wave energy in the South Pacific. At 11°S, our results suggest that the extended theory better fits the observed waves, but they are nearly indistinguishable, except for the shortest wavelength (η_1, Tables 3.2, 3.3, and 3.4). Curiously, for the Atlantic — where 41% of the sea surface height anomaly was explained by Rossby waves (Table 3.1) — our extended theory seemed not sufficient to explain c_p deviations from the linear theory. With increasing latitudes, all components better fit the extended curve (Figure 3.11-d to i).

The η_{24} and η_{12} components (Tables 3.2, 3.3, and 3.4) match our extended curve for all latitudes and basins. This result indicates that the barotropic background mean flow is primarily responsible for the offset in the phase speed c_p. Although the remaining wave components follow the extended curve tendency, variations in c_p are likely affected by other factors that introduce variations in the potential vorticity gradient, such as topography and current shear, as discussed in the previous Sections. Nevertheless, the correspondence to the first baroclinic mode is still satisfactory and we can conclude that the filtered waves are first-mode baroclinic.

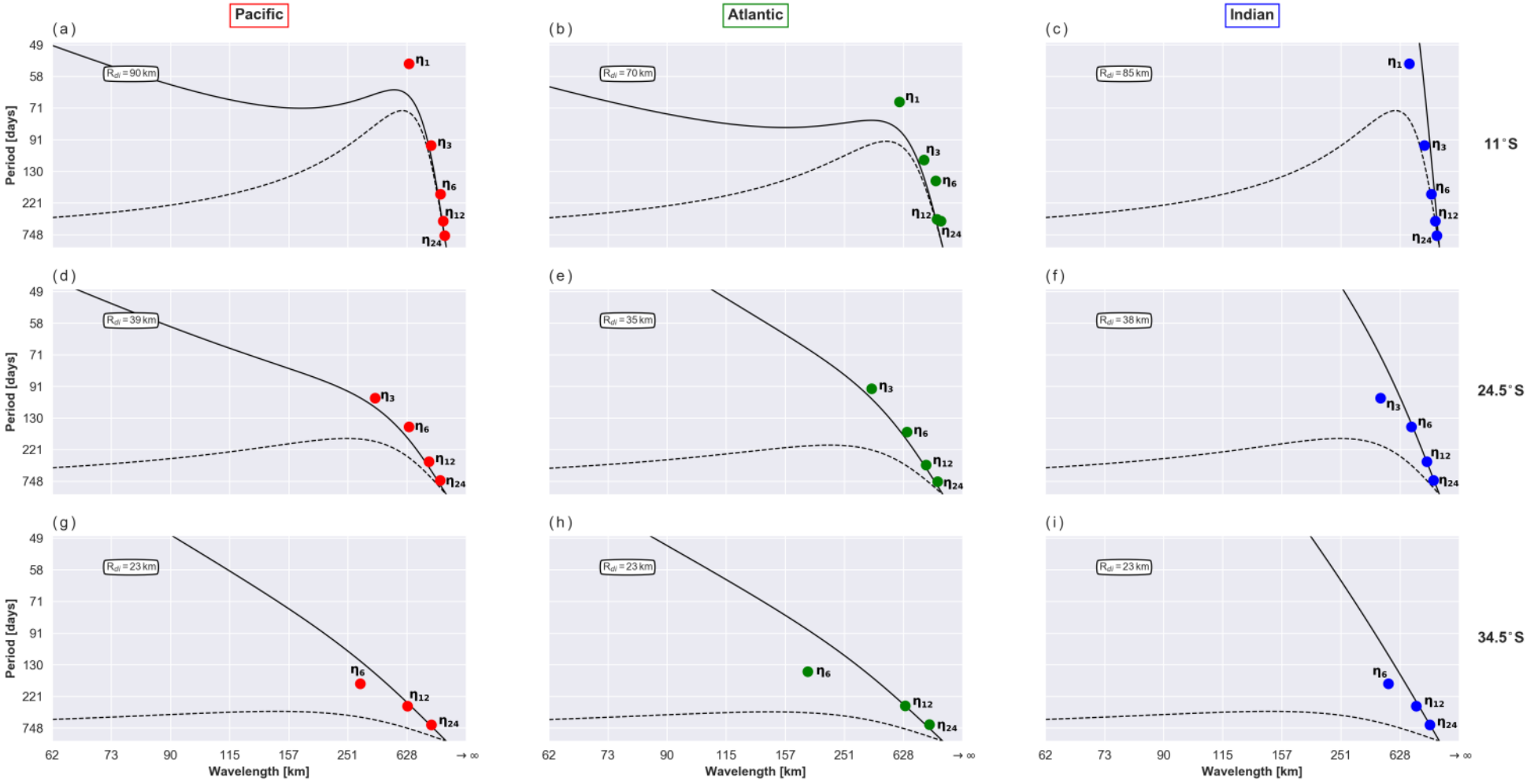

Figure 3.11: Dispersion relation of first baroclinic Rossby waves. Linear (dashed line) and extended theory accounting for mean flow only (solid line). Colored dots represent filtered Rossby waves according to the basin and latitude (Tables 3.2, 3.3 and 3.4). From the larger to the smaller wavelength, dots represent the η_{24}, η_{12}, η_6, η_3, and η_1 wave components.

3.3 A comparison between ocean basins

3.3.1 The similarity in wind forcing

The generation of Rossby waves is caused by variations in the PV field, which occur due to many physical processes, such as changes in buoyancy, the wind stress and its curl, baroclinic instabilities, variations in density and the magnitude of ocean currents (FRANKIGNOUL; MÜLLER, 1979; MÜLLER; FRANKIGNOUL, 1981; ANDERSON; CORRY, 1985; LIPPERT; KÄSE, 1985; BARNIER, 1988; HERRMANN; KRAUSS, 1989). In this Section, we focus on wind forcing.

Wind forces Rossby waves in all ocean basins (VIVIER *et al.*, 1999; BIROL; MORROW, 2001; CHU *et al.*, 2007). Liu (1999) suggested that the wind stress curl along the eastern boundary and Ekman pumping are the most effective mechanism to generate the non-Doppler-shifted mode Rossby wave, which resembles the first baroclinic mode but propagates regardless of the mean flow. This mode also has the biggest contribution to the sea surface height, the largest amplitude, and produces changes in the lower thermocline. Han and Lee (1985) presented the annual mean and the seasonal charts of wind stress and wind stress curl. The authors showed that the zonal mean of the annual zonal wind stress is similar for the three ocean basins. The mean zonal wind stress assumes negative values from 10°S to approximately 30°S, and positive values from that latitude towards the south pole (HAN; LEE, 1985, see Figure 3). With the advent of satellite data, Milliff and Morzel (2001) evaluated the time-average wind stress and its curl, revealing discrepancies between their results and previous studies, probably due to the improvement on spatial resolution. Several years later, the time series of satellite data grew larger and allowed improved statistics, particularly for longer periods (RISIEN; CHELTON, 2008; LEE *et al.*, 2013). Nevertheless, results of the large scale distribution of the wind fields in tropical and subtropical regions are still in accordance with classical theories (GILL, 1982).

Figure 3.12-a, to d shows wind stress and wind stress curl averaged from 01/1979 to 12/2018 and its standard deviations. We used data from the ERA-Interim (DEE *et al.*, 2011), a global atmospheric reanalysis produced and maintained by the European Centre for Medium-Range Weather Forecasts (ECMWF). Its spatial resolution is roughly 80 km, with 60 vertical levels from the surface up to 0.1 hPa. Comparing Figure 3.12-a and c, we can notice similarities between ocean basins in both fields, corroborating aforementioned studies. From 0° to 15°S the, wind stress curl assumes negative values

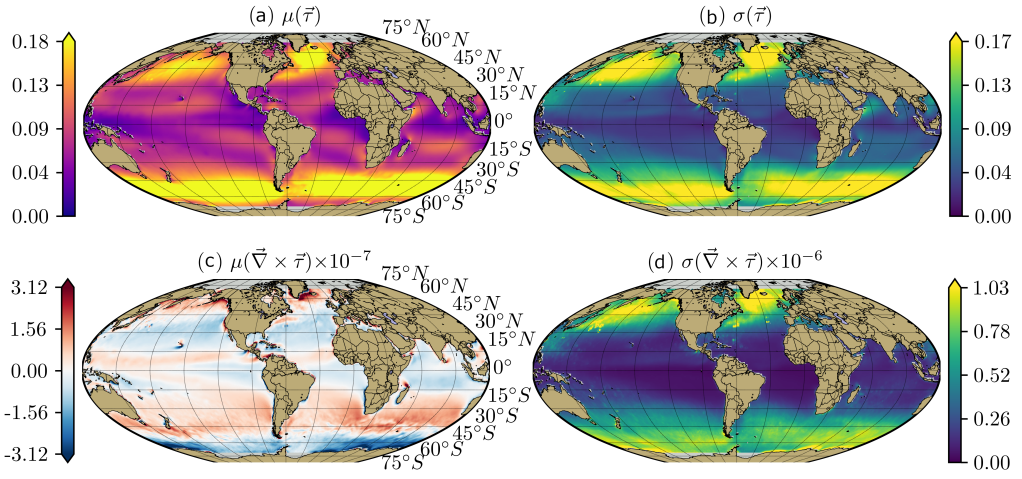

Figure 3.12: (a) Mean wind stress (τ) and (b) its standard deviation, and (c) mean wind stress curl ($\nabla \times \vec{\tau}$) and (d) its standard deviation (N m^{-2}). Courtesy of Dr. Paulo S. Polito.

(cyclonic), characteristic of tropical gyres. From 15°S down to 45°S winds, the typical subtropical gyre wind stress curl assumes an anti-cyclonic circulation, corroborating Han and Lee (1985), Milliff and Morzel (2001) and Risien and Chelton (2008). Moreover, the average wind stress is also similar: higher values are found near gyre borders (also where $\nabla \times \vec{\tau} = 0$) and below 45°S due to the westerlies. It is known that this configuration is typical of the Atlantic, Pacific, and Indian basins. Besides, the magnitude of $\vec{\tau}$ — as well as $\nabla \times \vec{\tau}$ — between basins is similar.

Wind stress produces a direct oceanic response in a thin layer near the surface: the Ekman transport. Spatial variations in the Ekman transport, generate convergence and divergence, resulting in vertical velocities. The Ekman pumping occurs along coasts as well as in the open ocean. For example, an anticyclonic circulation associated with a high-pressure center in the ocean yields convergence of the Ekman transport. Consequently, Ekman pumping is downward, which lowers the thermocline (GILL, 1982). At the eastern boundaries, e.g. the African coast in the South Atlantic, the wind is equatorward and parallel to the coast. Due to the Coriolis effect, the integrated Ekman transport is 90° to the left of the wind direction, causing divergence along the east coast, leading to coastal upwelling. The associated upward vertical movement of the thermocline at eastern boundaries is associated to the forcing of planetary waves (LIU, 1999; VIVIER *et al.*, 1999).

The spatial distribution of the standard deviation of the wind fields shown in Figure 3.12-d may suggest that the mechanism of generation of Rossby waves hardly vary among basins of the same Hemisphere, leading to Rossby waves of same amplitudes; to

be sure, we could quantify the energy flux from the wind into the waves, but due to time constraints we leave this analysis to future studies. Our results in Section 3.2.1 showed the opposite: the Rossby waves amplitudes vary among latitudes and basins. To address those differences, in the next Section we turn our attention to the vertical structure of the water column. We present results of a QG vertical-mode decomposition, calculated using the mean T, S, and N^2 from the ISAS climatology at 11°S, 24.5°S and 34.5°S.

3.3.2 Southern Hemisphere stratification and QG modes

In this Section we present the vertical structure of the barotropic (BT) and first and second baroclinic modes (BC1 and BC2), derived for the three ocean basins at 11°S, 24.5°S and 34.5°S (Figure 3.14), following the methodology described in Section 2.2.

The barotropic component ($i = 0$) represents the part of the flow that is depth-invariant, so that the vertical structure $F_0(z) = 1$ (green lines, Figure 3.14) and $R_{di} = \sqrt{gH}/f$. The baroclinic components ($i > 0$) are a result of different density distributions that vary with local T and S. Therefore, the vertical modes vary with different density profiles. Unlike the barotropic mode, the vertical structure of the baroclinic components are depth-dependent and have i zero-crossings in z (yellow and red lines, Figure 3.14). Larger i means higher modes and smaller values of R_{di}. As for the first baroclinic mode ($i = 1$), the zero-crossing represents an estimation of the main pycnocline depth. In our analysis, the main thermocline is analogous to the main pycnocline because temperature has a much larger contribution to the potential density structure than salinity (TALLEY *et al.*, 2011), since our profiles are concentrated in mid-latitudes and averaged. Salinity becomes more important than temperature in high-latitude regions (near Antarctica, for example), when precipitation or ice melting creates a layer of low salinity at the surface, and in coastal areas and estuaries. The main thermocline is the region of the ocean where T and S rapidly vary, and it is typically in the upper 1000 m (VALLIS, 2006). As for the MLD, typical values for the latitudes of interest range between 10 and 200 m (BOYER-MONTÉGUT *et al.*, 2004).

From Figure 3.13 one can notice differences in N^2 at each latitude and basin. These profiles were computed as a longitudinal average considering the ISAS time series of T and S profiles from 2002 to 2015. At 11°S, the seasonal thermocline is practically absent and profiles are typical of a tropical ocean (HOURY *et al.*, 1987). Up to 100 m, N^2 profiles are very sharp, especially in the Indian ocean, which is the most stratified (Figure 3.13-a). Differences between ocean basins are easily noticeable, being the Atlantic the

less stratified, followed by the Pacific and Indian. Moreover, the MLD — estimated as the depth of maximum N^2 — is shallower at the Atlantic with 65 m, reaching 75 and 95 m in the Indian and Pacific Oceans. From the modal decomposition, we estimated the main thermocline being at 800, 530 and 590 m depth for the Atlantic, Pacific and Indian Oceans.

At 24.5°S, the stratification drops to nearly half of that of 11°S (Figure 3.13-b), nevertheless the Indian Ocean being more stratified. The Atlantic and the Pacific Oceans have a similar profile up to the MLD, differing from 65 m downward. The Pacific and Indian Ocean profiles suggest that the main thermocline resides between 600 to 1200 m. From our mode analysis (Figure 3.14-d, e and f), we estimated it to be at 660 m on the Pacific and 840 m on the Indian. The seasonal thermocline is present, being more apparent on the Pacific ocean (Figure 3.13-b, red line bump between 200 and 500 m).

Lastly, at 34.5°S stratification drops even more and up to 100 m the N^2 profiles are visually identical (Figure 3.13-c). The main thermocline is shallower at the Atlantic, around 700 m, in comparison with the Pacific and Indian Oceans, between 700 and 1300 m. We corroborate that with our modal analysis, since we found 850, 900 and 960 m for the Atlantic, Pacific and Indian Oceans (Figure 3.14-g, h and i). Seasonal thermocline is again more pronounced at the Pacific, but can be seen in the three ocean basins (bumps in Figure 3.13-c). As for the MLD, differences are less noticeable both at 24.5°S and 34.5°S, ranging between 55 and 65 m. Below 1000 m, all profiles remain close to zero because of the relatively smaller variation in density at these depths.

In Section 3.2.1, the two largest differences in waves amplitudes between the same components were seen at 11°S and 24.5°S (Tables 3.2, 3.3 and 3.4), which were also the latitudes with the biggest difference in stratification (Figure 3.13). From our mode analysis, at 11°S the Atlantic has the deepest thermocline, around 800 m (Figure 3.14-a, b and c), associated to the weakest stratification (Figure 3.13). At 24.5°S, the estimate of the thermocline depth on the Atlantic was very close to that of the Indian basin, but again the former presented the least stratified profile and the shortest waves (compare amplitudes in Tables 3.2 and 3.4). In addition, at 34.5°S N^2 profiles and thermocline depth are similar for the three ocean basins (Figure 3.13-c), and thus it is difficult to assess which basin is more stratified. At this latitude, η_{24} had equivalent amplitudes at all basins (Tables 3.2, 3.3, and 3.4). As for η_{12}, the similarity in amplitudes is between the Atlantic and Indian Oceans (Tables 3.2 and 3.4) and for η_6 is between the Atlantic and Pacific Oceans (Tables 3.2 and 3.3).

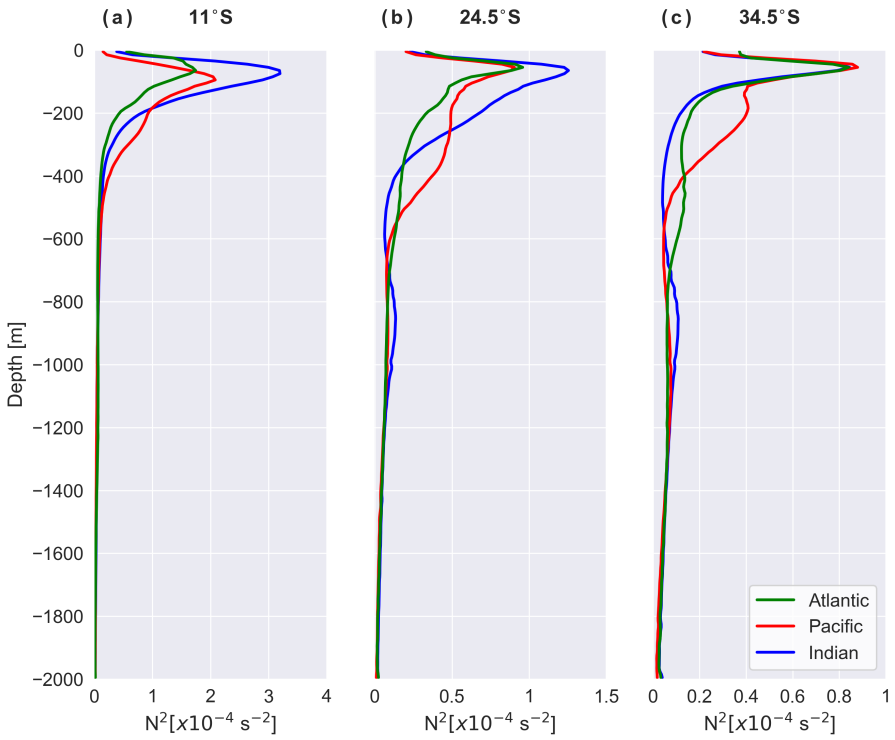

Figure 3.13: Squared Brunt-Väisälä frequencies (N^2) for the Atlantic, Pacific and Indian Oceans at 11°S, 24.5°S and 34.5°S.

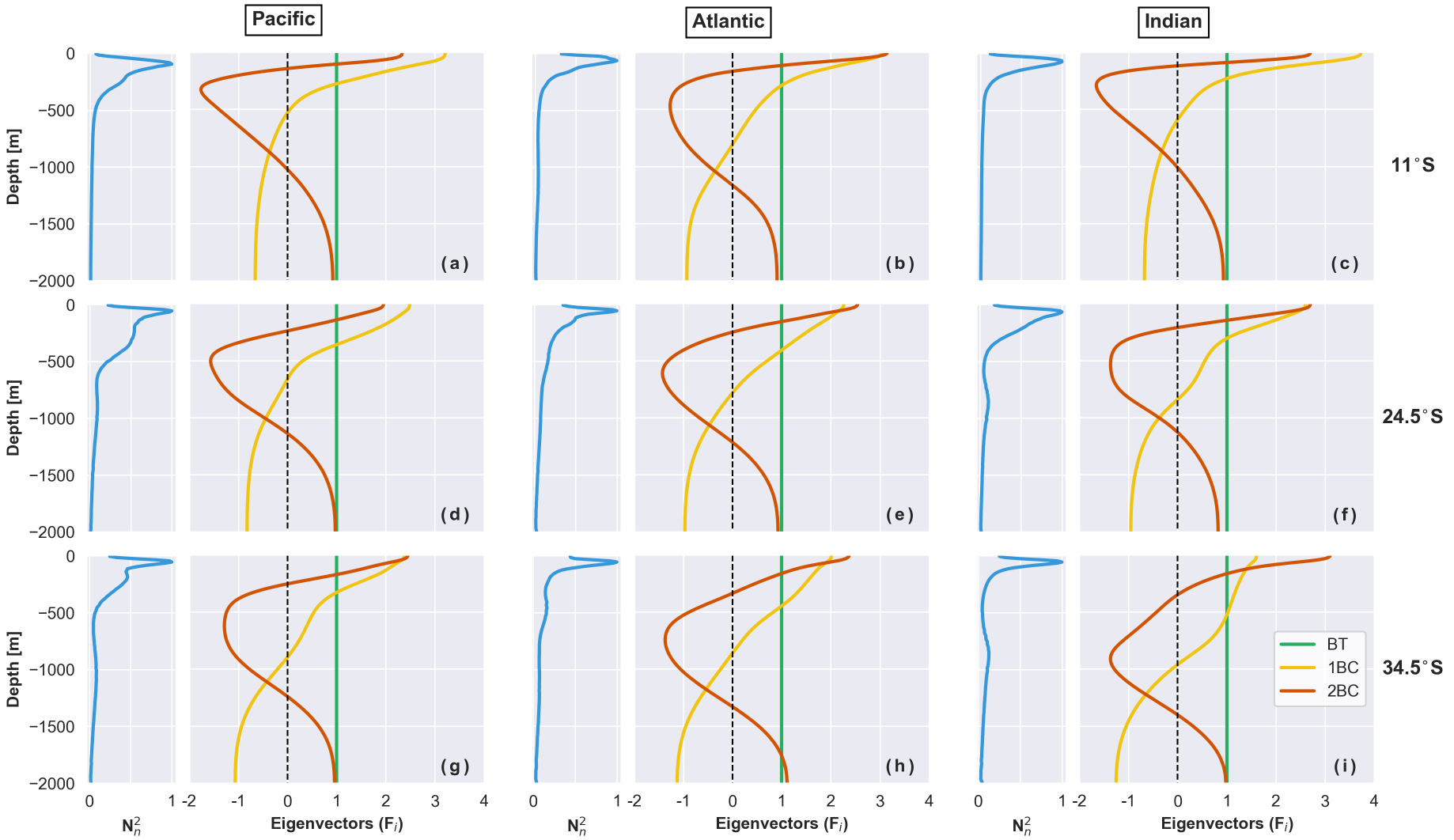

Figure 3.14: Vertical modes (F_i, unitless) eigenvectors of equation (2.4) solved using the ISAS climatology and normalized N_n^2 obtained from the same dataset for the Atlantic, Pacific and Indian Oceans at 11°S, 24.5°S and 34.5°S.

3.3.3 Sea surface height reconstruction

Using T and S from the ISAS dataset, we obtained the vertical structure F_i for each of the first three modes ($i = 0, 1$ and 2), discussed in Section 3.3.2. In this Section, we calculated the modal amplitudes $\mathbb{U}_i$ and $\mathbb{V}_i$ (Equation 3.5) using HYCOM's velocity vertical profiles to obtain the modal amplitudes Ψ_i related to the total streamfunction ψ (Equation 3.7). Subsequently, ψ — and consequently η — is calculated by the truncation of the first three modes (Equation 3.8). To evaluated how each mode contributes to the η variations we calculated the explained variance as in equation (3.9) but for the total streamfunction ψ_t and ψ_i is the streamfunction relative to each mode (or a combination of modes). We calculated EV for each mode individually and a combination (truncation) of two and three modes (Table 3.3.3).

Thompson *et al.* (2002) pointed out that each vertical mode contributes to the η signal having different spatial and temporal structures. From our Hovmöller diagrams (Figures 3.2 to 3.10) and from the corresponding phase speed (Tables 3.2 to 3.4), we could identify that the strongest Rossby wave signal is associated to BC1, which also corroborates our discussion in Section 3.2.3. Although we are only examining the sea surface, it is worth mentioning that it is possible to reconstruct the streamfunction in the ocean interior as a sum of each mode vertical contribution, because the vertical modes are orthogonal.

Recalling Section 2.2, the relationship between the modal amplitudes $\mathbb{U}_i$ and $\mathbb{V}_i$ and the modal amplitude of the streamfunction Ψ_i is

$$\left[\mathbb{U}_i, \mathbb{V}_i\right] = \left[\frac{-\partial}{\partial y}, \frac{\partial}{\partial x}\right]\Psi_i \,. \tag{3.13}$$

and the modal amplitude of the streamfunction Ψ can be solved by an elliptic equation,

$$\nabla^2\Psi_i = \underbrace{\frac{\partial \mathbb{V}_i}{\partial x} - \frac{\partial \mathbb{U}_i}{\partial y}}_{\stackrel{\text{def}}{=}\zeta} \,. \tag{3.14}$$

For each (x,y) box, we detrended and periodized ζ with mirror symmetry (ISERN-FONTANET *et al.*, 2006). In the Fourier analysis, this step prevents spectral leakage and discontinuities at the borders. In the Fourier domain,

$$\hat{\Psi}_i = \begin{cases} \frac{-\hat{\zeta}}{k_x^2+k_y^2}, & k_x^2 + k_y^2 \neq 0 \\ 0\,, & k_x = k_y = 0\,. \end{cases} \tag{3.15}$$

We retrieve the modal amplitudes Ψ_i applying the inverse Fourier transform on $\hat{\Psi}_i$, since the Fourier transform has an exact inverse. In other words, knowing the frequency and phase information of a signal allows us to precisely recover the original form of the same signal. Then, having Ψ for each mode we reconstructed the total streamfunction ψ and consequently η (Equation 3.8) as a truncation of the first three modes for the Atlantic, Pacific and Indian Oceans. To maintain consistency with the fields to be compared, we defined our η from the altimeter (hereafter η_a) to be the one calculated using the geostrophic velocities provided by the aforementioned dataset. We used the geostrophic velocities calculated based on the sea level anomaly in equations (3.14) and (3.15) to obtain ψ and η_a. Therefore, we are introducing the same bias in both the reconstructed and the "new" altimeter sea surface height. Moreover, we ensured that our reconstructed η fields (hereafter η_{rec}) using HYCOM's velocities preserved the variance of the original altimetric sea level anomaly field by multiplying each field by a constant factor defined as the RMS of the latter divided by the RMS η_a (NAPOLITANO *et al.*, 2019).

Figures 3.16, 3.15 and 3.17 show η_a, derived from altimeter's geostrophic velocities, and η_{rec}, calculated using HYCOM's velocities and ISAS T and S, for all latitudes at each ocean basin. Correlations between both fields were higher (0.69 – 0.85) in the Pacific and Indian Oceans than in the Atlantic (0.58 – 0.7). In all cases propagating signals can be detected in both fields. This result implies that few vertical modes can provide sufficient information on Rossby wave dynamics, corroborating Maharaj *et al.* (2007). The correlation values suggest both the altimeter data and the reanalysis outputs detect the same phenomenon, and most of the variability takes place at the vertical range sampled by Argo profilers. We also can notice an amplification on both η_a and η_{rec} at 24.5°S on the Pacific ocean, higher in the western part of the basin, also detected in our analysis in Section 3.2.1, and variations towards a slower c_p with increasing latitude in all basins, noticeable in the change of inclination patterns.

The BC1 should be dominant in mid-latitudes and when approaching the Equator the BC2 should gain more importance. As for the BT, it should be present at all latitudes and too fast to be detected by altimeters (POLITO; LIU, 2003), having higher contributions at high latitudes. As expected, results (Table 3.3.3) show that the BC1 has the highest contribution and dominates the η signal at all latitudes. The BT component gains importance poleward, as seen in the third column of Table 3.3.3. As for the BC2, it is much less important than both the BT and BC1, but still consistently contributes to 2 to 19% of the explained variance of the sea surface height signal, being more important at 11°S on the

Table 3.7: Explained variance for each modal component to the total ψ field calculated using HYCOM velocities, for each ocean basin.

Basin	Latitude	BT	BC1	BC2	BT + BC1	BC1 + BC2	BT + BC1 + BC2
Atlantic	11°S	35%	70%	15%	71%	76%	84%
	24.5°S	57%	67%	3%	82%	64%	87%
	34.5°S	75%	79%	9%	89%	74%	91%
Pacific	11°S	40%	75%	2%	78%	76%	83%
	24.5°S	64%	86%	6%	89%	85%	92%
	34.5°S	75%	83%	19%	87%	82%	88%
Indian	11°S	55%	89%	9%	89%	88%	94%
	24.5°S	74%	90%	12%	92%	90%	96%
	34.5°S	81%	77%	5%	92%	59%	93%

Atlantic. As mentioned before, the inclusion of the third baroclinic mode resulted in an increase of no more than 2% of the EV of the three mode truncation (last column, Table 3.3.3), and because of that this component was disregarded.

Both the reconstructed signal (η_{rec}) and η_a (Figures 3.16, 3.15 and 3.17) were filtered using the method described in Section 3.1.2, and propagating features are easily identifiable. The η_{rec} and η_a agree at all latitudes and present the same waves. Therefore, we stick our observations and the following discussion to the propagating features found in η_{rec} and η_a.

Subsequently, to check the effect of stratification on η, we did the following experiment: we reconstructed the sea level anomaly for the Atlantic basin using stratification profiles that belong to the Pacific and the Indian basins. In other words, we changed the Atlantic vertical structure F to reconstruct the η field in order to detect changes in waves amplitudes, using the same filtering process. From Section 3.2.1, differences in waves amplitudes ranged from 34% (η_1) to 244% (η_{24}) between Atlantic and Pacific and from 283% (η_3) to 742% (η_6) between Atlantic and Indian Oceans. These percentages are calculated in relation to Atlantic's waves amplitudes. For example, at 11°S, the amplitude of η_{12} in the Pacific Ocean is 235% larger than the same component in the Atlantic (See Tables 3.2 and 3.3). Surprisingly, at 11°S the detected Rossby waves amplitude differences in η_{rec} were small compared to what was observed in Section 3.2.1 with the altimeter data, with differences ranging from -5% to 120%, negative values meaning a decrease in amplitudes. For example, the η_{24} obtained from the altimeter measurements had an amplitude of 16 mm (Table 3.2). With a more stratified water column — using N^2 from the Indian ocean — the resulting amplitude was 21 mm, 31% larger than the one obtained with the η_{rec} from the Atlantic Ocean. However, from results in Section 3.2.1, we were

expecting an amplitude close to 55 mm, i.e. an amplitude 250% larger. The more striking result at this latitude was obtained for the η_6 component between the Atlantic and Indian Oceans, with the amplitude of the latter being 120% larger than the former basin. However, η_3 presented an amplitude 5% smaller than the same one in the Atlantic. It is worth mentioning that at 11°S the Atlantic presented the lowest $\eta_a - \eta_{rec}$ correlation (0.58) and the lowest EV for the first baroclinic mode (BC1, Table 3.3.3). In addition, from Figure 3.11-c, the η_3 component fits the extended curve, suggesting it is predominantly linear. Thus, geostrophy is dominant and the relationship between the sea surface height and stratification is well established. However, from Figure 3.11-b, the same component for the Atlantic departs from both the extended and the linear curve, suggesting that the Doppler-shift is not sufficient to explain the increase in c_p. Assuming that topography and the wind stress curl variability are similar, it is suggested that non-linearity becomes important for that wave, and thus the influence of stratification in sea surface height is decreased.

A better scenario arises at 24.5°S: from Section 3.2.1, amplitude differences ranged from 42% to 245%. From our experiment, changes in waves amplitudes ranged from 46% to 115%, and the mean is around 90%. Using the Indian (Pacific) stratification, amplitudes were 108% (80%), 114% (90%) and 100% (94%) larger for η_{24}, η_{12} and η_6, respectively. This result suggests that for a more stratified profile, waves can double their amplitudes. Although this is closer to what was observed in Section 3.2.1, these differences were not as large as the ones observed with the altimetric record. For example, for the η_{24} component, its amplitude obtained from the reconstruction using Indian (Pacific) stratification was 108% (80%) larger than that of the unchanged Atlantic, while in Section 3.2.1 the percentages were around 228% (123%). Finally, at 34.5°S, N^2 profiles (Figure 3.13-c) and the wind stress curl (Figure 3.12-c, d) are similar among basins, thus minor changes in waves' amplitudes were expected. Indeed, differences were smaller in comparison to the previous latitudes, ranging from -6% to 41%. According to Section 3.2.1, the amplitudes of η_{24}, η_{12} and η_6 should be similar among basins, but smaller in the Pacific. Yet, only η_6 decreased its amplitude (-6%) when we used the stratification from the Pacific Ocean. Therefore, it was possible to identify the role played by stratification on the modification of waves' amplitudes, although differences were not as high as the ones detected with the altimeter in Section 3.2.1, especially at 11°S and 24.5°S.

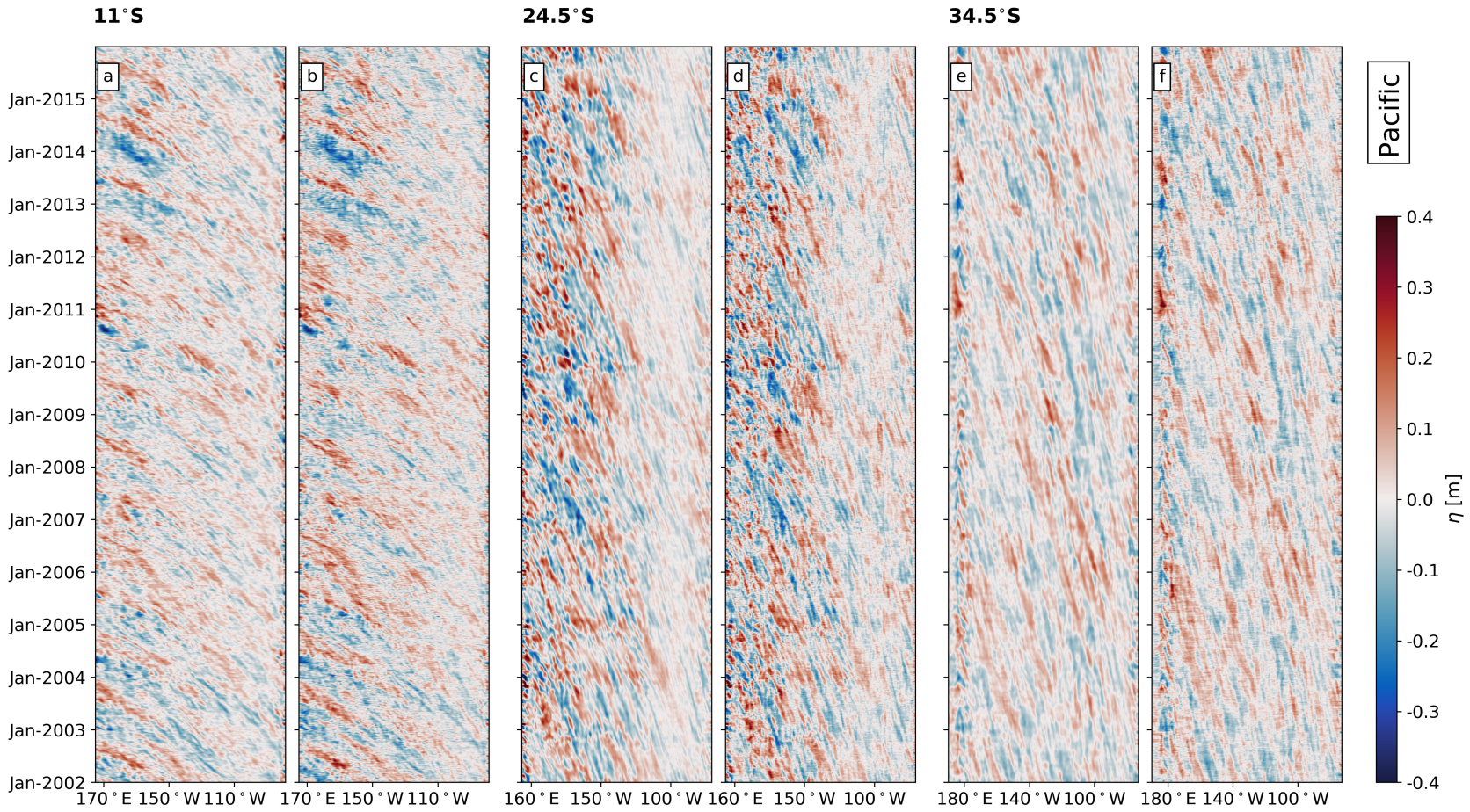

Figure 3.15: Hovmöller diagrams of sea level anomaly, η_a, calculated from geostrophic velocity anomalies from the altimeter (a, c and e) and η_{rec}, derived from the 3-mode truncation using velocity anomalies from HYCOM and the ISAS climatology (b, d and e) for the Pacific ocean at (a, b) 11°S, (c, d) 24.5°S and (e, f) 34.5°S.

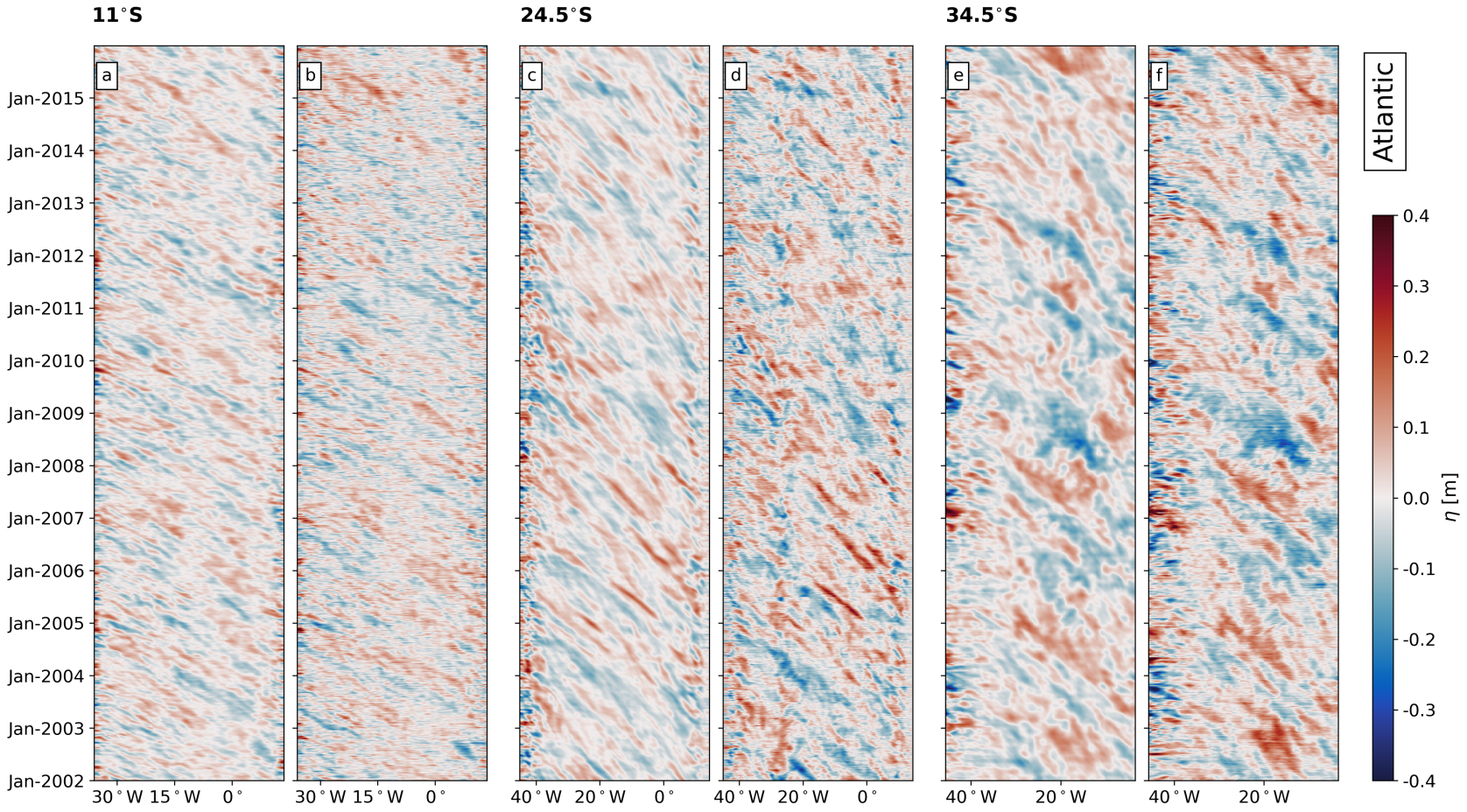

Figure 3.16: Similar to Figure 3.15, for the Atlantic ocean.

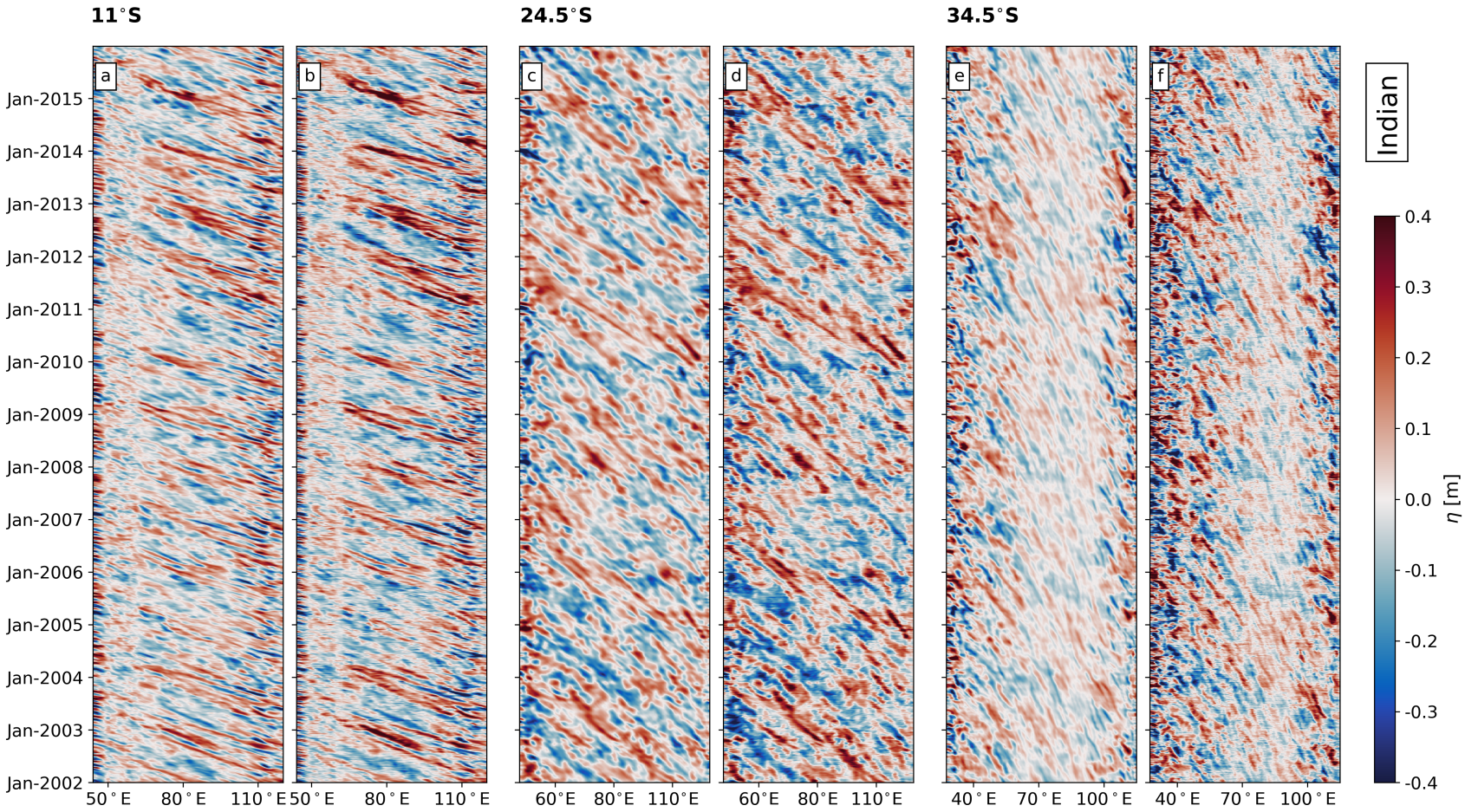

Figure 3.17: Similar to Figure 3.15, for the Indian ocean.

From equations (3.5) and (3.8), it is clear that a change in $F_i(z = 0)$ would result in a change of the reconstructed η field, thus changing its amplitude. We have observed that a more stratified water column, i.e. higher values of N^2, leads to larger mean wave surface amplitudes for each spectral band in our η_{rec}. These results suggest that stratification can modulate Rossby waves amplitudes, but we could not detect amplitude differences as large as those detected by the altimeter (Section 3.2.1) only by substituting the vertical structure F. Hence, we aimed for a comparison among ocean basins: at the same latitudes, η_{rec} was reconstructed using the modal amplitudes Ψ derived from HYCOM and the vertical structure F from the ISAS climatology, for each ocean basin. The main objective of this second experiment is to observe if the differences in amplitudes among basins using the modal reconstruction are close to those obtained by the altimeter analysis (Section 3.2.1).

For the Pacific and Indian Oceans, η_{rec} was calculated as a three mode truncation (Equations 3.5, 3.7, and 3.8), which represents more than 83% of the total surface field (Table 3.1), to be compared with η_{rec} from the Atlantic. We then applied the same filtering process to separate propagating and non-propagating signals, as in the previous experiment. Furthermore, we analyze if, on average, the modal amplitudes and the vertical streamfunction of the first baroclinic mode, i.e. Ψ_i and ψ_1 respectively, differ.

At 11°S, the differences in waves amplitudes were larger in relation to the first experiment, and also when comparing the three ocean basins. For example, the amplitude of η_{24} is 63% larger in the Pacific than the amplitude of the same component in the Atlantic. When comparing the Atlantic with the Indian Ocean, the positive difference in amplitude is even higher, 107%. Overall, we detected higher differences than the previous experiment, ranging from 63% to 365%. However, at 24.5°S differences were smaller than the first experiment comparing the Atlantic with the Pacific Oceans, ranging from -8% to 43%. For example, the η_{24} presented a negative difference of 8%, and η_6 a positive difference of 13%, meaning that η_{24} (η_6) had a smaller (larger) amplitude in the Pacific in relation to the Atlantic Ocean. Nevertheless, the amplitude of η_{12} was raised in 45%, in excellent agreement with the 42% presented in Section 3.2.1. As for the Atlantic and Indian basins, at this latitude results were similar to the first experiment, ranging from 76% to 110%. Lastly, at 34.5°S, differences in waves' amplitudes related better to the ones of Section 3.2.1, using the altimeter data. Comparing the Atlantic and the Pacific Oceans, the latter had the smallest amplitudes, so the differences were negative (-8% to -40%), in consonance with Section 3.2.1. Amplitude differences were smaller regarding

the previous latitudes, ranging from -40% to 52%, what was already expected, since N^2 profiles (Figure 3.13) and the wind stress curl (Figure 3.12-c, d) are similar. Poleward and with a less stratified water column, all waves presented smaller differences in amplitudes, in accordance to our previous results.

The time-averaged modal amplitudes ($\overline{\Psi}_1$) and the vertical streamfunctions ($\overline{\psi}_1$) for the first baroclinic mode are presented in Figures 3.18, 3.19, and 3.20 for the three ocean basins at each latitude. The comparison of the filtered waves in η_{rec} among basins (second experiment) suggested that the vertical structure of the velocities also play an important role in modulating Rossby waves' amplitudes. The BC1 strongly dominates the sea surface signal for all basins and latitudes except for the Indian Ocean at 34.5°S, where the BT is dominant (Table 3.3.3). Additionally, since the Rossby waves analyzed here are of the first baroclinic mode, we present a sectional perspective of $\overline{\psi}_1$ from 0 to 2000 m.

Excluding western boundary regions, at 11°S the modal amplitude for the first baroclinic mode range from -0.25 to 0.3 $\times 10^3$ m^{2}s^{-1} for the Atlantic, -0.42 to 0.65 $\times 10^3$ m^{2}s^{-1} for the Pacific, and from -0.62 to 0.91 $\times 10^3$ m^{2}s^{-1} for the Indian Oceans (Figure 3.18, upper panels). In absolute values, the Atlantic presented the smallest modal amplitude ($\overline{\Psi}_1$) in relation to the Pacific and Indian Oceans, leading to the weakest $\overline{\psi}_1$ (Figure 3.18) of all basins. Besides, at this latitude, Rossby waves explained the least variance of the surface signal (Table 3.1). Figure 3.18-c shows that the Indian Ocean has the strongest first baroclinic mode structure, both the modal amplitude $\overline{\Psi}_1$ and the streamfunction $\overline{\psi}_1$ are larger in absolute values in comparison with the other two basins. In addition, Rossby waves dominate (69%) the sea surface height signal (Table 3.1), and we found the waves with the largest amplitudes in the Indian Ocean (Table 3.4).

At 24.5°S, Rossby waves have a larger contribution in the sea surface height signal (Table 3.1) and the modal amplitude $\overline{\Psi}_1$ present larger absolute values for all basins in relation to the previous latitude (Figure 3.19). Differences between the first baroclinic mode streamfunction $\overline{\psi}_1$ are more noticeable at this latitude, especially between the Indian and the other two basins. The Indian Ocean remains the basin with the strongest first-mode baroclinic structure, the modal amplitude ranging from -1.6 to 0.45 $\times 10^3$ m^{2}s^{-1}, followed by the Pacific, with the modal amplitude between -0.58 and 0.48 $\times 10^3$ m^{2}s^{-1} and the Atlantic, ranging from -0.56 to 0.37 $\times 10^3$ m^{2}s^{-1} (Figure 3.19, upper panels). Differences between Rossby waves amplitudes at 24.5°S were smaller (See Section 3.2.1) than those of 11°S. Nevertheless, the Indian Ocean presented the waves with the largest amplitudes (Table 3.4), followed by the Pacific (Table 3.3) and the Atlantic (Table 3.3), similar to

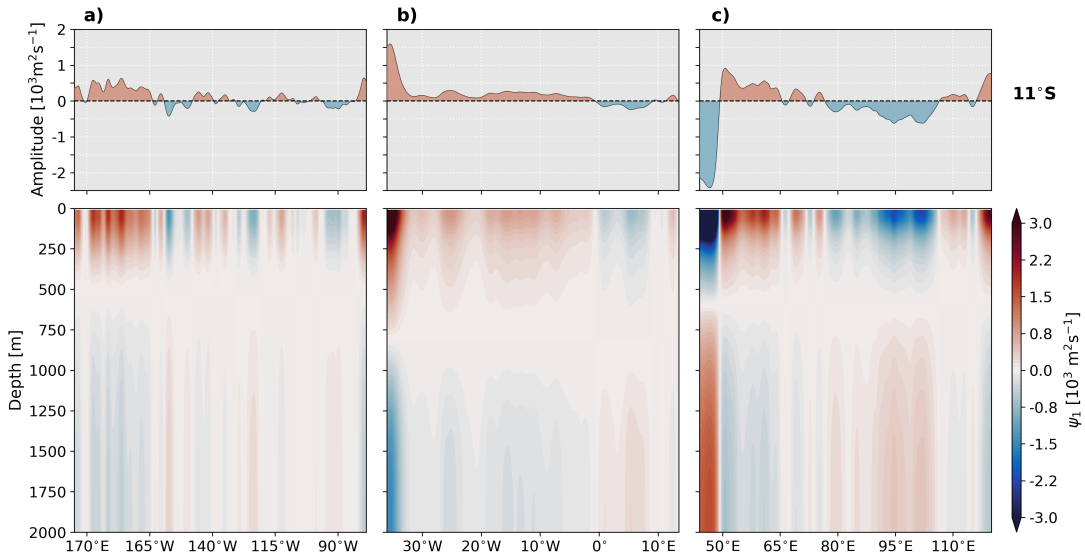

Figure 3.18: Mean first baroclinic modal amplitudes Ψ_1 (upper panels) and mean vertical first baroclinic mode streamfunction ψ_1 (lower panels) for (a) the Pacific, (b) Atlantic and (c) Indian basins at 11°S. Calculations were made using HYCOM's velocities and N^2 from T and S from ISAS climatology.

results of the previous latitude.

Interestingly, the modal amplitude $\overline{\Psi}_1$ is even larger in absolute values at 34.5°S. Contrary to 11°S and 24.5°S, the Pacific presented the smallest modal amplitudes among basins, ranging from -0.80 to 0.96 $\times 10^3$ m^{2}s^{-1} and the weakest first baroclinic mode streamfunction $\overline{\psi}_1$ (Figure 3.20-a). Likewise, this basin presented the weakest (51%) Rossby wave signal (Table 3.1) and the waves' with the smallest amplitudes (Table 3.3). The modal amplitude of the Atlantic fall between Indian and Pacific, ranging from -1.82 to 0.31 $\times 10^3$ m^{2}s^{-1}, and the first baroclinic mode streamfunction $\overline{\psi}_1$ is strongest in comparison to the Pacific Ocean (Figure 3.20-b), especially at the eastern part of both basins. As for the Indian Ocean, the modal amplitude $\overline{\Psi}_1$ is the largest in absolute values, between -1.86 and 0.70 $\times 10^3$ m^{2}s^{-1}. Similar to the previous latitudes, the Rossby waves detected in our altimeter analysis presented the largest amplitudes on this basin (Table 3.4), the exception being η_{12}. From these vertical analyses, it is proposed that the vertical velocity (u, v) profiles, used in the calculation of the modal amplitudes Ψ_i, have a significant part in modulating Rossby waves' amplitudes. These results can explain why the amplitudes of Rossby waves in the Atlantic Ocean are smaller than the same waves on the Pacific and Indian Oceans, especially at 11°S and 24.5°S, where differences in the water column stratification are remarkable.

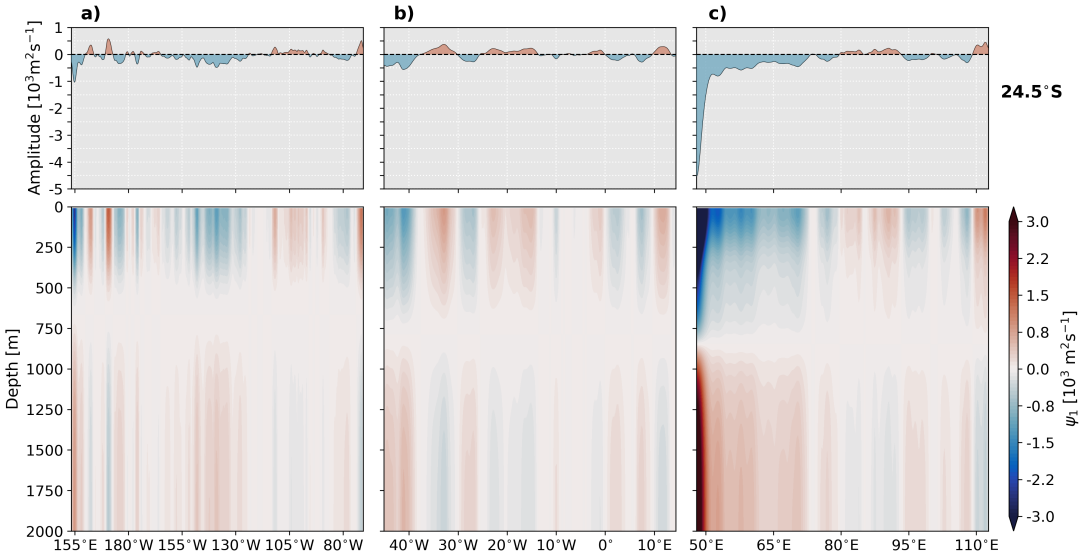

Figure 3.19: Similar to Figure 3.18 for 24.5°S.

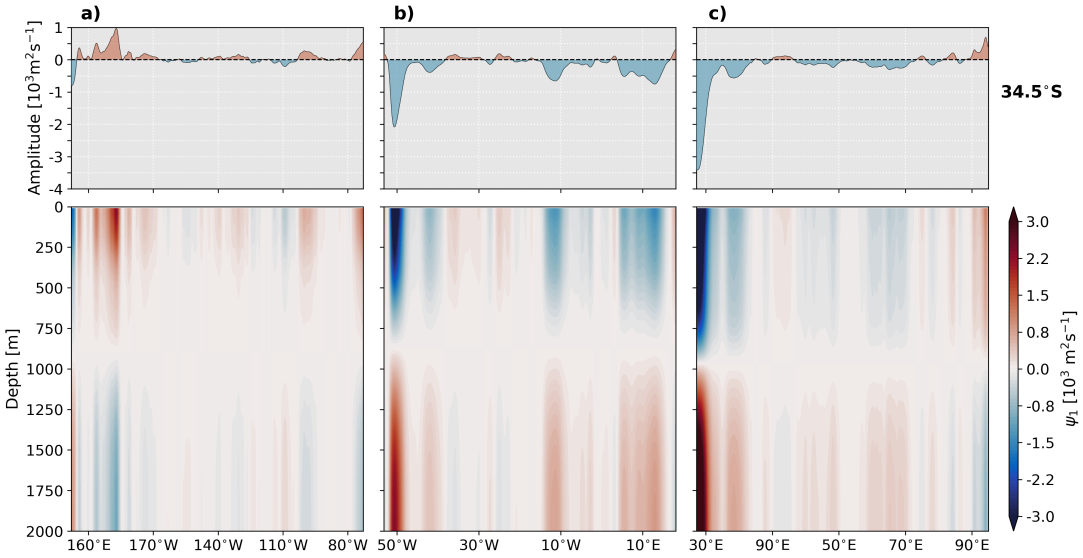

Figure 3.20: Similar to Figure 3.18 for 34.5°S.

The biggest differences between surface amplitudes of the waves among basins were observed at 11°S, and decreased poleward. This is consistent with our experiments, since we found variations in Rossby waves amplitudes both in the reconstructed Atlantic sea surface height anomaly (η_{rec}) with varying N^2(z) and F_i(z) profiles and in the comparison among basins of the reconstructed sea surface height anomaly (η_{rec}), and that was observed in Section 3.2.1 in our analysis using altimeter data. Variations in stratification are larger among basins close to the Equator (Figure 3.13-a); poleward, the water column becomes less stratified (Figure 3.13-b, c). Thus, based on our results, we can say that at least approximately half of the difference detected in long, first mode baroclinic Rossby waves amplitudes is due to a more stratified water column. However, the question that remains is: *What explains the rest of these amplitude differences?*

We therefore conclude that a more (less) stratified N^2 profile leads to larger (smaller) waves' amplitudes. Besides, from our interbasin comparison, the modal amplitudes derived from the vertical velocity profiles also influences waves amplitudes variations, and different vertical structures yields different waves' characteristics. Thus, stratification can modulate the Rossby waves' amplitudes and we accept hypothesis H_3. However, since the differences found between basins were not as high as in Section 3.2.1, and although we are comparing results from observational data and an ocean general circulation model, we suggest that this modulation is compounded by another or a variety of other processes, which may include wind stress curl variations and variations in PV down to the water column. To evaluate the wind influence, one could compare the wind stress parallel to the western boundary and its curl in the three ocean basins at the same band period as the waves; due to time constraints, this is beyond the scope of the present study. Nevertheless, this topic should be further investigated and present a potential theme for future investigation.

3.4 Summary and Conclusions

Long, first mode baroclinic Rossby waves generate perturbations in the pycnocline depth on the order of three times greater than at the surface, with the opposite phase (OLIVEIRA; POLITO, 2013). This means that a wave-like movement on the thermocline of around 20 m allied to a density variation of 3 kg m^{-3} can distort the ocean surface by about 6 cm. Thus, these features can be identified by altimetric radars because of its clear signal at the surface (POLITO; CORNILLON, 1997). Using several filters based

on convolution and sea level anomaly from Topex/Poseidon satellite altimeter, Polito and Liu (2003) identified Rossby waves globally. The authors found discrepancies between waves amplitudes, mainly on the Southern Hemisphere at the three ocean basins. Employing a similar method, we have identified Rossby waves at 11°S, 24.5°S and 34.5°S. By decomposing the sea level anomaly signal (η_0) in propagating and non-propagating signals, the latter including eddies and the basin-scale variability, we found that more than 86% of the sea surface height can be explained by the filtered components, which include the large-scale basin-wide signals, Rossby waves and the mesoscale eddy field.

From the filtered components of the sea surface height anomaly of the altimeter record, we estimated the explained variance of the Rossby wave field, defined by the sum of all westward propagating components. At 11°S, 41%, 63% and 69% (Table 3.1) of the total signal can be attributed to Rossby waves for the Atlantic, Pacific and Indian Oceans respectively. This result indicates that, from a radar altimeter perspective, long first-mode baroclinic Rossby waves are significantly more important for the Pacific and Indian Oceans when compared to the Atlantic. At 24.5°S, the explained variance of the Rossby wave field increases, 57% for the Atlantic, 73% for the Pacific and 75% for the Indian. As for 11°S, the waves in the Atlantic explain less variance than the other two basins, however, the overall amplitude more than doubled in most bands (Tables 3.2, 3.3, and 3.4), and the regional difference in the explained variance has decreased. This latitude marks, in all basins, the middle of the subtropical gyre. Here, the mean wind stress is below average, the mean wind stress curl (Figure 3.12-c) is positive and relatively large, with more variability than at 11°S. At 34.5°S, the Rossby wave field explains 61%, 51% and 67% of the sea surface surface height anomaly signal for the Atlantic, Pacific and Indian. This region is highly energetic (Figure 2.3), and the decrease in the explained variance of Rossby waves are due to an increase of mesoscale activity in this region. In most cases, the sea surface height is dominated by Rossby waves and we therefore accept hypothesis H_2. One important message that the sea surface height analysis shows here, is that, more often than not, the westward propagating planetary wave field has more energy than that of the seasonal cycle at 11°S, 24.5°S and 34.5°S. Thus, at least in these regions and for phenomena that can be studied in a 2 (or 1.5)-layer model, interior dynamics are more important to considerate than the seasonal cycle.

According to Chelton and Schlax (1996), Rossby waves detected by altimetry propagate faster that the predicted by the linear theory. However, Killworth *et al.* (1997) showed that the inclusion of a baroclinic east-west mean zonal flow works to increase the west-

ward propagation of the free, baroclinic Rossby waves. Therefore, our first questioning was whether these waves are, in fact, Doppler shifted as Killworth *et al.* (1997) proposes. We plotted the dispersion diagram (Figure 3.11) of the linear first baroclinic Rossby wave (dashed line). Long waves were close to the curve only at 11°S, departing from it with increasing latitude, suggesting that the simplest, non-Doppler shifted linear theory performs better close to low latitudes, which was also noted by Maharaj *et al.* (2007). Then, we included the mean background flow simply by estimating the mean zonal geostrophic velocity $\bar{u}_g$, defined as the temporal and spatial average of u_g from the altimeter obtained from each Hovmöller at each latitude, resulting in a much better fit for long waves (Figure 3.11, solid lines). Thus, including the background mean flow lead to a consistent approximation between our observations and the curves in our dispersion diagram. Our results suggest that the waves filtered are first-mode baroclinic, and the appearance of propagating faster is strongly related to the background movements, also corroborating Polito and Liu (2003) in agreement to the linear theory and Killworth *et al.* (1997) and Maharaj *et al.* (2007), given the influence of the mean flow. Another interesting conclusion concerns Rossby waves with smaller periods that depart from both the linear and Doppler-shifted curve (Figure 3.11), especially at 11°S. Assuming that the variability of the wind stress curl is low (Figure 3.12-d), and the influence of topography is not as significant as the influence of the background mean flow (KILLWORTH; BLUNDELL, 1999), we suggest that these waves are non-linear, so that the relationship between sea surface height and stratification would be weakened.

Long, first baroclinic mode Rossby waves have in the vertical stretching most of the vorticity that is changed to planetary in the process of oscillation and propagation. In a 2-layer model, this stretching translates into pycnocline height anomalies (Equation 1.7). The available potential energy of the wave depends on this anomaly squared weighted by the vertical stratification (CUSHMAN-ROISIN; BECKERS, 2012), and by mass conservation, the sea surface height anomaly will also be weighted by the vertical stratification. Thus, if a first-mode baroclinic Rossby wave in the Atlantic has the same available potential energy of a similar wave in the Pacific Ocean, but the stratification differs between basins, their signal on the ocean surface would differ. Due to all the contribution of density to surface and interior dynamics, we believed that stratification controls the amplitude of the Rossby waves' signals and explains most of the differences between the waves' amplitudes observed at the surface in mid-latitudes for the three basins on the South Hemisphere. From this simple, yet meaningful, idea, we decided to address our hypothesis with a more realistic stratification.

It is a common practice to decompose fields of a baroclinic flow in vertical modes, especially when most of the energy is attributed to few of them. The solution depends solely on the local N^2 profile, and each basin and latitude presented a different vertical structure (Figures 3.14, 3.18, 3.19, and 3.20). From our analysis using HYCOM-NCODA's vertical velocity profiles and N^2 derived from the ISAS climatology, 3 modes — the barotropic plus the first and the second baroclinic — suffice to reproduce the sea level anomaly field of the Atlantic, Pacific and Indian Oceans, representing more than 83% of the total surface variability. Furthermore, the observed differences in N^2 would result in different structures of baroclinic modes. Since our focus is on long, first-mode baroclinic Rossby waves, having different vertical configurations would, in principle, lead to variations the characteristics of the waves observed at the surface.

Satellite data are strict to the ocean surface, and projecting surface movements down to the water column is still a challenge. Therefore, we used velocity profiles from HYCOM-NCODA outputs and temperature and salinity profiles from ISAS to reconstruct the sea surface height, and relate these reconstructed fields to the ones obtained from the altimeter to assess hypothesis H_3. Two approaches were used to reconstruct the sea level anomaly field (η_{rec}) and identify the influence of stratification on Rossby waves. In the first experiment, we reconstructed Atlantic's sea level anomaly and applied the FIR2D to detect Rossby waves and their respective amplitudes. Then, using Atlantic's modal amplitude Ψ, we reconstructed two more sea level anomaly fields, the first one using N^2 and hence F from the Pacific and the second using N^2 and F from the Indian Oceans. Both reconstructed fields were filtered using the same method. We could identify differences in waves amplitudes on the Atlantic using different stratification profiles; however, these differences were not as large as the ones observed with the sea level anomaly provided by the altimeter (Section 3.2.1). The second experiment consisted in an interbasin comparison. The sea level anomaly was reconstructed for each basin and latitude and filtered to separate the propagating and non-propagating components; differences in amplitudes of the former were analyzed, and values were closer to the results obtained with the altimeter data.

In our first experiment, variations in the amplitudes of the waves in the Atlantic at 11°S ranged from -10% to 122%, negative values meaning smaller in amplitudes, when reconstructing η with Pacific and Indian stratification. Differences in amplitudes were larger when replacing the Atlantic with the Indian Ocean's N^2 profile, which is the most stratified at this location (Figure 3.13-a). However, replacing with the Pacific Ocean strat-

ification, amplitudes were almost unchanged ($\pm$ 10%). At 24.5°S, differences in waves' amplitudes were larger than the previous case. On average, the amplitudes were 90% (107%) larger when replacing Atlantic's N^2 for Pacific (Indian) Ocean's N^2 profiles. This result suggest that a more stratified water column, represented here by N^2 from the Pacific and Indian basins (Figure 3.13-b), leads to larger values of waves' amplitudes in comparison with those of the unaltered Atlantic. As for 34.5°S, from Section 3.2.1 we identified that Rossby waves amplitudes are similar, and the difference among basins is not as striking as at 11°S or 24.5°S. Since N^2 profiles at these latitudes are similar (Figure 3.13-c), we were not expecting much of a change. The results were indeed lower than the previous latitudes, ranging from -6% to 41%. However, using Pacific's stratification we were expecting that waves' amplitudes would be smaller than those of the unaltered Atlantic, as noted in Section 3.2.1, but η_6 was the only component that dropped its amplitude.

By choosing a realistic, climatological N^2 profile for the calculations of the vertical structure, we aimed for a physically consistent sea surface height anomaly reconstruction. Stratification differed among basins, and this difference is particularly more noticeable at 11°S and 24.5°S (Figure 3.13-a, b). We observed that, especially at 11°S and 24.5°S, where differences between wave amplitudes were large, the modal amplitudes calculated using vertical velocity profiles from HYCOM differed significantly, leading to a different vertical first-mode baroclinic streamfunction among basins (Figures 3.18 and 3.19). Our results allow us to state that this is why the Rossby wave amplitudes are smaller in the Atlantic in comparison to the same waves' amplitudes on the Pacific and Indian Oceans: they are associated to a less stratified water column, which results in a relatively weak vertical first-mode baroclinic structure. Therefore, we conclude that a more stratified water column leads to large wave amplitudes at the surface, but we cannot decouple the influence of the modal amplitudes.

In our second experiment, we performed an interbasin comparison, analyzing the amplitudes of the filtered waves for each reconstructed η. Results showed that differences in wave amplitudes were larger at 11°S, followed by 24.5°S, and 34.5°S. At 11°S and 24.5°S, differences were positive for the wave amplitudes for both the Pacific and Indian Oceans in comparison to the ones of the Atlantic, meaning that in the former oceans amplitudes are larger, exception being η_{24} at 24.5°S for the Pacific. At 34.5°S, differences were negative (positive) for the wave amplitudes of the Pacific (Indian) in comparison to the same components on the Atlantic, η_{12} for the Indian Ocean being the only exception. This is consistent to our analysis using the altimeter sea level anomaly data

(Section 3.2.1). Moreover, our sectional analysis showed that the Indian Ocean has the strongest first-mode baroclinic vertical structure (Figures 3.18-c and 3.19-c), and it is also the basin (i) with the strongest Rossby wave signal (Table 3.1) and (ii) with the waves with the largest amplitudes at 11°S and 24.5°S. At 34.5°S, not only stratification is very low, hardly reaching $1 \times 10^{-4}\,\mathrm{s}^{-1}$ (Figure 3.13-c), but also very similar among the three ocean basins. However, the average modal amplitudes of the first baroclinic mode ($\overline{\Psi}_1$) are very different, being the largest on the Indian, followed by the Atlantic and Pacific Oceans. In addition, the largest amplitudes of Rossby waves were detected at the Indian, followed again by the Atlantic and Pacific. More often than not, our interbasin comparison resulted in differences in wave amplitudes closer to the ones observed with the altimeter record. Our second experiment suggests that the vertical structure of the velocities also play an important role in modulating Rossby wave amplitudes.

In conclusion, our results suggest that a more (less) stratified water column, associated to each basin modal amplitudes Ψ, leads to an larger (smaller) wave amplitudes at the surface. It is worth mentioning that the modal amplitudes Ψ are calculated using not only the velocity vertical profiles, but also F, which is strongly dependent on stratification. Thus, we accept hypothesis H_3, that stratification modulates the amplitudes of mid-latitude, long, first-mode baroclinic Rossby waves. As a word of caution, we could not identify all the interbasin difference of Rossby wave amplitudes, and these changes are plausibly associated with (i) the presence of unstable currents, (ii) the use of exceedingly smooth, climatological profiles or simply (iii) our oversimplified physical model. Resolving this is beyond the scope of the present work, yet it poses an interesting framework for future studies.

4 *Final remarks*

The advent of satellites represented a huge advance not only in the oceanographic community but also in the private sector, spawning new enterprises, since 1978. From then on, many ocean processes that were poorly studied could be understood. In that, meso to large scale propagating signals pose a serious challenge to in-ship sampling due to the loss of synopticity during a data collection campaign. The two main advantages of the use of satellite data resides in global coverage and synopticity. Data is restricted to the ocean surface, so connecting the information at and below the surface seems to be an everlasting challenge. In a continuously stratified and geostrophic framework, horizontal density variations ensure the vertical shear of horizontal velocities. To include temporal variations, which are vital to the understanding of, for example, planetary waves, the quasi-geostrophy is brought into light. Because of altimeter's limitation of retrieving information below the surface, it is necessary to resort to primitive equations, general circulation models (OGCM) to study the four dimensional — x and y directions, depth and time — large-scale ocean circulation. The quasi-geostrophic models includes the minimum set of equations to have temporal variability and also keep approximations to a minimum, yet they suffice to reproduce the phenomenon in focus, although not realistically. To compare with observations, it is also needed that these OGCMs models assimilate observational data, such as the ones provided by satellites, moored buoys, and Argo floats, so that the variables would be physically consistent to the ones observed in the real ocean.

To correctly represent ocean circulation, these models should resolve Rossby waves (POLITO *et al.*, 2008). They are an important mechanism of adjustment in the ocean circulation and are directly related to climate, since they act to maintain western boundary currents, as they carry energy across basins. Thus, if a numerical model can accurately reproduce Rossby waves, it has a better chance of properly represent the physics of large scale ocean circulation. We chose to use HYCOM-NCODA precisely because it assimilates satellite data, correctly resolves Rossby waves (Appendix B) and makes available vertical profiles of the zonal and meridional velocities with enough resolution to fit our

purposes. In addition, we used temperature and salinity profiles provided by ISAS, because they are entirely based on *in situ* measurements.

In this context, this study focused on the role played by density fields in meso and large scale ocean dynamics. In Chapter 2, we have quantified to what extent the surface dynamics in the mesoscale band is driven by the time evolution of the density field at 11°S, 24.5°S and 34.5°S in the Atlantic ocean. For that, we derived the total streamfunction as a sum of the SQG and QG components (WANG *et al.*, 2013). According to Oliveira and Polito (2013), the explained variance of mesoscale eddies is larger that the one related to Rossby waves south of 25.5°S on the Atlantic. Southward to this latitude, the eddy kinetic energy increases near the western boundary. Close to the Brazil-Malvinas Confluence, to the west, and to the Agulhas leakage, to the east, energy reaches two regional maxima. We found that the SQG is the dominant factor of the sea surface height variability at these areas. In other words, we found SQG dominance mostly over highly energetic areas, associated to high mesoscale activity, and at our southernmost latitude (34.5°S), corroborating previous studies (LETRAON *et al.*, 2008; XU; FU, 2012; RICHMAN *et al.*, 2012; ROCHA *et al.*, 2013; GONZALEZ-HARO; ISERN-FONTANET, 2014; HOSODA *et al.*, 2015; DUFAU *et al.*, 2016). Moreover, we were able to identify that our SQG reconstruction dominates ψ during winter, when generally the ML is deeper, lateral buoyancy gradients are stronger and energy is higher (CALLIES *et al.*, 2015). This result clearly shows the our reconstruction depends on the seasonal variation of the MLD, in agreement to Isern-Fontanet *et al.* (2014), Gonzalez-Haro and Isern-Fontanet (2014), Vergara *et al.* (2019). In conclusion, we accept our hypothesis H_1.

In Chapter 3, we identified Rossby waves in the altimetric sea surface height anomaly fields at the same latitudes in the three ocean basins. We have concluded that most of the variability associated to westward propagating features are Rossby waves, explaining more than 41% of the variance of the total surface signal. Even south of 25.5°S, where mesoscale activity increases (Figure 2.3), the filters separate large-scale, long baroclinic Rossby waves (Figures 3.2–3.10) and mesoscale eddies, although they tend to propagate together (POLITO; SATO, 2015). From our analysis, Rossby waves explained 41% to 75% of the total sea surface height anomaly field on the three ocean basins. The dispersion diagram showed that not only the filter is portraying a statistically significant Rossby wave signal from the altimeter's sea level anomaly (Figure 3.11), but also that these waves are first-mode baroclinic and linear Doppler-shifted, especially the one with larger periods ($\sim$ 6 months). Therefore, hypothesis H_2 is confirmed.

Finally, we assessed the contribution of stratification to the modulation of waves' amplitudes. This stratification was given by realistic N^2 profiles calculated from temperature and salinity from the ISAS climatology. The sea surface height field was reconstructed under the QG theory considering the barotropic and the first two baroclinic modes, since they accounted for more than 83% of the surface field variance. From our results, we detected differences in waves' amplitudes (i) by maintaining Atlantic's modal amplitude (Ψ) and varying the vertical structure (F) to reconstruct the sea surface height anomaly field and (ii) by comparing the reconstructed sea surface height anomaly fields for the three ocean basins, using Ψ and F representative of each basin and latitude. We concluded that the more stratified the water column, the larger the waves' amplitudes at the surface. However, we cannot decouple F and Ψ. Through the exchange of density profiles of the Atlantic with those of basins, we confirmed the idea that the differences in stratification explain on average 45% of the disparity of Rossby wave amplitudes in a fixed latitude of the Atlantic Ocean in comparison with the amplitudes observed in other basins. Therefore, stratification is important but not a sufficient explanation. We accept hypothesis H_3 with this cautionary note. Through the modal reconstruction, in addition to the stratification that determines the vertical structure, we observed that the modal amplitude brings the reconstructed solution closer to the satellite observations. We interpret that as an indication that the partition of energy among vertical modes also plays an important role in modifying Rossby waves surface amplitudes.

Finally, the remaining amplitude differences that were not accounted in our hypothesis H_3 are probably due to our purposely naive and superficial approach to the wind forcing analysis. We propose that the proper solution to this problem is to use an ocean general circulation model with realistic and simulated wind stress curl scenarios, taking into account that most of the wind stress curl variability resides in the synoptic time scale. The part of the variability that affects oceanic Rossby waves most directly is (i) on the months to years time scale, and (ii) on a spatial scale of several Rossby radii. This is the part of the wind stress curl spectrum that should be modified for these hypothetical numerical experiments. Although very appealing, this enterprise is outside the scope of this study.

This study presented a dynamical interplay between surface and interior dynamics, connecting the surface expression of planetary waves to the interior stratification. It revealed interesting aspects of the physics of these waves. On a different perspective, it brought together data from orbital microwave altimeters, robotic quasi-Lagrangian floats

and numerical model reanalysis. It is by no means an end point, leaving many unopened doors. One of particular interest is the extension of this analysis towards finer scales, a possibility that will materialize with the launching of the Surface Water Ocean Topography–SWOT (MORROW *et al.*, 2019) and Winds and Currents Mission–WaCM (RODRIGUEZ *et al.*, 2019) missions in the near future. With high resolution altimetric measurements, we can extend this study towards smaller scale variability, although probably not as small as initially thought three years ago (CHELTON *et al.*, 2019). Another interesting possibility is to veer towards numerical model simulations of forced Rossby waves under different scenarios of wind stress curl variability and differential diabatic forcing, the latter effect usually ignored in the discussion of oceanic Rossby waves.

Bibliography

AGUEDJOU, H. M. A. *et al.* Eddies in the Tropical Atlantic Ocean and their seasonal variability. *Geophysical Research Letters*, v. 46, p. 12156–12164, 2019.

AMOL, P. Impact of Rossby waves on chlorophyll variability in the southeastern arabian sea. *Remote Sensing Letters*, v. 9:12, p. 1214–1223, 2018.

ANDERSON, D. L. T.; CORRY, R. A. Ocean response to low frequency wind forcing with application to the seasonal variation in the Florida Straits—Gulf Stream transport. *Progress in Oceanography*, Elsevier, v. 14, p. 7–40, 1985.

ANDERSON, D. L. T.; KILLWORTH, P. D. Non-linear propagation of long Rossby waves. *Deep-Sea Research*, v. 26A, p. 1033–1050, 1979.

AVISO/ALTIMETRY. AVISO User Handbook for Merged TOPEX/POSEIDON products. *AVI-NT-02-101*, p. 1–201, 1996.

BACKEBERG, B. C.; BERTINO, L.; JOHANNESSEN, J. A. Evaluating two numerical advection schemes in HYCOM for eddy-resolving modelling of the Agulhas Current. *Ocean Sciences*, Copernicus Publications on behalf of the European Geosciences Union, v. 5, p. 173–190, 2009.

BAKER-YEBOAH, S.; BYRNE, A.; WATTS, D. R. Observations of mesoscale eddies in the South Atlantic Cape Basin: Baroclinic and deep barotropic eddy variability. *Journal of Geophysical Research*, v. 115, n. C12069, p. 1–20, 2010.

BARNIER, B. A numerical study on the influence of the Mid-Atlantic Ridge on nonlinear first-mode baroclinic Rossby waves generated by seasonal winds. *Journal of physical oceanography*, v. 18, n. 3, p. 417–433, 1988.

BELONENKO, T. V.; BASHMACHNIKOV, I. L.; KUBRYAKOV, A. A. Horizontal advection of temperature and salinity by Rossby waves in the North Pacific. *International Journal of Remote Sensing*, v. 39, n. 8, p. 2177–2188, 2017.

BIROL, F.; MORROW, R. Source of the baroclinic waves in the southeast Indian Ocean. *Journal of Geophysical Research: Oceans*, Wiley Online Library, v. 106, n. C5, p. 9145–9160, 2001.

BOULANGER, J.-P.; MENKES, C. Propagation and reflection of long equatorial waves in the Pacific Ocean during the 1992-1993 El Niño. *Journal of Geophysical Research*, v. 100, n. C12, p. 25041–25059, 1995.

BOYER-MONTÉGUT, C. de *et al.* Mixed layer depth over the global ocean: An examination of profile data and a profile-based climatology. *Journal of Geophysical Research: Oceans*, Wiley Online Library, v. 109, n. C12, 2004.

BOYER, T. P.; LEVITUS, S. *Quality control and processing of historical oceanographic temperature, salinity, and oxygen data*. [S.l.]: US Department of Commerce, National Oceanic and Atmospheric Administration, 1994.

CALLIES, J. *et al.* Seasonality in submesoscale turbulence. *Nature communications*, Nature Publishing Group, v. 6, n. 1, p. 1–8, 2015.

CASTELLANOS, P. *et al.* Inter-comparison studies between high-resolution HYCOM simulation and observational data: The South Atlantic and the Agulhas leakage system. *Journal of marine systems*, Elsevier, v. 159, p. 76–88, 2016.

CAZENAVE, A.; LLOVEL, W. Contemporary sea level rise. *Annual review of Marine Science*, Annual Reviews, v. 2, p. 145–173, 2010.

CHELTON, B. D.; SZOEKE, R. A. de; SCHLAX, M. G. Global atlas of first baroclinic Rossby radius of deformation and gravity-wave phase speed. *Oregon State University, Oregon*, 2008.

CHELTON, D. B. *et al.* Geographical variability of the first baroclinic Rossby radius of deformation. *Science*, v. 28, p. 433–460, 1998.

CHELTON, D. B.; SCHLAX, M. G. Global observations of oceanic Rossby waves. *Science*, v. 272, p. 234–238, 1996.

CHELTON, D. B. *et al.* Global observations of large oceanic eddies. *Geophysical Research Letters*, v. 34, n. L15606, p. 1–5, 2007.

CHELTON, D. B. *et al.* Prospects for future satellite estimation of small-scale variability of ocean surface velocity and vorticity. *Progress in Oceanography*, Elsevier, v. 173, p. 256–350, 2019.

CHEN, G.; HAN, G. Contrasting short-lived with long-lived mesoscale eddies in the global ocean. *Journal of Geophysical Research: Oceans*, Wiley Online Library, v. 124, n. 5, p. 3149–3167, 2019.

CHU, P. C. *et al.* On long baroclinic Rossby waves in the tropical North Atlantic observed from profiling floats. *Journal of Geophysical Research: Oceans*, Wiley Online Library, v. 112, n. C5, 2007.

CHURCH, J. A. *et al.* Estimates of the regional distribution of sea level rise over the 1950–2000 period. *Journal of Climate*, v. 17, n. 13, p. 2609–2625, 2004.

CIPOLLINI, P. *et al.* Rossby waves detected in global ocean colour data. *Geophysical Research Letters*, Wiley Online Library, v. 28, n. 2, p. 323–326, 2001.

CIPOLLINI, P.; CROMWELL, D.; QUARTLY, G. D. Observations of Rossby wave propagation in the Northeast Atlantic with TOPEX/Poseidon altimetry. *Advances in Space Research*, v. 22, p. 1553–1556, 1998.

CIPOLLINI, P. *et al. Satellites, Oceanography and Society*. [S.l.]: Elsevier Science, 2000. 99–125 p.

COX, M. D. Generation and propagation of 30-day waves in a numerical model of the pacific. *Journal of Physical Oceanography*, v. 10, n. 8, p. 1168–1186, 1980.

CUMMINGS, J. A. *Status and Progress of NCODA Assimilation in HYCOM*. [S.l.], 2007.

CUSHMAN-ROISIN, B.; BECKERS, J. *Introduction to Geophysical Fluid Dynamics: physical and numerical aspects*. Second edition. [S.l.]: Elsevier, 2011. 813 p. p.

CUSHMAN-ROISIN, B.; BECKERS, J.-M. *Introduction to Geophysical Fluid Dynamics: Physical and Numerical Aspects*. [S.l.]: Academic Press, 2012. 768 p. p.

DEE, D. P. *et al.* The ERA-Interim reanalysis: Configuration and performance of the data assimilation system. *Quarterly Journal of the royal meteorological society*, Wiley Online Library, v. 137, n. 656, p. 553–597, 2011.

DEWAR, W. K.; MORRIS, M. Y. On the propagation of baroclinic waves in the general circulation. *Journal of Physical Oceanography*, v. 30, p. 2637–2649, 2000.

DÖÖS, K. Influence of the Rossby waves on the seasonal cycle in the tropical atlantic. *Journal of Geophysical Research*, v. 114, n. C12, p. 29591–29598, 1999.

DUFAU, C. *et al.* Mesoscale resolution capability of altimetry: Present and future. *Journal of Geophysical Research: Oceans*, v. 121, p. 4910–4927, 2016.

FERRARI, R.; WUNSCH, C. The distribution of eddy kinetic and potential energies in the global ocean. *Tellus A: Dynamic Meteorology and Oceanography*, v. 62, n. 2, p. 92–108, 2010.

FLIERL, G. R. Models of vertical structure and the calibration of two-layer models. *Dynamics of Atmospheres and Oceans*, v. 2, p. 341–381, 1978.

FRANKIGNOUL, C.; MÜLLER, P. On the generation of geostrophic eddies by surface buoyancy flux anomalies. *Journal of Physical Oceanography*, v. 9, n. 6, p. 1207–1213, 1979.

FU, L.-L.; CHELTON, D. B. Large-Scale Ocean Circulation. In: ____. *Satellite Altimetry and Earth Sciences: A Handbook of Techniques and Applications*. First. [S.l.: s.n.], 2000. v. 29, p. 463.

FU, L.-L. *et al.* Topex/poseidon mission overview. *Journal of Geophysical Research*, v. 99, n. C12, p. 24369–24381, 1994.

FU, L.-L.; QIU, B. Low-frequency variability of the North Pacific Ocean: The roles of boundary- and wind-driven baroclinic Rossby waves. *Journal of Geophysical Research*, v. 107, n. C12, p. 13–1–13–10, 2002.

GAILLARD, F. Isas - tool version 6: Method and configuration. *Rapport LPO 12–02*, p. 1–18, 2012.

GARZOLI, S.; SIMIONATO, C. Baroclinic instabilities and forced oscillations in the Brazil/Malvinas confluence front. *Deep Sea Research*, v. 37, n. 6, p. 1053–1074, 1990.

GARZOLI, S. L.; GORDON, A. L. Origins and variability of the Benguela Current. *Journal of Geophysical Research*, v. 101, n. C1, p. 897–906, 1996.

GASPAR, P.; WUNSCH, C. Estimates from altimeter data of Barotropic Rossby waves in the Northwestern Atlantic Ocean. *Journal of Physical Oceanography*, v. 19, n. 12, p. 1821–1844, 1989.

GILL, A. E. *Atmosphere-Ocean Dynamics*. [S.l.]: International Geophysics Series, 1982. 661 p. p.

GONZALEZ-HARO, C.; ISERN-FONTANET, J. Global ocean current reconstruction from altimetric and microwave sst measurements. *Journal of Geophysical Research: Oceans*, v. 119, p. 3378–3391, 2014.

GORDON, A. L.; BOSLEY, K. T. Cyclonic gyre in the tropical South Atlantic. *Deep-Sea Research*, v. 38, n. 1, p. S323–S343, 1990.

GORDON, A. L.; GREENGROVE, C. L. Geostrophic circulation of the Brazil-Falkland confluence. *Deep-Sea Research*, v. 33, n. 5, p. 573–585, 1986.

GUERRA, L. A.; PAIVA, A. M.; CHASSIGNET, E. P. On the translation of Agulhas rings to the western South Atlantic Ocean. *Deep Sea Research Part I: Oceanographic Research Papers*, Elsevier, v. 139, p. 104–113, 2018.

HAN, Y.-J.; LEE, S.-W. An analysis of monthly mean wind stress over the global ocean. *Monthly Weather Review*, v. 111, p. 1554–1566, 1985.

HELD, I. M. *et al.* Surface quasi-geostrophic dynamics. *Journal of Fluid Mechanics*, v. 282, p. 1–20, 1995.

HERRMANN, P.; KRAUSS, W. Generation and propagation of annual Rossby waves in the North Atlantic. *Journal of physical oceanography*, v. 19, n. 6, p. 727–744, 1989.

HILL, K. L.; ROBINSON, I. S.; CIPOLLINI, P. Propagation characteristics of extratropical planetary waves observed in the atsr global sea surface temperature record. *Journal of Geophysical Research: Oceans*, Wiley Online Library, v. 105, n. C9, p. 21927–21945, 2000.

HOSKINS, B. J.; MCINTYRE, M. E.; ROBERTSON, A. W. On the use and significance of isentropic potential vorticity maps. *Quarterly Journal of the Royal Meteorological Society*, Wiley Online Library, v. 111, n. 470, p. 877–946, 1985.

HOSODA, K.; KAWAMURA, H.; SAKAIDA, F. Improvement of New Generation Sea Surface Temperature for Open ocean (ngsst-0): a new sub-sampling method of blending microwave observations. *Journal of Oceanography*, v. 71, p. 205–220, 2015.

HOURY, S. *et al.* Brunt-Väisälä frequency and Rossby radii in the south atlantic. *Journal of Physical Oceanography*, v. 17, p. 1619–1626, 1987.

ISERN-FONTANET, J. *et al.* Potential use of microwave sea surface temperatures for the estimation of ocean currents. *Geophysical Research Letters*, v. 33, n. L24608, p. 1–5, 2006.

ISERN-FONTANET, J. *et al.* Three-dimensional reconstruction of oceanic mesoscale currents from surface information. *Journal of Geophysical Research*, v. 113, n. C09005, p. 1–17, 2008.

ISERN-FONTANET, J.; SHINDE, M.; GONZáLEZ-HARO, C. On the transfer function between surface fields and the geostrophic stream function in the mediterranean sea. *Journal of Physical Oceanography*, v. 44, p. 1406–1423, 2014.

JACOBS, G. A. *et al.* The global structure of the annual and semiannual sea surface height variability from geosat altimeter data. *Journal of Geophysical Research: Oceans*, Wiley Online Library, v. 97, n. C11, p. 17813–17828, 1992.

JACOBS, G. A.; EMERY, W. J.; BORN, G. H. Rossby waves in the Pacific Ocean extracted from Geosat altimeter data. *Journal of Physical Oceanography*, v. 23, p. 1155–1175, 1993.

KANG, Y. Q.; MAGAARD, L. Annual baroclinic Rossby waves in the Central North Pacific. *Journal of Physical Oceanography*, v. 10, p. 1159–1167, 1980.

KESSLER, W. S. Observations of long Rossby waves in the northern tropical pacific. *Journal of Geophysical Research*, v. 95, n. C4, p. 5183–5217, 1990.

KILLWORTH, P. D.; BLUNDELL, J. R. The effect of bottom topography on the speed of long extratropical planetary waves. *Journal of Physical Oceanography*, v. 29, p. 2689–2710, 1999.

KILLWORTH, P. D.; BLUNDELL, J. R. Long extratropical planetary wave propagation in the presence of slowly varying mean flow and bottom topography. part i: The local problem. *Journal of Physical Oceanography*, v. 33, p. 784–801, 2003.

KILLWORTH, P. D.; BLUNDELL, J. R. Planetary wave response to surface forcing and instability in the presence of mean flow and topography. *Journal of physical oceanography*, v. 37, n. 5, p. 1297–1320, 2007.

KILLWORTH, P. D.; CHELTON, D. B.; SZOEKE, R. A. D. The speed of observed and theoretical long extratropical planetary waves. *Journal of Physical Oceanography*, v. 27, p. 1946–1966, 1997.

KUNDU, P. K.; ALLEN, J. S.; SMITH, R. L. Modal decomposition of the velocity field near the Oregon Coast. *Journal of Physical Oceanography*, v. 5, p. 683–704, 1975.

KUNDU, P. K.; COHEN, I. M. *Fluid Mechanics*. Second edition. [S.l.]: Academic Press, 2002. 730 p. p.

LACASCE, J. H. Surface quasigeostrophic solutions and baroclinic modes with exponential stratification. *Journal of Physical Oceanography*, v. 42, p. 569–580, 2012.

LACASCE, J. H. The prevalence of oceanic surface modes. *Geophysical Research Letters*, v. 44, p. 11097–11105, 2017.

LACASCE, J. H.; MAHADEVAN, A. Estimating subsurface horizontal and vertical velocities from sea-surface temperature. *Journal of Marine Research*, v. 64, p. 695–721, 2006.

LACASCE, J. H.; WANG, J. Estimating subsurface velocities from surface fields with idealized stratification. *Journal of Physical Oceanography*, v. 45, p. 2424–2435, 2015.

LAPEYRE, G. What vertical mode does the altimeter reflect? on the decomposition in baroclinic modes and on a surface-trapped mode. *Journal of Physical Oceanography*, v. 39, p. 2857–2874, 2009.

LAPEYRE, G.; KLEIN, P. Dynamics of the upper oceanic layers in terms of surface quasigeostrophy theory. *Journal of Physical Oceanography*, v. 36, p. 165–176, 2006.

LEBLOND, P. H.; MYSAK, L. A. *Waves in the Ocean*. First edition. [S.l.]: Elsevier Oceanographic Series, 1978. 602 p. p.

LEE, T. *et al.* Evaluation of cmip3 and cmip5 wind stress climatology using satellite measurements and atmospheric reanalysis products. *Journal of Climate*, v. 26, p. 5810–5826, 2013.

LETRAON, P. Y. *et al.* Do altimeter wavenumber spectra agree with the interior or surface quasigeostrophic theory? *Journal of Physical Oceanography*, v. 38, p. 1137–1142, 2008.

LEVITUS, S. *Climatological atlas of the world ocean*. [S.l.]: US Department of Commerce, National Oceanic and Atmospheric Administration, 1982. 173 p.

LI, X. *et al.* Atlantic-induced pan-tropical climate change over the past three decades. *Nature Climate Change*, Nature Publishing Group, v. 6, n. 3, p. 275–279, 2016.

LIM, J. S. Two-dimensional signal and image processing. *ph*, 1990.

LIPPERT, A.; KÄSE, R. H. Stochastic wind forcing of baroclinic Rossby waves in the presence of a meridional boundary. *Journal of physical oceanography*, v. 15, n. 2, p. 184–194, 1985.

LIU, L. *et al.* Retrieving density and velocity fields of the ocean's interior from surface data. *Journal of Geophysical Research: Oceans*, v. 119, p. 8512–8529, 2014.

LIU, Z. Forced planetary wave response in a thermocline Gyre. *Journal of Physical Oceanography*, v. 29, p. 1036–1055, 1999.

MAHARAJ, A. M. *et al.* An evaluation of the classical and extended Rossby wave theories in explaining spectral estimates of the first few baroclinic modes in the South Pacific Ocean. *Ocean Dynamics*, v. 57, p. 173–187, 2007.

MCWILLIAMS, J. C. *Fundamentals of Geophysical Fluid Dynamics*. [S.l.]: Cambridge University Press, 2006. 249 p. p.

MCWILLIAMS, J. C. *et al. The Local Dynamics of Eddies in the Western North Atlantic*. [S.l.]: Springer, Berlin, Heidelberg, 1983. 92–113 p.

MEINEN, C. S. *et al.* Characteristics and causes of Deep Western Boundary Current transport variability at 34.5°s during 2009–2014. *Ocean Science*, v. 13, p. 175–194, 2017.

MEINEN, C. S. *et al.* Temporal variability of the meridional overturning circulation at 34.5°s: Results from two pilot boundary arrays in the South Atlantic. *Journal of Geophysical Research*, v. 118, p. 6461–6478, 2013.

MILLIFF, R. F.; MORZEL, J. The global distribution of the time-average wind stress curl from nscat. *Journal of Atmospheric Sciences*, v. 58, n. 2, p. 109–131, 2001.

MORROW, R. *et al.* Global observations of fine-scale ocean surface topography with the Surface Water and Ocean Topography (swot) Mission. *Frontier in Marine Sciences*, v. 6, n. 232, p. 1–19, 2019.

MÜLLER, P.; FRANKIGNOUL, C. Direct atmospheric forcing of geostrophic eddies. *Journal of Physical Oceanography*, v. 11, n. 3, p. 287–308, 1981.

NAPOLITANO, D. C. *et al.* On the steadiness and instability of the Intermediate Western Boundary Current between 24° and 18°s. *Journal of Physical Oceanography*, v. 49, p. 3127–3143, 2019.

OLBERS, D.; WILLEBRAND, J.; EDEN, C. *Ocean Dynamics*. [S.l.]: Springer, 2012. 704 p. p.

OLIVEIRA, F. S. C.; POLITO, P. S. Characterization of westward propagating signals in the South Atlantic from altimeter and radiometer records. *Remote Sensing Environment*, v. 134, p. 367–376, 2013.

OSYCHNY, V.; CORNILLON, P. Properties of Rossby waves in the North Atlantic estimated from satellite data. *Journal of Physical Oceanography*, v. 34, p. 61–76, 2004.

PEDLOSKY, J. A note on the western intensification of the ocean circulation. *Journal of Marine Research*, v. 23, n. 3, p. 207–209, 1965.

PEDLOSKY, J. On the radiation of mesoscale energy in the midocean. *Deep-Sea Research*, v. 24, p. 591–600, 1977.

PEDLOSKY, J. *Geophysical Fluid Dynamics*. [S.l.]: Springer, 1987. 710 p. p.

PEDLOSKY, J. *Waves in the Ocean and Atmosphere: Introduction of Wave Dynamics*. [S.l.]: Springer, 2003. 260 p. p.

PEGLIASCO C., A. C.; MORROW, R. Main eddy vertical structures observed in the four major eastern boundary upwelling systems. *Journal of Geophysical Research: Oceans*, v. 120, p. 6008–6033, 2015.

PETERSON, R. G.; STRAMMA, L. Upper-level circulation in the South Atlantic Ocean. *Progress in Oceanography*, v. 26, p. 1–73, 1991.

POLITO, P. S.; CORNILLON, P. Long baroclinic Rossby waves detected by topex/poseidon. *Journal of Geophysical Research*, v. 102, p. 3215–3235, 1997.

POLITO, P. S.; LIU, W. T. Global characterization of Rossby waves at several spectral bands. *Journal of Geophysical Research*, v. 108, n. C1, p. 1–18, 2003.

POLITO, P. S.; SATO, O. T. Do eddies ride on Rossby waves? *Journal of Geophysical Research*, v. 120, p. 5417–5435, 2015.

POLITO, P. S.; SATO, O. T.; LIU, W. T. Characterization and validation of the heat storage variability from TOPEX/Poseidon at four oceanographic sites. *Journal of Geophysical Research*, v. 105, n. C7, p. 16911–16921, 2000.

POLITO, P. S.; SATO, O. T.; WAINER, I. Height variability from the MIROC–IPCC model for the 20th century compared to that of the TOPEX/POSEIDON altimeter. *Ocean Modelling*, Elsevier, v. 24, n. 3-4, p. 73–91, 2008.

PONTE, A. L.; KLEIN, P. Reconstruction of the upper ocean 3D dynamics from high-resolution sea surface height. *Ocean Dynamics*, v. 63, p. 777–791, 2013.

RHINES, P. Edge-, bottom-, and and Rossby waves in a rotating stratified fluid. *Geophysical and Astrophysical Fluid Dynamics*, v. 1, p. 273–302, 1970.

RICHMAN, J. G. *et al.* Inferring dynamics from the wavenumber spectra of an eddying global ocean model with embedded tides. *Journal of Geophysical Research*, v. 117, n. C12012, p. 1–11, 2012.

RICHMAN, J. G.; WUNSCH, C.; HOGG, N. G. Space and time scales of mesoscale motion in the western North Atlantic. *Reviews of Geophysics and Space Physics*, v. 15, n. 4, p. 1–11, 1977.

RISIEN, C. M.; CHELTON, D. B. A global climatology of surface wind and wind stress fields from eight years of QuikSCAT Scatterometer data. *Journal of Physical Oceanography*, v. 38, p. 2379–2413, 2008.

ROBINSON, I. S. *Satellite Oceanography*. First edition. [S.l.]: Wiley, 1995. 456 p. p.

ROBINSON, I. S. *Measuring the Ocean from Space: The principles and methods of satellite oceanography*. First edition. [S.l.]: Springer, 2004. 669 p. p.

ROBINSON, I. S. *Discovering the ocean from space: The unique applications of satellite oceanography*. First edition. [S.l.]: Springer, 2010. 638 p. p.

ROCHA, C. B. *et al.* Mesoscale to submesoscale wavenumber spectra in Drake Passage. *Journal of Physical Oceanography*, v. 46, p. 601–620, 2016.

ROCHA, C. B. *et al.* Traditional quasi-geostrophic modes and surface quasi-geostrophic solutions in the Southwestern Atlantic. *Journal of Geophysical Research: Oceans*, v. 118, p. 2734–2745, 2013.

RODEN, G. I. Thermohaline fronts and baroclinic flow in the Argentine Basin during the austral spring of 1984. *Journal of Geophysical Research*, v. 91, n. C4, p. 5075–5093, 1986.

RODRIGUEZ, E. *et al.* The winds and currents mission concept. *Frontiers in Marine Science*, Frontiers, v. 6, p. 438, 2019.

SALMON, R. *Lectures on Geophysical Fluid Dynamics*. [S.l.]: Oxford University Press, 1998. 50–120 p.

SASAKI, H. *et al.* Impact of oceanic-scale interactions on the seasonal modulation of ocean dynamics by the atmosphere. *Nature: Communications*, v. 5, n. 5636, p. 1–8, 2014.

SILVEIRA, I. C. A. da; BROWN, W. S. Dynamics of the North Brazil Current retroflection region from the western Tropical Atlantic Experiment observations. *Journal of Geophysical Research*, v. 105, n. C12, p. 28559–28583, 2000.

SILVEIRA, I. C. A. da; MIRANDA, L. B. de; BROWN, W. S. On the origins of the North Brazil Current. *Journal of Geophysical Research*, v. 99, n. C11, p. 22501–22512, 1994.

SMITH, K. S.; VALLIS, G. K. The scales and equilibration of midocean eddies: Freely evolving flow. *Journal of Physical Oceanography*, v. 31, p. 554–571, 2001.

STAMMER, D. Global characteristics of ocean variability estimated from regional TOPEX/ POSEIDON Altimeter measurements. *Journal of Physical Oceanography*, v. 27, p. 1743–1769, 1997.

SUDHEER, J.; RAVICHANDRAN, M. Validation of 0.25 x 0.25 Indian Ocean HYCOM. INCOIS, 2012.

SUDRE, J.; MAES, C.; GARCON, V. On the global estimates of geostrophic and Ekman surface currents. *Limnology and Oceanography: Fluids and Environments*, v. 3, p. 1–20, 2013.

TAILLEUX, R.; MCWILLIAMS, J. C. The effect of bottom pressure decoupling on the speed of extratropical, baroclinic Rossby waves. *Journal of physical oceanography*, v. 31, n. 6, p. 1461–1476, 2001.

TALLEY, L. D. *et al. Descriptive Physical Oceanography: An Introduction*. Sixth edition. [S.l.]: Elsevier, 2011.

TANDON, A.; GARRETT, C. Geostrophic adjustment and restratification of a mixed layer with horizontal gradients above a stratified layer. *Journal of physical oceanography*, v. 25, n. 10, p. 2229–2241, 1995.

TCHILIBOU, M. *et al.* Spectral signatures of the Tropical Pacific dynamics from model and altimetry: a focus on the meso-/submesoscale range. *Ocean Sciences*, v. 14, p. 1283–1301, 2018.

THOMPSON, L. *et al.* Buoyancy and Mixed Layer effects on the sea surface height response in an isopycnal model of the North Pacific. *Journal of Physical Oceanography*, v. 32, p. 3657–3670, 2002.

VALLIS, G. K. *Atmospheric and Oceanic Fluid Dynamics: Fundamentals and Large Scale-circulation*. [S.l.]: Cambridge University Press, 2006. 197–244 p.

VERGARA, O. *et al.* Revised global wave number spectra from recent altimeter observations. *Journal of Geophysical Research: Oceans*, v. 124, p. 3523–3537, 2019.

VIVIER, F.; KELLY, K. A.; THOMPSON, L. Contributions of wind forcing, waves, and surface heating to sea surface height observations in the Pacific Ocean. *Journal of Geophysical Research: Oceans*, Wiley Online Library, v. 104, n. C9, p. 20767–20788, 1999.

WANG, D. *et al.* Wavenumber spectrum in the Gulf Stream from shipboard ADCP observations and comparison with altimetry measurements. *Journal of Physical Oceanography*, v. 40, p. 840–844, 2010.

WANG, J. *et al.* Reconstructing the ocean's interior from surface data. *Journal of Physical Oceanography*, v. 43, p. 1611–1626, 2013.

WANG, L. *et al.* Large-scale Rossby wave in the mid-latitude South Pacific from altimetry data. *Geophysical Research Letters*, v. 25, n. 2, p. 179–182, 1998.

WATANABE, W. B.; POLITO, P. S.; SILVEIRA, I. C. Can a minimalist model of wind forced baroclinic Rossby waves produce reasonable results? *Ocean Dynamics*, v. 66, p. 539–548, 2016.

WUNSCH, C. The vertical partition of oceanic horizontal kinetic energy. *Journal of Physical Oceanography*, v. 27, p. 1770–1794, 1997.

WUNSCH, C.; STAMMER, D. The global frequency-wavenumber spectrum of oceanic variability estimated from TOPEX/Poseidon altimeter measurements. *Journal of Geophysical Research*, v. 100, p. 24 895–24 910, 1995.

WYRTKI K., L. M.; HAGER, J. Eddy energy in the oceans. *Journal of Geophysical Research*, v. 81, n. 15, p. 2641–2646, 1976.

XU, Y.; FU, L. The effects of altimeter instrument noise on the estimation of the wavenumber spectrum of sea surface height. *Journal of Physical Oceanography*, v. 42, p. 2229–2233, 2012.

YANG, H. Evolution of long planetary wave packets in a continuously stratified ocean. *Journal of physical oceanography*, v. 30, n. 8, p. 2111–2123, 2000.

ZANG, X.; WUNSCH, C. The observed dispersion relationship for North Pacific Rossby wave motions. *Journal of Physical Oceanography*, v. 29, p. 2183–2190, 1999.

APPENDIX A – Theory behind QG modes and SQG solutions

A.1 Traditional modes — QG theory

This part of the Appendix complements the theory presented in Section 2.2. There we suppressed the mathematics to improve readability, and for the sake of completeness we present this part here. We introduce the quasi-geostrophic conservation of potential vorticity (QGPV) equation:

$$\frac{D_g}{Dt}q = 0, \tag{A.1}$$

where q is:

$$q = \nabla^2\psi + \beta y + \frac{\partial}{\partial z}\left(\frac{f_0^2}{N^2}\frac{\partial \psi}{\partial z}\right).$$

Linearizing equation A.1, we obtain:

$$\frac{\partial}{\partial t}\left[\nabla^2\psi + \frac{\partial}{\partial z}\left(\frac{f_0^2}{N^2}\frac{\partial \psi}{\partial z}\right)\right] + \beta\frac{\partial \psi}{\partial x} = 0, \tag{A.2}$$

solved by separation of variables

$$\psi(x,y,z,t) = \Psi(x,y,t)F(z)\,. \tag{A.3}$$

Equation A.2 admits wave-like solutions, being F the vertical structure and Ψ the stream-function modal amplitude, $\Psi(x,y,t) = e^{i(k_x x + k_y y - \omega t)}$.

Proceeding with the separation of variables technique, we group the terms that depend on (x,y,t) on the left side and the ones dependent on (z) on the right side. Thus,

$$-\frac{1}{\frac{\partial \Psi_i}{\partial t}}\left(\frac{\partial}{\partial t}\nabla^2\Psi_i + \beta\frac{\partial \Psi_i}{\partial x}\right) = \frac{1}{F_i}\left(\frac{\partial}{\partial z}\frac{f_0^2}{N^2}\frac{\partial F_i}{\partial z}\right) = -\lambda_i^2\,, \tag{A.4}$$

where $i = [0,1,2,3,...+\infty[$, F_i are the eigenvectors and λ_i^2 are the eigenvalues.

The boundary conditions at the surface (z = 0) and at the bottom (z = -H) are:

$$\frac{\partial F_i}{\partial z} = 0\,. \tag{A.5}$$

Equations A.4 – A.5 form a Sturm-Liouville eigenvalue problem. The right side of Equation A.4 represents the horizontal-temporal evolution equation, and the left side, that is,

$$\left(\frac{\partial}{\partial z}\frac{f_0^2}{N^2}\frac{\partial F_i}{\partial z}\right) = -\lambda_i^2 F_i\,, \tag{A.6}$$

is the vertical structure equation. The vertical modes F_i are discrete functions in a discrete layered model, and continuous in continuous height coordinates (MCWILLIAMS, 2006),

$$\psi(x,y,z,t) = \sum_{i=0}^{\infty} \Psi_i(x,y,t)\, F_i(z)\,. \tag{A.7}$$

To obtain the numerical solution of Equation A.6 and obtain the vertical structure F_i(z) for each mode, following McWilliams (2006), can be expressed in matrix notation for an arbitrary M layers, q and ψ can be written as:

$$\begin{cases} q = q_m;\ m = 1,...,M \\ \psi = \psi_m;\ m = 1,...,M\,. \end{cases} \tag{A.8}$$

The q and ψ are related to the layered potential vorticities, a vertical discretization in layers for the QGPV 3D:

$$\begin{cases} q_1 = \nabla^2\psi_1 + \beta y - \frac{f_0^2}{g'_{1.5}H_1}(\psi_1 - \psi_2)\,, \\ q_m = \nabla^2\psi_m + \beta y - \frac{f_0^2}{g'_{m+0.5}H_n}(\psi_m - \psi_{m+1}) + \frac{f_0^2}{g'_{n-0.5}H_m}(\psi_{m-1} - \psi_m)\,, \\ q_M = \nabla^2\psi_M + \beta y - \frac{f_0^2}{g'_{M-0.5}H_M}(\psi_{M-1} - \psi_M)\,, \end{cases} \tag{A.9}$$

and expressed in matrix notation:

$$q = P\psi + I\beta\, y\,,$$

where I is the identity matrix (= 1 for each diagonal element) and P is the linear operator which represents the contribution of ψ derivatives to $q - I\beta y$, that is,

$$P = I\nabla^2 - S\,,$$

where $I\nabla^2$ is the relative vorticity and S the stretching vorticity operators, in matrix notation.

The modal transformations are expressed in matrix notation $psi = F\Psi$, $\Psi = F^{-1}\psi$, and thus,

$$q = F^{-1}PF\Psi + I\beta y = [I\nabla^2 - F^{-1}S]\Psi + I\beta\, y\,.$$

To eliminate cross-modal coupling, $F^{-1}SF$ is a diagonal matrix, i.e., choosing the vertical modes F as eigenmodes of S with the correspondent eigenvalues $R_m^{-2} = \lambda_m^2 \geq 0$,

$$SF - R^{-2}F = 0\,,$$

for the diagonal matrix, $R^{-2} = \delta_{i,m}R_m^{-2}$, being $R = R_{di}$ of mode m.

From equations (A.9), we define S:

Now, defining $\overline{N^2_{m-0.5}} = \frac{-g'_{m-0.5}}{H_M}$, where N^2(z) is the Brunt-Väisälä frequency squared:

$$S_{11} = -\frac{1}{H_1^2}\Big(\frac{f_0^2}{N^2_{1.5}}\Big),$$

$$S_{12} = \frac{1}{H_1^2}\Big(\frac{f_0^2}{N^2_{1.5}}\Big),$$

- $S_{1m} = 0$ if $m > 2$,

$$S_{21} = \frac{1}{H_2^2}\Big(\frac{f_0^2}{N^2_{1.5}}\Big),$$

$$S_{22} = -\frac{1}{H_2^2}\Big(\frac{f_0^2}{N^2_{1.5}} + \frac{f_0^2}{N^2_{2.5}}\Big),$$

$$S_{23} = \frac{1}{H_2^2}\Big(\frac{f_0^2}{N^2_{2.5}}\Big),$$

- $S_{2m} = 0$ if $m > 3$,

$$S_{MM} = \frac{1}{H_M^2}\Big(\frac{f_0^2}{N^2_{M-0.5}}\Big),$$

$$S_{MM-1} = -\frac{1}{H_M^2}\Big(\frac{f_0^2}{N^2_{M-0.5}}\Big),$$

- $S_{Mm} = 0$ if $m < M-1$.

If the data is equally vertically spaced, $H_1 = H_2 = H_3 = ... = H_M = \Delta z$.

Thus, matrix S is:

$$S = \frac{f_0^2}{(\Delta z)^2} \begin{bmatrix} -\frac{1}{N_{1.5}^2} & \frac{1}{N_{1.5}^2} & 0 & \dots & 0 \\ \frac{1}{N_{1.5}^2} & -\left(\frac{1}{N_{1.5}^2}+\frac{1}{N_{2.5}^2}\right) & \frac{1}{N_{2.5}^2} & \dots & 0 \\ 0 & \frac{1}{N_{2.5}^2} & -\left(\frac{1}{N_{2.5}^2}+\frac{1}{N_{3.5}^2}\right) & \dots & 0 \\ \vdots & \vdots & \vdots & \ddots & \vdots \\ 0 & 0 & 0 & \dots & \frac{1}{N_M^2} \\ 0 & 0 & 0 & \dots & -\frac{1}{N_M^2} \end{bmatrix},$$

where $N_{1.5}^2 = \frac{1}{2}\left(N_1^2 + N_2^2\right)$.

We obtained the vertical structure F for a depth dependent, realistic N^2 profile. We tested the numerical solution for constant stratification, following (PEDLOSKY, 1987; LACASCE, 2012). The analytical solution of F_i is

$$F_i = A\cos\left(\frac{i\pi z}{H}\right), \tag{A.10}$$

where i is an integer and represents each normal mode, i.e. 0 for the barotropic, 1 for the baroclinic and so on. The amplitude A is equal in magnitude to that at the bottom.

Results can be seen in Figure A.1. It is clear that the results are almost indistinguishable. Yellow-colored lines represent the barotropic mode (n = 0 in equation A.10) whereas the red ones account for the first baroclinic and the blue ones for the second baroclinic modes (n = 1 and 2, respectively). One can notice the symmetry around the zero crossing in the first baroclinic mode. In a real ocean, what breaks this symmetry is the presence of the thermocline. Therefore, the numerical solution of QG modes approximates very well the analytical solution when a constant N^2 profile is used.

A.2 Surface modes — SQG theory

Differently from the traditional QG modal decomposition, the SQG equations do not form an eigenvalue problem, although the technique of separation of variables is employed here too. For details on the method, see LaCasce (2012) and Wang *et al.* (2013). Assuming a wave-like solution for Equation A.2:

$$\psi(x,y,z,t) = \chi(z)\hat{\Psi}_{k_x,k_y,\omega}e^{i(k_x x + k_y y - \omega t)}. \tag{A.11}$$

where the caret denotes the Fourier domain. The χ is a transfer function, and $\chi \in \mathbb{R}e$. Equation A.11 makes it clear that χ(z) controls the amplitude of a family of harmonic

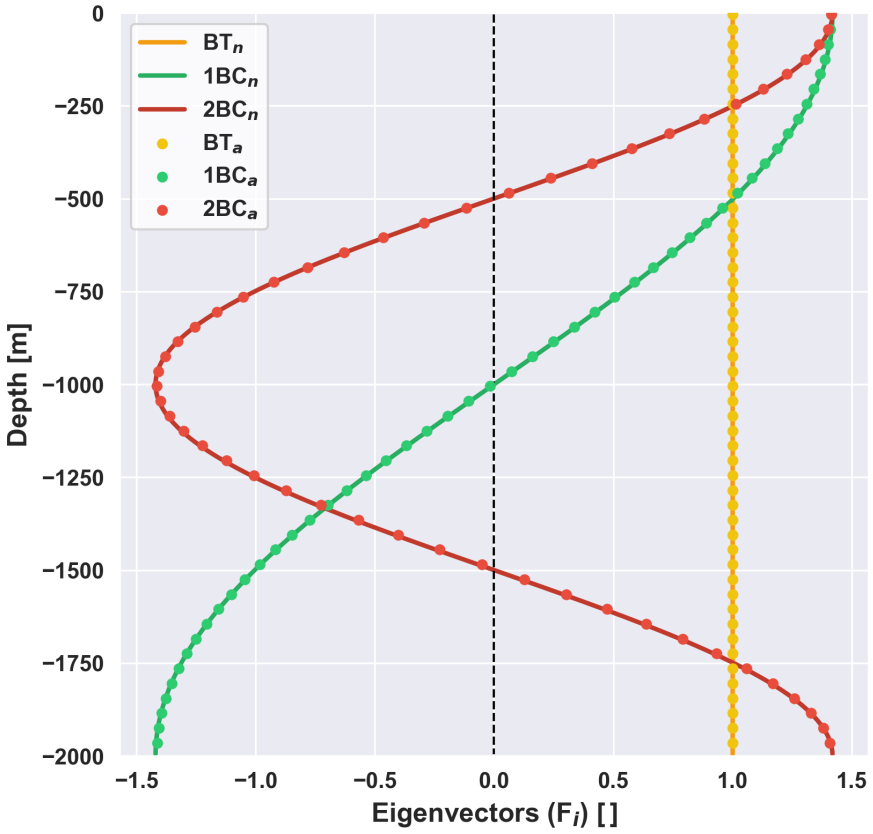

Figure A.1: Results of the modal vertical structure (F_i), also known as eigenvectors, for $i = 0, 1$ and 2 using a constant N^2, numerical (solid lines, BT_n, $1BC_n$, $2BC_n$) and analytical (scatter plots, BT_a, $1BC_a$ and $2BC_a$) solutions, the latter as in Pedlosky (1965), LaCasce (2012).

funcions that are kept either in phase or in opposition of phase.

Since the boundary condition at the surface for SQG solutions are directly related to surface density (Equation 2.2), the boundary conditions for the transfer function χ at $z = 0, -H$ are:

$$\frac{\partial \chi}{\partial z} = 1, \; at \; z = 0 \tag{A.12}$$

and

$$\frac{\partial \chi}{\partial z} = 0, \; at \; z = -H \tag{A.13}$$

Applying A.11 in A.2, and defining $\hat{\Psi} e^{i(k_x x + k_y y - \omega t)} = \phi$ to improve readability, we obtain:

$$\frac{\partial}{\partial t}\left(\frac{\partial^2 \chi\phi}{\partial x^2} + \frac{\partial^2 \chi\phi}{\partial y^2} + \frac{\partial}{\partial z}\left(\frac{f_0^2}{N^2}\frac{\partial \chi\phi}{\partial z}\right)\right) + \beta \frac{\partial \chi\phi}{\partial x} = 0.$$

Since ϕ is constant in z, we have:

$$(k_x^2 + k_y^2)\chi - \frac{\partial}{\partial z}\left(\frac{f_0^2}{N^2}\frac{\partial \chi}{\partial z}\right) + \frac{\beta k_x}{\omega} = 0.$$

Recalling that $k = \sqrt{k_x^2 + k_y^2}$,

$$\frac{\partial}{\partial z}\left(\frac{f_0^2}{N^2}\frac{\partial \chi}{\partial z}\right) - k^2 \chi = 0. \tag{A.14}$$

Analogous to the discretization QG vertical mode decomposition (Appendix A.1) and the layered potential vorticity equations, in matrix notation, Equation A.14 can be written as:

$$(S' - Ik^2)\chi = b, 1 < m < M,$$

under a M-layer approximation, where and $b = \{1, 0, ..., 0\}^T$ and S' is the same linear parameter as in Section A.1 with different boundary conditions. That is,

$$S' = \frac{f_0^2}{(\Delta z)^2}\begin{bmatrix} \Delta z & -\Delta z & 0 & \dots & 0 \\ \frac{1}{N_{1.5}^2} & -\left(\frac{1}{N_{1.5}^2} + \frac{1}{N_{2.5}^2}\right) & \frac{1}{N_{2.5}^2} & \dots & 0 \\ 0 & \frac{1}{N_{2.5}^2} & -\left(\frac{1}{N_{2.5}^2} + \frac{1}{N_{3.5}^2}\right) & \dots & 0 \\ \vdots & \vdots & \vdots & \ddots & \vdots \\ 0 & 0 & 0 & \dots & \frac{1}{N_M^2} \\ 0 & 0 & 0 & \dots & -\frac{1}{N_M^2} \end{bmatrix}.$$

To evaluate if the numerical solution is giving the correct transfer function, we tested

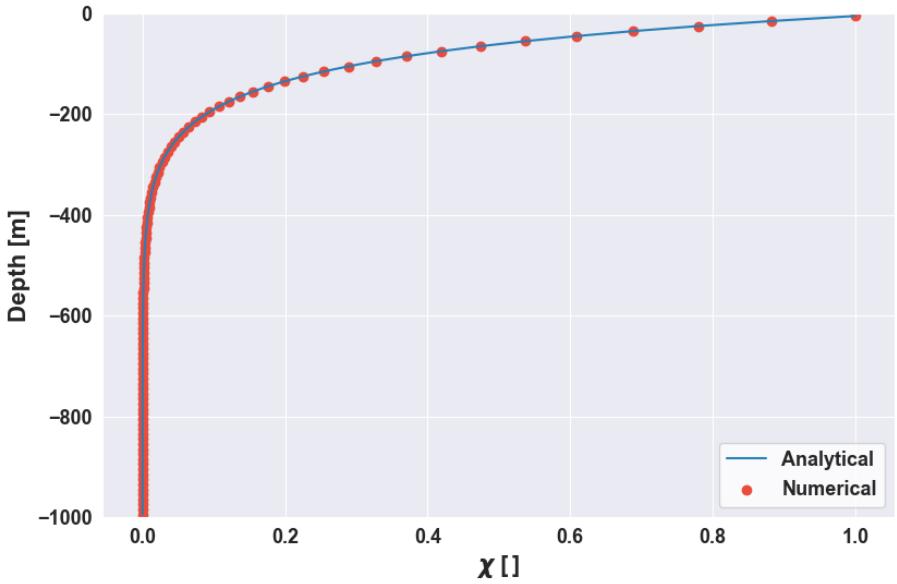

Figure A.2: Numerical and analytical solutions of the (normalized) transfer function χ for constant N^2 for an arbitrary k.

for constant stratification following LaCasce (2012). The ψ_{sqg} was reconstructed using the transfer function obtained by the numerical solution and the known analytical transfer function for constant N^2 given by:

$$\chi_a = \frac{Hk_d}{k} \frac{cosh[(1+z/H)k/k_d]}{sinh[k/k_d]}, \tag{A.15}$$

where $k_d = f_0/NH$.

Here we present three results. The comparison of the analytical χ_a and numerical χ_n (Figure A.2), the root mean square error (RMSE) between both solutions (Figure A.3) at depth and the ψ_{sqg} reconstruction (Figure A.4). At the surface, RMSE is nearly zero, which means the numerical solution is in great agreement with the analytical solution. With increasing depth, the reconstruction is not as good as at the surface, but differences are still very small, e.g. 6% at 1000 m. ψ_{sqg} is very similar between reconstructions (Figure A.4-a, b), and the differences (Figure A.4-c) are of $O(10^{-3}$ m). The results suggest the numerical solution is correct and can be used to a depth-variant N^2 profile (WANG *et al.*, 2013).

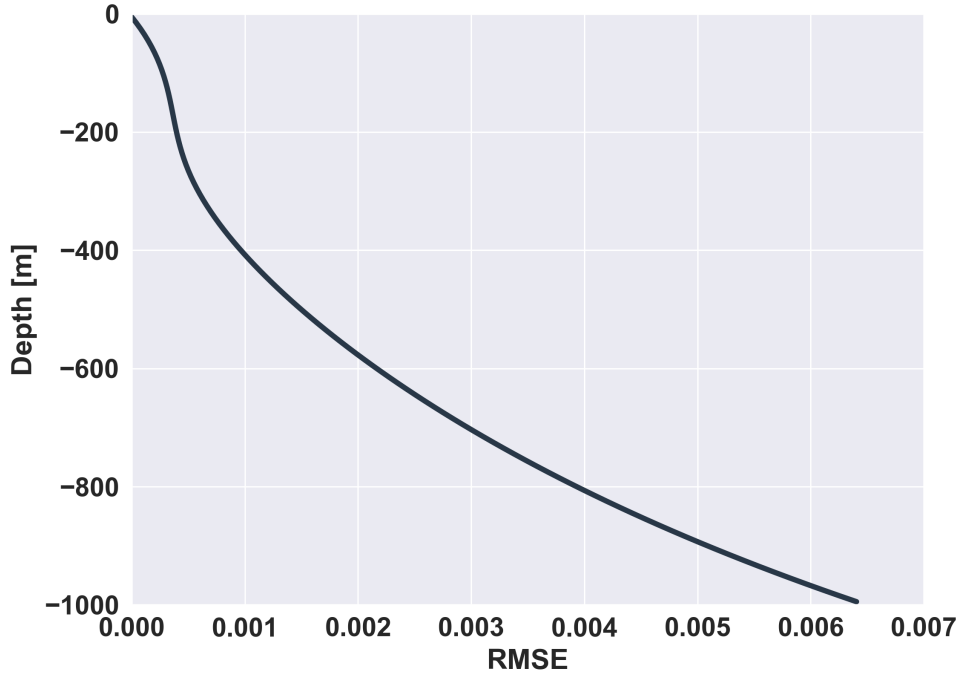

Figure A.3: Root mean square error (RMSE) between the numerical and analytical solution for constant N^2.

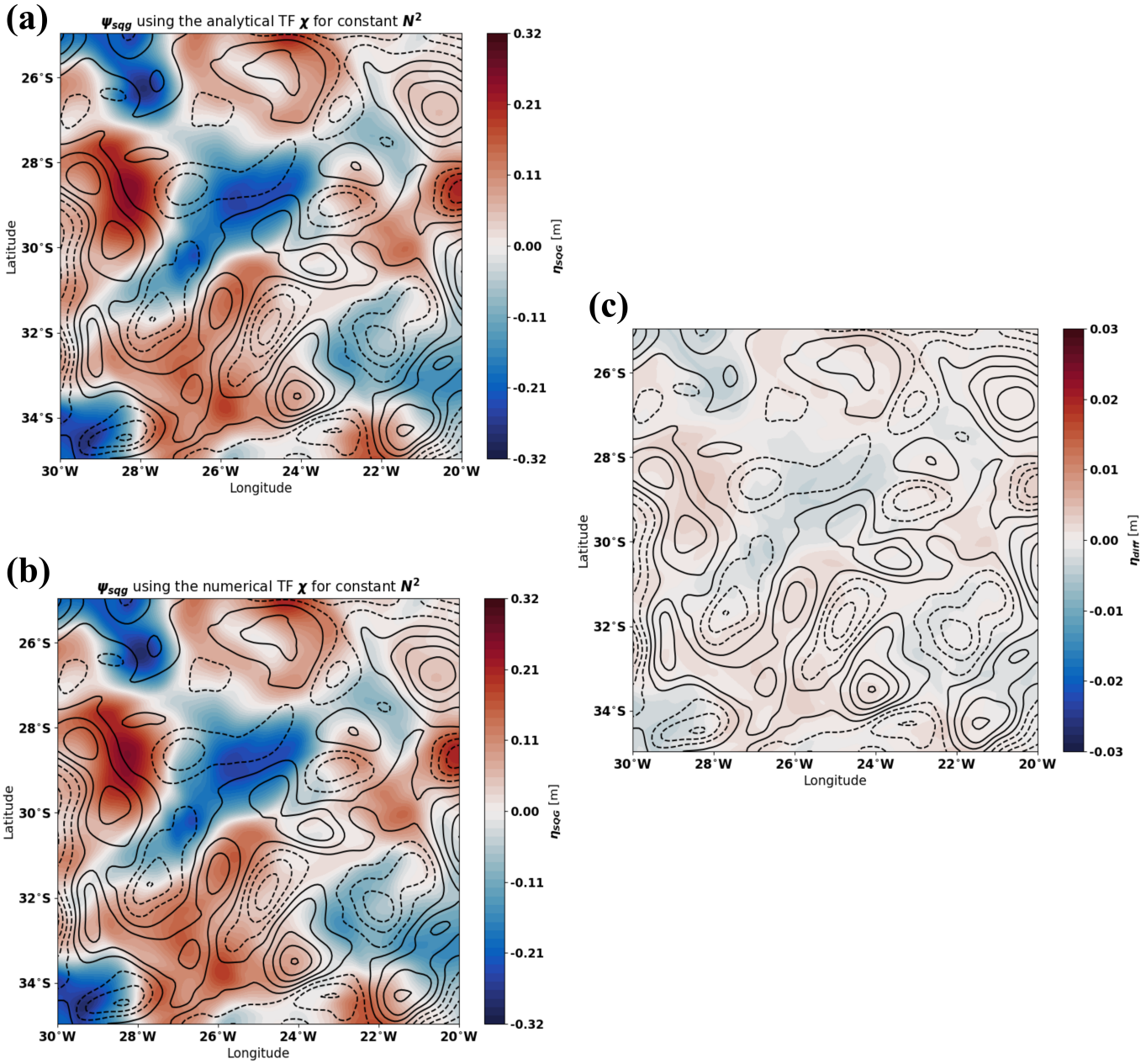

Figure A.4: Reconstructed ψ_{sqg} at the surface for a constant N^2 using (a) the analytical transfer function χ_a as in LaCasce (2012) and b_s in the Atlantic at 25-35°S, 20-30°W, (b) the numerically resolved transfer function χ_n, and the (c) difference between the two solutions. Note that limits are 10 times smaller for panel (c). Superimposed black contours represent the sea surface height from HYCOM, above (solid line) or below (dashed line) the mean sea level.

APPENDIX B – Can HYCOM-NCODA detect Rossby waves? A test case on the Pacific, 15°N

First, we have addressed whether HYCOM can represent well the sea surface field from the altimeter. Results in Section 2.1 suggest that yes, there is a good correspondence between both fields and the correlation was, on average, 0.8. Applying the same method of filtering (See Section 3.1.2) to both fields, we intended to see if HYCOM is capable of reproduce the Rossby waves seen in the altimeter. To assess this question, we chose the latitude of 15°N on the Pacific Ocean because (i) this basin is the largest of all main basins and has the strongest Rossby wave signals (POLITO; LIU, 2003), (ii) the Coriolis effect is significant and R_{di} of the first baroclinic mode is consistent to altimeter's resolution and (iii) sea surface height is influenced by the El Niño/La Niña signal. Both sea level anomaly fields were band-passed filtered and the results are as follows:

Table B.1: Results from the FIR2D at 15°N on the Pacific Ocean

Parameters	c_p **guess**	T	λ	A	c_p	**EV**
Altimeter	-11.45	24	16206	45	-18.15	24
		12	6952	37	-18.01	16
		6	2161	37	-11.93	25
		3	997	35	-11.6	27
		1	521	28	-11.26	25
HYCOM	-11.58	24	11146	52	-12.44	22
		12	5536	37	-15.76	14
		6	2126	42	-12.29	21
		3	962	39	-10.83	24
		1	498	31	-10.2	21

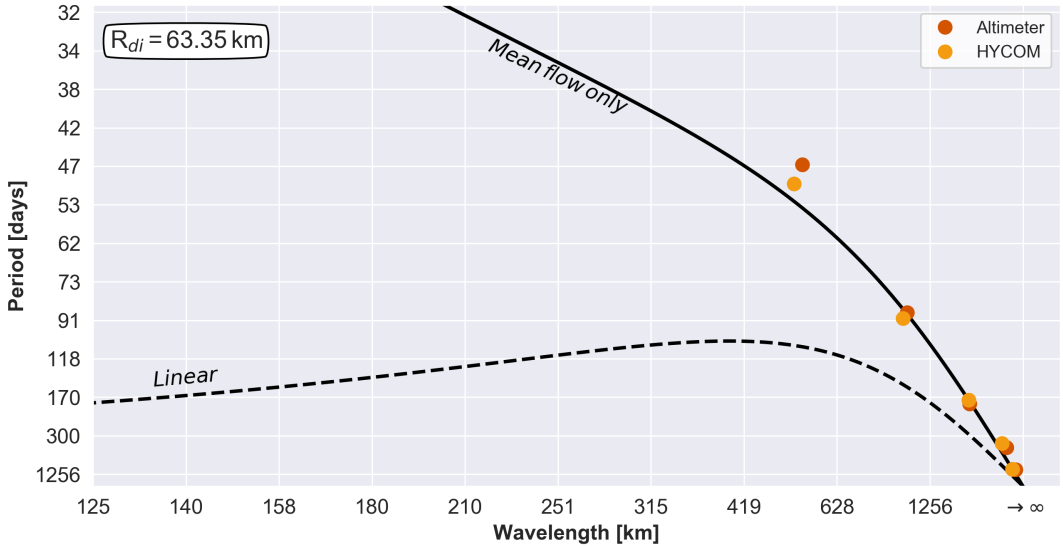

Figure B.1: Dispersion diagram for filtered first baroclinic Rossby waves from Altimeter (brown) and HYCOM (yellow). Linear theory (dashed line) and extended theory accounting for the averaged mean flow only (solid line), both with R_{di} = 63 km.

According to Polito and Liu (2003), on the Pacific between 5°N and 25°N, the biannual Rossby wave (η_{24}) has a significant amplitude and accounts for around 20% of the total variance. In our analysis, η_{24} corroborates that for both the explained variance (EV) and specially the amplitudes A (Table B.1). The filter can capture similar waves, independent of the source of the sea level anomaly fields. There are some discrepancies between the parameters from the HYCOM and the altimeter, but all values are within the error bounds of each other (not shown).

At 15°N on the Pacific, the first baroclinic Rossby radius is around 70 km (CHELTON; SCHLAX, 1996). Our R_{di} calculated from N^2 profiles using T and S from HYCOM is 63 km. We plotted the filtered waves on the dispersion diagram (Figure B.1) to assess whether they behave as first baroclinic mode Rossby waves. When accounting for the background mean flow (See Killworth and Blundell (2003) and Maharaj *et al.* (2007)), the waves – especially the low frequency ones – follow the Doppler shifted dispersion curve. The results suggest that HYCOM correctly resolves the long, first-mode baroclinic Rossby waves. The next step is to assess whether its velocities can be used to reconstruct the sea level anomaly field and if this reconstruction is representative of the altimeter data.

For the same period (2015), we calculated the modal amplitudes and the baroclinic modes using the methodology described in Section 2.2 and in Appendix A.1, the daily zonal and meridional velocities (u and v) provided by HYCOM, and T and S daily profiles

from ISAS. At different depths:

$$\mathbb{V}_i(x,y,t) = \frac{1}{H}\int_{-H}^{0} v(x,y,z,t)F_i(z)dz. \tag{B.1}$$

According to Flierl (1978) and Silveira and Brown (2000), one can reconstruct the velocities by doing:

$$v_i(x,y,z,t) = \mathbb{V}_i(x,y,t)F_i(z), \tag{B.2}$$

with an analogous expression for u_i.

As $i = [0,1,2]$, we have separately the contribution of barotropic (v_0) and first and second baroclinic (v_1 and v_2) modes. According to the root mean square (RMS) result, the explained variance of the three-mode truncation is more than 75% of the vertical structure. In other words, these modes represent the main contribution to the vertical structure, as well as the surface velocity field. The explained variance difference of including the third baroclinic mode is 2%, therefore the first three modes alone are sufficient to evaluate the dynamics, and since the detected Rossby waves are first baroclinic (Figure B.1), we decided to keep the barotropic and two baroclinic modes only.

We reconstructed the η field for 2015 (Figure B.2-e) and compared with the products from the altimeter (Figure B.2-a, b and c). The year of 2015 has nothing particular and we could have chosen any other period. We estimated the Pearson's correlation between the η from the altimeter (Figure B.2-a) and our reconstructed η based on HYCOM's velocities and the ISAS climatology (Figure B.2-e), to assess how much of the total η field (Figure B.2-a) is lost in the reconstruction calculations, and results showed that the correlation (for a single year) is around 0.5. We decided to calculate another η field, using the absolute dynamic topography and removing its annual mean (Figure B.2-b). The correlation between the latter and our reconstructed η (Figure B.2-e) was improved, reaching 0.7. Both the absolute dynamic topography and HYCOM velocity profiles have in their signal the mean currents, which explains the increase in correlations. Lastly, we calculated η from the geostrophic velocities available from the altimeter (Figure B.2-c) in the same way we calculated the reconstructed η from the vertical modes. We aimed to be consistent on the η fields to be compared. For this case, the correlation between the reconstructed η (Figure B.2-e) and the altimeter (Figure B.2-c) was 0.85. As for η derived from HYCOM velocities (Figure B.2-d), correlation was higher than 0.95, indicating that three modes are sufficient to represent the surface height field and HYCOM outputs agrees with the altimeter.

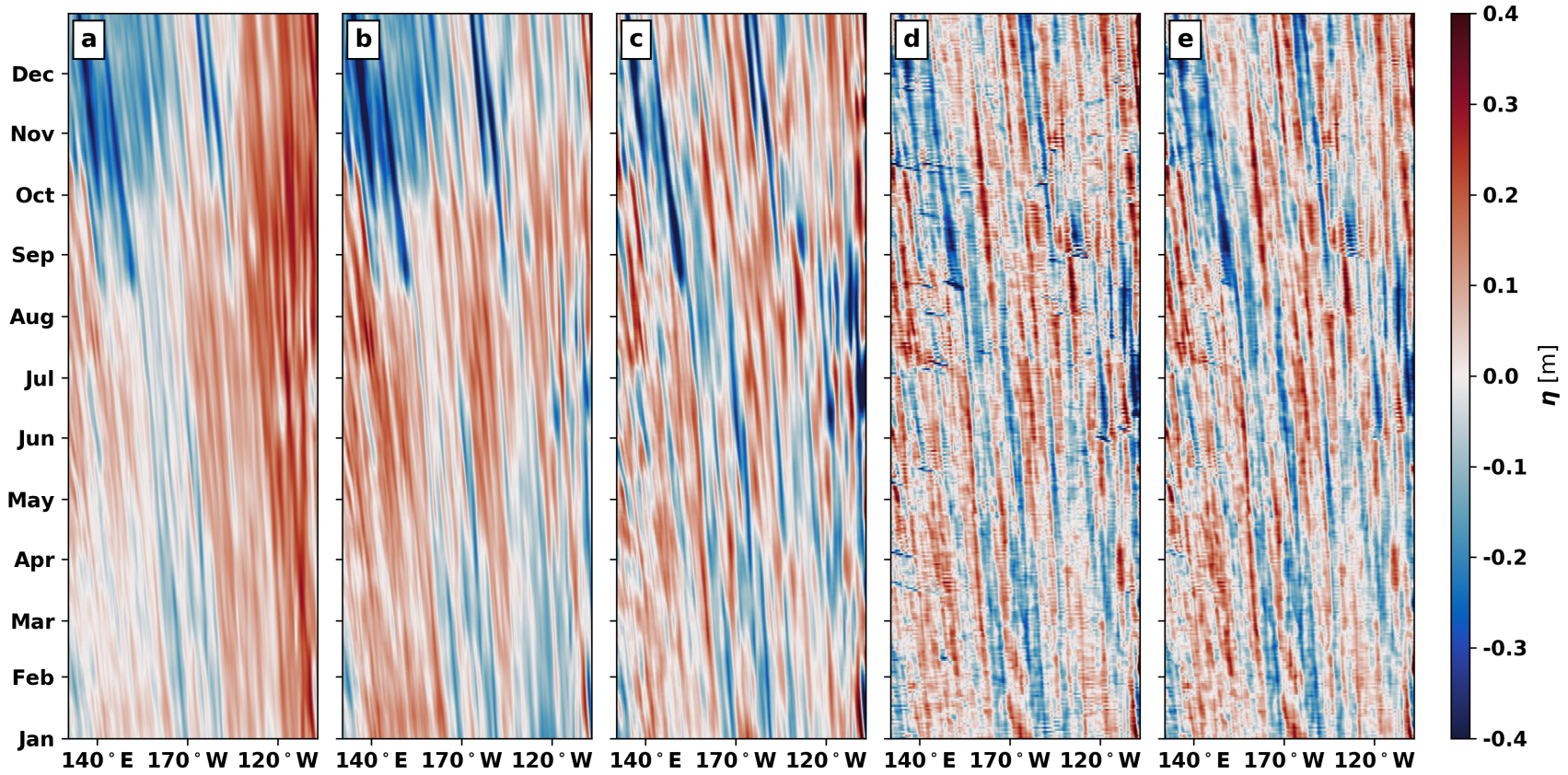

Figure B.2: Hovmöller diagrams for the Pacific ocean at 15°N: (a) Sea level anomaly from the entire altimeter series (1993–2018), (b) sea level anomaly calculated for 2015 only and (c) sea level anomaly calculated from the total velocities provided by the altimeter for 2015 only, (d) sea level anomaly calculated from the total velocities provided by HYCOM and (e) sea level anomaly reconstruction using the three mode truncation.

Back to the initial question, the answer is *yes*: HYCOM outputs can reproduce the Rossby waves observed by the altimeter and can represent the sea level anomaly field. Given the 85% correlation, we proceed in using HYCOM outputs to draw conclusions regarding the Rossby waves seen by the altimeter.